

University of Nevada, Reno

**Design and Characterization of Sectored (Patterned) IPMC Actuators
for Propulsion and Maneuvering in Bio-Inspired Underwater Systems**

A thesis submitted in partial fulfillment of the
requirements for the degree of Master of Science in
Mechanical Engineering

by

Joel Jackson Ures Hubbard

Dr. Kam K. Leang/Thesis Advisor

August 2011



THE GRADUATE SCHOOL

We recommend that the thesis
prepared under our supervision by

JOEL JACKSON URES HUBBARD

entitled

**Design and Characterization of a Sectored (Patterned) IPMC Actuators
for Propulsion and Maneuvering in Bio-Inspired Underwater Systems**

be accepted in partial fulfillment of the
requirements for the degree of

MASTER OF SCIENCE

Kam K. Leang, Ph.D., Advisor

Kwang J. Kim, Ph.D., Committee Member

Yantao Shen, Ph.D., Graduate School Representative

Marsha H. Read, Ph.D., Associate Dean, Graduate School

August 2011

Abstract

The goal of this thesis is to characterize the performance of ionic polymer-metal composite (IPMCs) propulsors for underwater applications, namely for propelling and maneuvering small bio-inspired autonomous systems. Specifically, this work examines the capabilities of IPMCs with sectored (patterned) electrodes. The electrode pattern on the surface of the ion exchange membrane is created, for example, using a straightforward surface-machining process. These IPMCs have recently been fabricated for realizing bending and twisting motion, where the main application is for creating next-generation artificial fish-like propulsors that can mimic the undulatory, flapping, and complex motions of real fish fins. Not only can the sectored IPMCs be used for actuation, but sections of the composite material can be employed as a sensor, for sensing fin deformation and responses to external stimulation. The result is a compact monolithic control surface with integrated sensing for multifunctional applications. Herein, a thorough experimental study is performed on IPMCs with sectored electrodes to characterize their performance. In particular, results are presented to show (1) the achievable twisting response; (2) blocking force and torque; (3) propulsion characteristics; (4) power consumption and effectiveness. These results can be utilized to guide the design of practical marine systems driven by IPMC propulsors. For example, a bio-inspired robotic system capable of ostraciiform locomotion with the potential to control pitch, roll, and yaw through complex twisting of the pectoral and tail fins is developed. The maximum speed for the initial prototype is measured at 2.8 cm/s. It is noted that significant improvements in swimming speed can be made, for example, by optimizing the IPMC-caudal fin geometry.

Acknowledgments

First, I would like to thank Kam, my adviser. Without his support, expertise, guidance, and most of all, patience, this research wouldn't have been possible.

I thank Dr. Kim and Dr. Shen for their support by serving on my thesis committee. Dr. Kim helped me considerably with his extensive knowledge on IPMCs and expertise in the field. I also thank the support of his research team and laboratory capabilities, particularly Viljar Palmre and David Pugal for fabricating the IPMC actuators. I would like to also acknowledge support from the Office of Naval Research, grant number N000140910218.

Next, I would like to thank my fellow graduate students of the easyLab (Max Fleming, Brian Kenton, Robert Riddle, and Yingfeng Shan). Their selfless sharing of experience and thoughtful discussions help to solve numerous issues, while at the same time their humor and companionship made coming to work enjoyable.

Lastly, my family. Their love, optimism and support has made me who I am today. Their consummate belief in me makes me believe in myself. It is what drives me to succeed and at the core of everything I have accomplished. Thank you for all that you have done, and all that I know you will continue to do as I take that next step in life.

Dedication

To my mother, Diana, and sister, Averi.

Contents

1	Introduction	1
1.1	Goal, Objectives, and Contribution	1
1.2	Motivation	2
1.3	Organization	4
2	Background	6
2.1	Underwater Locomotion in Aquatic Animals	6
2.2	Man-Made Underwater Vehicles	11
2.3	Bio-Inspired Robotic Systems	17
2.4	Ionic Polymer Metal Composites for Underwater Propulsion	20
2.5	Summary	24
3	Experimental System	25
3.1	IPMC Fabrication Process	25
3.1.1	Surface Machining Technique: Sectoring	27
3.2	IPMC Enhancement - Gold Plating Process	29
3.3	Electrical Contact Considerations	30
3.4	Control Hardware	33
3.5	Displacement Sensor Calibration	33
3.6	Drag Tank	35

3.7	Summary	37
4	Characterization	38
4.1	Twisting Response	38
4.2	Blocking Force and Torque	40
4.3	Propulsion Characteristics	45
4.4	Power Consumption and Effectiveness	53
4.5	Summary	58
5	IPMC-Based Bio-inspired Robot	60
5.1	Design	60
5.1.1	Initial Body Design: Monolithic Silicone Body	60
5.1.2	Final Body Design	61
5.1.3	Body Dynamics	65
5.1.4	Flapping IPMC	68
5.2	Performance Characterization and Analysis	71
6	Conclusions	76
7	Future Work	78
A	Alternative IPMC Assembly for Complex Bending and Twisting	87

List of Figures

2.1	Example of (a) vortex ring beginning to form from shear layer of expelled jet and (b) fully formed vortex ring [1].	7
2.2	Diagram of grass carp fish with fins used to control maneuvering and propulsion (Vlado, freedigitalphotos.net).	8
2.3	The modes of swimming locomotion employed by fish, where the shaded area indicates the regions contributing to thrust generation with darker regions representing larger amplitude motion (illustration from [2,3]).	9
2.4	Examples of short range highly maneuverable and long range high speed vehicles and their characteristic qualities: (a) the autonomous underwater vehicles (AUV) Sentry, (b) the remotely operated vehicle (ROV) Jason, used for ship wreck investigation and (c) US Navy Ohio-class ballistic missile submarine used to roam the worlds seas for nuclear deterrence (Photo (a) by Tom Bolmer, Woods Hole Oceanographic Institution; photo (b) by Chris German, Woods Hole Oceanographic Institution); and (c) www.3dcadbrowser.com).	13
2.5	Limit cycle exhibited by the ROV Jason, in calm water while attempting to station-keep relative to a desired position with a control scheme that does not account for thruster dynamics [4]. The ROV itself is shown in Fig. 2.4(b).	15

2.6	Biological life that utilized vortex ring thrusters for propulsion and maneuvering include (a) squid and (b) jellyfish [1].	16
2.7	Examples of biomimetic robots, the body and caudal fin (BCF) locomotion modes they mimic, and the groups that developed them [5].	18
2.8	(a) Scanning electron microscope image of the cross-section of a Nafion-based IPMC. (b) Illustrative movement of cations and water molecules inside of an IPMC.	22
2.9	IPMC AM fin motion: (a) bending and (b) twisting.	23
3.1	The above figure depicts the fabrication process that starts with a piece of commercial Nafion membrane and ends with a fully functional IPMC.	26
3.2	(a) Example patterned IPMC (units in millimeters) and (b) experimental setup for measuring bending/twisting response.	28
3.3	Electrode patterning process: (a) the masking and (b) the surface-machining technique.	29
3.4	Displacement and force responses before and after Au plating.	30
3.5	IPMC bending before (left) and after (right) gold plating.	31
3.6	Electrodeposition process for Au plating magnets and IPMCs.	32
3.7	Custom-design voltage/current amplifier for IPMC actuator: (a) circuit diagram, (b) fabricated circuit board, and (c) measured cross-over distortion vs. frequency.	34
3.8	The experimental setup for (a) laser sensor calibration and (b) the resulting data.	35
3.9	Left, the prototype similar to how it was tested for drag coefficient and Right, the drag tank and carriage system.	36

4.1	The achievable twist angle of a 4 sector IPMC was obtained using the (a) the experimental setup and (b) the definition of the twist angle where d_1 and d_2 are obtained by the laser sensors.	39
4.2	Twist angle of IPMC versus amplitude of DC input voltage.	40
4.3	Twist angle verses input signal frequency (sinusoidal input).	40
4.4	Experimental setup for measuring the blocking force and torque of a sectored IPMC	42
4.5	Bending force of sectored IPMC versus input signal frequency.	44
4.6	Blocking torque of IPMC versus input signal frequency.	44
4.7	Diagram of an oscillating rigid tail fin.	46
4.8	Experimental setup used to measure the thrust of IPMC and caudal fin tail assembly.	47
4.9	Frequency response of conventional IPMC with attached passive caudal fin.	47
4.10	Thrust response of conventional IPMC with caudal fin when driven by a 3-V, 1.1-Hz sine wave at resonance.	48
4.11	Average thrust of conventional IPMC-Caudal fin assembly when actuated by a sinusoidal input.	49
4.12	Thrust production of assembly in Fig. 4.13a when actuated by different input waveforms at 2 V.	50
4.13	IPMC-caudal fin assemblies used for thrust testing (units in mm): (a) conventional IPMC sample and simple trapezoidal caudal fin, (b) sectored IPMC with simple caudal fin, and (c) with bio-inspired caudal fin.	51

4.14	Thrust production of sectored IPMC in conjunction with caudal fin shapes shown in Fig. 4.13(b) and Fig. 4.13(c) when actuated by sinusoidal input voltages.	52
4.15	Power Consumption of assembly in Fig. 4.13(a) when actuated sinusoidal input voltage.	54
4.16	Power Consumption of assembly in Fig. 4.13(a) when actuation by different input waveforms of 2 V amplitude.	55
4.17	The ratio of average thrust force to power consumed, Υ , for the IPMC and tail fin geometry seen in Fig. 4.13(a) when actuated sinusoidal input voltage.	56
4.18	The ratio of average thrust force to power consumed, Υ , for the IPMC and tail fin geometry seen in Fig. 4.13(a) when actuated by different input waveforms of 2-V amplitude.	57
4.19	Power consumption of sectored IPMC and caudal fins seen in Fig. 4.13(b) and (c) when actuated sinusoidal input voltage.	58
4.20	The ratio of average thrust force to power consumed, Υ , for sectored IPMC shown in Fig. 4.13(b) and (c) verses frequency of sinusoidal input voltage.	59
5.1	Initial design: monolithic body (a) the 3-D model, (b) used to construct the body out of silicone casting rubber and (c) the bottom view and (d) top view of the resulting cast body.	62
5.2	Two bio-inspired IPMC-based robots: (a) prototype with gold-plated IPMCs where pectoral fins consisted of individual actuators connected by Kapton [®] film and (b) prototype with three bi-sectored IPMCs.	63
5.3	Robot motions and required fin orientations.	64

5.4	The 2-D representation of the body dynamics of the prototype during ostraciiform locomotion.	66
5.5	Free body diagram of forces acting on oscillating tail, where D and L represent drag and lift forces, respectively.	69
5.6	Simplistic model proposed to predict the prototype's velocity.	72
5.7	Experimentally and predicted velocities of prototype when actuated by 5 V sinusoidal input.	73
5.8	An illustration of the reverse Kármán vortex street generated by a swimming fish.	75
A.1	Soft medium with embedded IPMCs: (a) front view and (b) isometric view.	88
A.2	Time lapse images of boot-IPMC assembly bending due to a 4 V 50 mHz square wave input signal. The times corresponding to the images are indicated by the red dotted lines overlaid on the input signal plot directly above.	89
A.3	Two views depicting the maximum twist angle achieved. The input signal is plotted directly above and the time of maximum deflection is noted by the red dotted line.	90

List of Tables

5.1	Added mass coefficients of a 2-D thin plate as defined in [6].	70
-----	--	----

Chapter 1

Introduction

This chapter focuses on the research goal, objectives, contribution, and motivation. The organization of this thesis is at the end of the chapter.

1.1 Goal, Objectives, and Contribution

The goal of this thesis is to characterize the performance of ionic polymer-metal composite (IPMCs) propulsors with sectored (patterned) electrodes for underwater applications, namely for bio-inspired autonomous systems. Specifically, the objectives to achieve this goal are to:

1. Measure the achievable twisting response;
2. Characterize the blocking force and torque;
3. Examine the propulsion characteristics of IPMC-based propulsors;
4. Quantify the power consumption and effectiveness; and
5. Create a bio-inspired robotic system capable of ostraciiform locomotion with potential to control pitch, roll, and yaw through complex twisting of the pectoral and tail fins.

The main contribution of this research work is to provide performance measures which can be used to guide the design of practical marine systems driven by IPMC propulsors.

1.2 Motivation

Ionic polymer-metal composite (IPMC) material is a promising active (smart) material for engineering novel soft biomimetic actuators and sensors, particularly for underwater applications [7–14]. Notable advantages IPMCs include low driving voltage (<5 V), relatively large strain, soft and flexible structure, and the ability to operate in an aqueous environment (such as water). When an IPMC is mechanically deformed, charges develop on the electrodes and thus IPMCs can function as a sensor [10, 15]. More recently, monolithic IPMCs with the sectored (patterned) electrodes have been introduced to create bending, twisting, and complex deformation [16–18]. These patterned IPMCs can be used to develop propulsors that can mimic, for example, the flapping (pitch and heaving) motion and complex behavior of real pectoral and caudal fish fins.

This research focuses on the capabilities of IPMCs with sectored (patterned) electrodes. The electrode pattern on the surface of the ion exchange membrane is created, for example, using a straightforward surface-machining process. These IPMCs have recently been fabricated for realizing bending and twisting motion, where the main application is for creating next-generation artificial fish-like propulsors that can mimic the undulatory, flapping, and complex motions of real fish fins. Not only can the sectored IPMCs be used for actuation, but sections of the composite material can be employed as a sensor, for sensing fin deformation and responses to external stimulation. The result is a compact monolithic control surface with integrated sensing for multifunctional applications in a wide spectrum of micro-autonomous robots

and underwater systems. Herein, a thorough experimental study is performed on IPMCs with sectored electrodes to characterize their performance for propelling and maneuvering small bio-inspired robotic systems.

The proficiency of sectored IPMC actuators at reproducing smooth complex bending and twisting motion makes them ideal for use in bio-inspired robotics. However, for practical applications and to help guide the design of such systems, a thorough understanding of their characteristics and limitations is needed. This research will provide performance measures for future designs of IPMC-based systems. Additionally, through the characterization of the IPMC's performance, a prototype biomimetic robotic fish that is capable of multiple degrees of freedom is developed. The prototype and its performance characteristics can serve as a foundation for the design of future IPMC enabled underwater robotic vehicles.

IPMCs for underwater vehicles are predominately used as control surfaces and propulsors. For example, strips of IPMCs have been used to construct the legs (tentacles) of a jellyfish-like robot [19, 20]. The swimming speed of the jellyfish robot was controlled through the frequency of the input voltage applied to the IPMC-based legs. Likewise, the caudal fin to propel a robotic fish was created from an IPMC actuator with an achievable peak swimming speed reported at 22 mm/s [21]. The control surfaces can be used passively, replacing rigid structures in current designs, or employed in a more active role where IPMC movement itself generates direct maneuvering forces while maintaining the potential to be used as a passive control surface. An example of where IPMCs with these capabilities can be of benefit is in the development of highly-maneuverable biorobotic vehicles, e.g., the system described in [22]. In order to effectively design and utilize IPMC for these applications, a thorough understanding of their ability to generate twist and force is needed as this governs the range of directional forces that can be generated. In a more prominent applica-

tion, IPMCs can also be used in combination with passive media to amplify potential thrust generation and act as the primary propulsory for underwater devices.

Recently bio-inspired robotic designs featuring IPMC actuators as the primary propulsor have had limited maneuvering capability. Furthermore, successful integration these active-material actuators is hindered by limited knowledge of their capabilities. Ultimately, when IPMC actuators are used in either configuration the capabilities of the vehicle are fundamentally limited by the ability of the IPMCs themselves. Successful integration IPMCs requires knowledge of their capabilities with respect to underwater locomotion. This research focuses on characterizing conventional IPMC actuators as well as recently developed sectorized IPMCs to aid in future development of IPMC enabled systems. Specifically, results are presented to show (1) the achievable twisting response; (2) blocking force and torque; (3) propulsion characteristics; (4) power consumption and effectiveness. These results can be utilized to guide the design of practical marine systems driven by IPMC propulsors. A bio-inspired robotic system capable of ostraciiform locomotion with potential to control pitch, roll, and yaw through complex twisting of the pectoral and tail fins is developed. The maximum speed for the initial prototype is measured at 2.8 cm/s. It is noted that significant improvements in swimming speed can be made, for example, by optimizing the IPMC-caudal fin geometry.

1.3 Organization

This thesis is organized as follows. Chapter 2 presents a review of underwater locomotion for biological life forms and man-made vehicles, bio-inspired designs for propulsion and maneuvering, and ionic polymer-metal composite material. Chapter 3 presents the experimental setup, specifically the hardware and software used to characterize the IPMC actuator systems. Chapter 4 discusses characterization re-

sults. Chapter 5 discusses the two prototype bio-inspired robotic platform designs which employ the IPMCs for propulsion and maneuvering. The performance characteristics the prototypes are also presented. Concluding remarks are in Chapter 6, followed by future work in Chapter 7. Appendices are found at the end.

Chapter 2

Background

Underwater locomotion is defined as the propulsion and maneuvering techniques utilized in an underwater environment. Biological systems are capable of complex multiple degrees-of-freedom motion and man-made systems are generally very limited, for example the propulsion of a spinning propeller. Propellers are the standard method for man-made systems such as boats and submarines. On the other hand, biological systems utilize highly dexterous fins and body movements. The mechanisms behind the two platforms, marine life and man-made, are discussed below. Specifically, this chapter discusses the fundamentals of underwater locomotion, reviews current state-of-the-art man-made robotic systems, and presents the basics of active material-based actuators such as ionic polymer-metal composites. The IPMC is used in this work to mimic the propulsion characteristics of aquatic animals.

2.1 Underwater Locomotion in Aquatic Animals

Swimming locomotion techniques employed by aquatic life vary widely. However, they are all similar in that they exist in the realm of unsteady force. The locomotion methods can be broken down into two groups, those that employ vortex ring thrusters (VRTs) and those that utilize body or fin undulation for maneuvering and propulsion [2,3]. This first group consists of animals such as squid, jelly fish, and octopuses

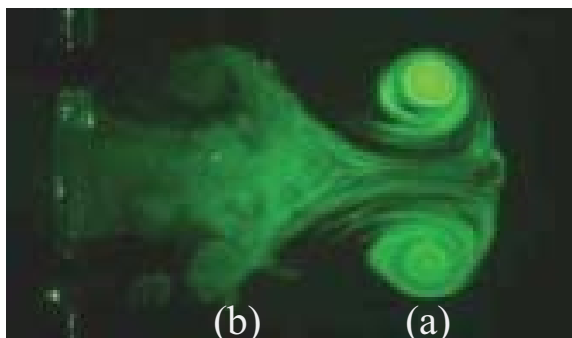


Figure 2.1: Example of (a) vortex ring beginning to form from shear layer of expelled jet and (b) fully formed vortex ring [1].

(see Fig. 2.6). These animals draw liquid into a cavity and then squeeze it (reducing the volume of the cavity quickly) to eject the fluid out of a nozzle like structure [1]. The vortex ring, also known as a toroidal vortex, is generated by the shear layer that results from the high momentum jet encounter in the ambient fluid and can be seen in Fig. 2.1. The VRT technology offers significant advantages over contemporary methods. These advantages and its potential use in underwater vehicles is discussed later in Section 2.3.

The other locomotion method employed by the large of majority of aquatic life involves flapping, pitching, or heaving of a flexible foil. This technique is seen in rays, sharks, and especially fish [2]. For the purposes of this thesis fish are used as the biological example and the source of bio-inspiration. The body and fins of fish come in all shapes and sizes, however, on some level all fish feature a streamlined body with flexible fins. Usually, seven fins (see Fig. 2.2) are effectively positioned about the body; the movement of these surfaces are primary source of maneuvering and propulsive forces [23]. Typically, a fish features a dorsal, anal, and caudal fin along with pairs of pectoral and pelvic fins. The dorsal and anal fins are used for stability in the roll plane. The number, shape, and function of these fins changes depending on the speed or habits of the fish. For instance, some fish may utilize the median

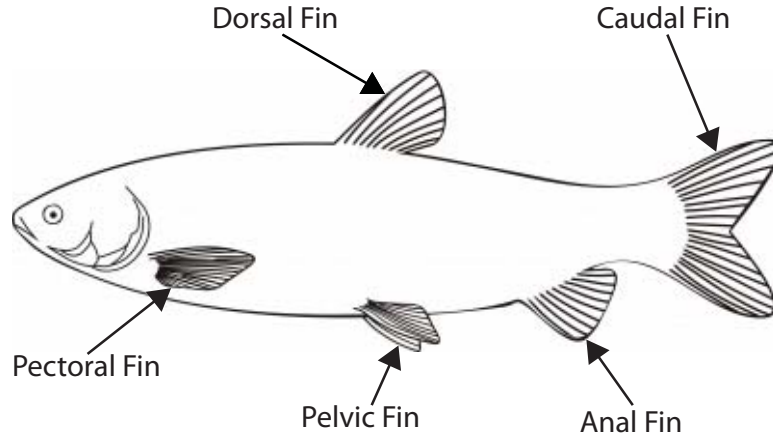


Figure 2.2: Diagram of grass carp fish with fins used to control maneuvering and propulsion (Vlado, freedigitalphotos.net).

paired fins (pectoral or pelvic fins) to maneuver or station keep at low speeds while at they may act as rudders at higher speeds with the caudal fin being the primary source of propulsion. Additionally, fish that spend their time operating at low speeds or in littoral areas may feature larger or more numerous dorsal, anal, and pelvic fins to aid in maneuvering through increased active surface area.

Movement of these fins and the body are responsible for the development of propulsive and maneuvering forces. These movements, and thus the propulsion and maneuvering techniques, differ between low speed maneuvering and high speed transit. For instance, from rest the fish can accelerate using large amplitude oscillations of the caudal fin then settle to quicker but smaller amplitude movement at cruising speed. Furthermore, fish that move at high speeds regularly swim much differently than normal fish, particularly with respect to body movement. Several very different swimming methods are seen across the broad spectrum of existing fish species. There are those that utilize body undulations in combination with caudal fins for primary propulsion, ones that employ rapid undulation or oscillation of the median paired fins, and those generate undulations over elongated dorsal or anal fins for thrust [3]. These

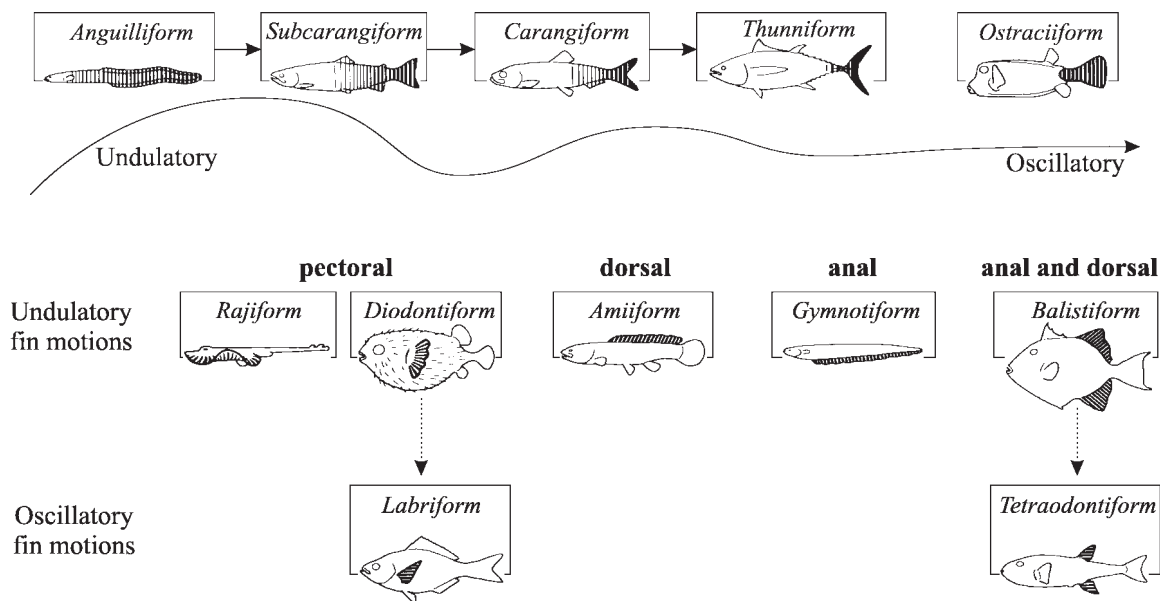


Figure 2.3: The modes of swimming locomotion employed by fish, where the shaded area indicates the regions contributing to thrust generation with darker regions representing larger amplitude motion (illustration from [2,3]).

locomotion techniques are illustrated in Fig. 2.3 where the shaded regions indicate the area of movement with darker regions indicating larger amplitude movement.

The most extreme of these groups being anguilliform, is best represented by the pure undulatory movement, like that of eels. In this mode a sinusoidal waveform is initiated at the front and propagates down the body; the amplitude of movement grows down the body toward the tail. Similarly in sub-carangiform locomotion, a propagating wave of undulation is seen however the increasing amplitude is limited and seen in the last half of the body. Carangiform swimming, on the other hand, involves further limited motion, isolated to the last third of the fish body. Fish with carangiform locomotion typically feature a stiffer caudal fin and are capable of faster swimming than fish using more undulatory modes. In other words, the swimming behavior of an eel is one of the slowest and in some sense, least efficient. Lastly, the fastest of these techniques is the thunniform locomotion. The thunniform swimming

mode is utilized by fish and sharks and are suited to high speeds in calm water; it also the most efficient of all the swimming modes and are regarded as the most advanced swimming mode in the evolutionary development of swimming. Fish utilizing this mode feature stiff crescent (sometimes referenced as lunate) shaped caudal fins that are tall by comparison to caudal fins typical seen in other modes. Lastly, ostraciiform swimmers are characterized by completely rigid bodies and stiff caudal fins. These swimmers typically utilize the median pair fins for primary propulsion; auxiliary propulsion at higher speeds can consist of pure oscillatory flapping of the caudal fin [3].

There is a prominent trend in the body and caudal fin (BCF) locomotion modes discussed. The fish that utilize the various locomotion modes seem to be dependant on certain qualities, such as body stiffness. Anguilliform swimmers have very flexible bodies that lend themselves well to the undulatory motion while thunniform and ostraciiform swimmers have rigid bodies with movement concentrated around the peduncle joint (at the base of the caudal fin).

Another important consideration that is essential to locomotion is buoyancy. The bone, flesh, and cartiligenous tissue that make up the fish's body have higher densities than the surrounding water. As a result without measures in place to counteract the negative buoyancy they would sink. Also, without an active system the range of depths an aquatic animal can explore is severely limited. Fish body types fall into two groups, osteithyes, or bony fish and typically what one would think of at the mention of a fish and a second group called Condricthyes, which are boneless fish that depend on cartiligenous tissue for structure. The latter group consists of fish like sharks and rays. Many animals store less dense oils to aid in buoyancy but this is done over time and does not allow short term changes. To fully address this problem animals have developed systems to combat this problem. Those osteithyes

fish utilize a swim bladder that is typically situated near the dorsal fin. By controlling the pressure in the bladder relative to the depth, the volume of the bladder can be controlled and thus, the effective density of the fish is controlled. The placement of the swim bladder also aids in stability of the entire fish. Cartilaginous fish, or condricthyes, feature large, oil dense livers. The difference in densities between oil and water provides some buoyancy that negates dead weight but only provides a partial solution. The difference is made up through dynamic lift. This technique is a byproduct of the forward swimming motion and airfoil shaped pectoral fins. As the fish swims forward, water flows over the top of the pectoral fins faster and the resulting low pressure generates lift. The down side to this technique is that when this forward motion stops the fish can sink.

2.2 Man-Made Underwater Vehicles

Man-made underwater vehicles are developed for a wide array of applications. These range from the long distance travel of submarines circumnavigating the globe to small submersibles investigating ship wrecks in tight quarters. The issue is that current design conventions mean that vehicles are relegated to one of two realms: high speed, efficient travel that allows for long range transport, or low speed travel with maneuverability and a limited travel range. The lack of overlap between vehicles in one of these realms can be attributed to their propulsion and maneuvering techniques.

Currently underwater vehicles, regardless of their design, depend solely on propellers and control surfaces to generate thrust and maintain control. Vehicles that are developed for long range travel adopt a high aspect ratio, streamlined body; for example, ballistic submarines in use by the navy [see Fig 2.4(c)]. This allows for minimal drag at speed and increases propulsive efficiency. For maneuvering, control surfaces along the body are used often in tandem with some form of thrust vectoring.

However, the large aspect ratio makes thrust vectoring minimally effective other than to induce a rotation of the vehicle itself. The control surfaces function as intended at high forward speeds, generating control forces necessary to maneuver the vehicle. However, the forces generated by the surfaces are highly dependant on the speed at which the vehicle is traveling, a consequence that results in insufficient control forces for maneuvering at low speeds [24]. The common solution would be to incorporate larger or more numerous control surfaces, which, while increasing maneuvering potential, is counter productive to a streamlined efficient body.

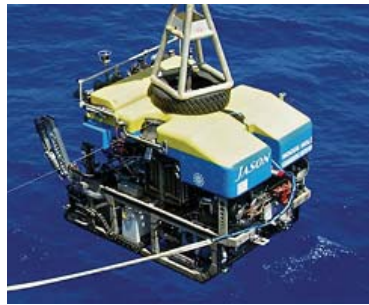
Looking at vehicles at the other end of the spectrum, i.e., low aspect ratios and limited range, issues arise from the same technology. These vehicles tend to be designed to be highly maneuverable by employing stout outer dimensions and multiple thrusters. This makes the vehicle inherently inefficient for traveling long distances or traversing any distance quickly. Examples of this kind of vehicles are remotely operated vehicles (ROVs) and autonomous underwater vehicles (AUVs) for scouting and exploring ship wreckage or the oceans bottom, some of these vehicles are shown in Fig. 2.4(a) and (b). In this case multiple propulsors can be used to maneuver. However, their ability to control the vehicle accurately is in question itself.

It is very clear that solely relying on control surfaces for maneuvering is not practical, particularly at low speeds. The question then becomes can conventional technology be used to improve maneuverability of conventional vehicles. In [4] it was determined that at low speeds the behavior of the underwater vehicles is dominated by the dynamics of the thrusters, in this case the propellers. The propellers ability to produce thrust is governed by its ability to artificially produce a steady flow in an arbitrary direction. This ability is greatly influenced by changes in the axial and cross flow of the surrounding fluid. A predominate reason for this is the changes in effective attack angle of the blade of the propeller relative to the flow as a result for

**Short Range
Highly maneuverable**

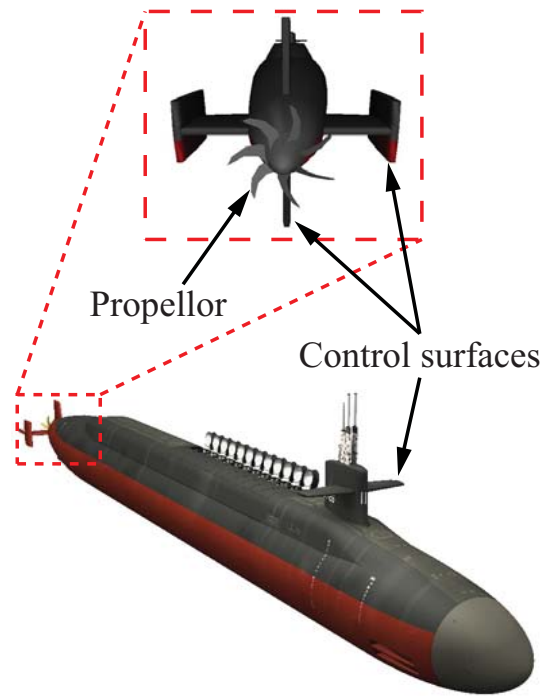


Multiple thrusters
(a)



Boxy, low aspect ratio
body
(b)

**Long Range
Fast and Efficient**



Propellor
Control surfaces
Teardrop shape low drag
body, high aspect ratio
(c)

Figure 2.4: Examples of short range highly maneuverable and long range high speed vehicles and their characteristic qualities: (a) the autonomous underwater vehicles (AUV) Sentry, (b) the remotely operated vehicle (ROV) Jason, used for ship wreck investigation and (c) US Navy Ohio-class ballistic missile submarine used to roam the worlds seas for nuclear deterrence (Photo (a) by Tom Bolmer, Woods Hole Oceanographic Institution; photo (b) by Chris German, Woods Hole Oceanographic Institution); and (c) www.3dcadbrowser.com).

these changes [4]. For maneuvering at low speeds these problems are exacerbated.

At the low speeds the cross and axial flow effects are more pronounced due to their proportion to the lower vehicle speed. It is at these low speeds, or stationary positions, that precision maneuverability is needed. Often these scenarios require a vehicle to dock to port, work in close proximity to other vehicles, or provide a stable platform for measurements from sensitive equipment. Due to the nature of the environment vehicles frequently face disturbances from waves movement and changes in currents and local flow [25]. As a result, for a thruster to be effective at these tasks it must be able to produce small forces reliably and for short durations [1, 4]. In addition, the propellers thrust generation must have a settling time that is small by comparison to the transient behavior of the surrounding environment. While at high rotational speeds propellers operate at high efficiencies and produce predictable thrust. Unfortunately, to produce low levels of thrust conventional propellers have to operate in the realm of single digit rotations. At these levels of rotational frequency propellers are found to produce wide range of magnitude and direction of forces; including forces in the opposite direction desired [26]. The reason for this is similar to what has been discussed above.

At the slow rotational speeds the behavior and response of the propeller is increasingly dependant on the velocity of the surrounding fluid. Also, the propeller has a settling time that is associated with its thrust production as well as thrust termination. At higher speeds where forward velocity of a vehicle is of concern this poses no problem, however, for precision maneuvering this is an issue and can result in overshoot. Combined with an environment that includes fluid flow that changes both direction and magnitude with respect to time, basic station-keeping becomes difficult. This is illustrated in Fig. 2.5, where the position of a underwater ROV is shown as it attempts to station-keep in a dockside test in calm water [4]. The ROV does not

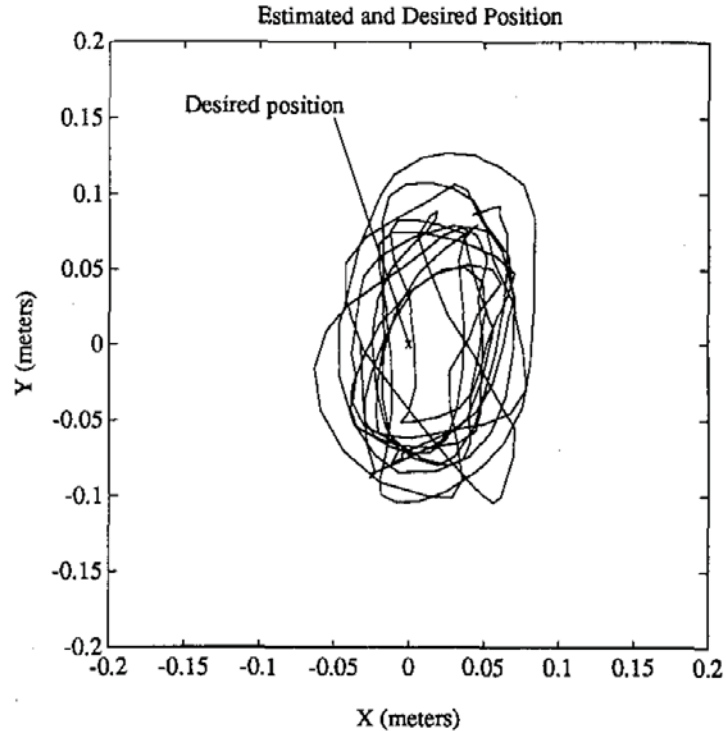


Figure 2.5: Limit cycle exhibited by the ROV Jason, in calm water while attempting to station-keep relative to a desired position with a control scheme that does not account for thruster dynamics [4]. The ROV itself is shown in Fig. 2.4(b).

feature a control scheme that accounts for the thruster dynamics. In [4] it was shown that significant improvements in position control can be realized by implementing a control scheme that reflects the dynamics of the propeller itself. Even so it was shown that at low rotation speeds non-linearities in the dynamics of the propeller effect the thrust generation in a underlying way that is much different than the typical inertial and hydrodynamic non-linearities that are already accounted for [4]. It is because of this, and the fact that vehicles feature not one, but many thrusters, that rectifying this through control techniques becomes difficult.

While the engineering community regards the majority of technology used in propulsion and maneuvering to be fully matured significant advancements can be made by taking after nature. The locomotion techniques of underwater animals have

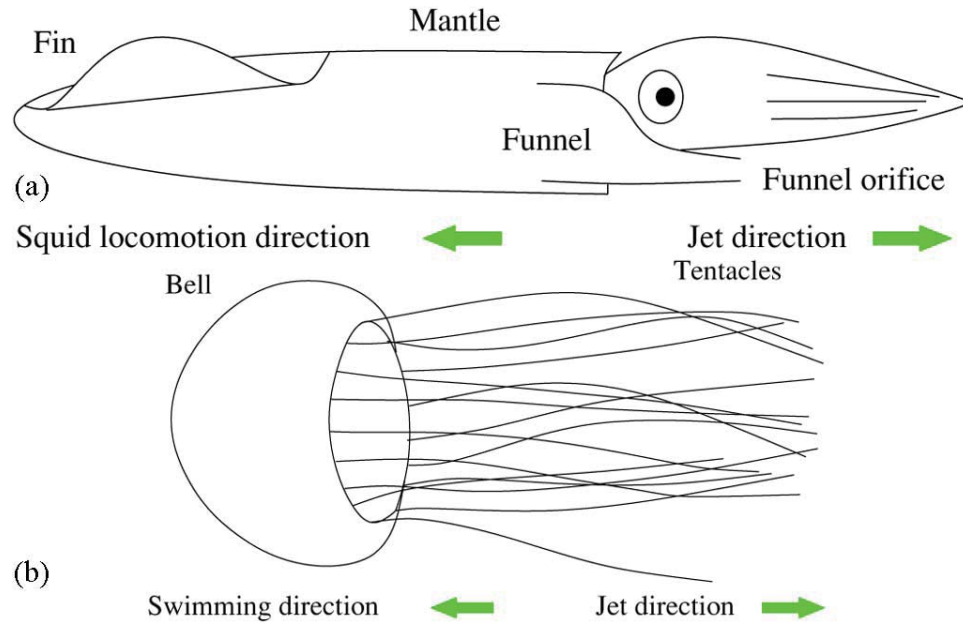


Figure 2.6: Biological life that utilized vortex ring thrusters for propulsion and maneuvering include (a) squid and (b) jellyfish [1].

largely been understood for decades [2]. But in more recent years, advances in computing power have allowed detailed analysis and a more thorough understanding of the mechanisms behind the superior performance of animals locomotion when compared to man-made techniques.

It is pointed out that the operation of most biological platforms is the unsteady vortex dominated range while current successful man-made platforms rely solely the the steady state momentum dominated realm [27]. When maneuvering techniques are examined this again holds true. Research in the past two decades has centered around understanding the movements and unsteady operating range. The reason behind this past, and continuing research, can be attributed to the swimming efficiency and particularly, the maneuverability, of biological life typically being an order of magnitude superior to that of current successful man-made technology [28].

2.3 Bio-Inspired Robotic Systems

Currently, man-made machines employ steady state techniques for generating thrust both for travel and maneuvering in a fluid environment, be it air or water. Unfortunately, technologies today limit the design of vehicles to singular applications; meaning applications that require speedy transit or long distances, or ones that necessitate high maneuverability. Furthermore, existing propulsion technologies can be very noisy, which greatly limits the application potential as it influences the ability to operate in close proximity to biological life or meet the needs of a military that puts an increasing emphasis on stealth. To provide next-generation underwater vehicles with the advantages of biological systems, fish and rays are explored for their potential use in biomimetic underwater vehicles.

Most animals operate using locomotion techniques based on unsteady lift and drag mechanisms. There have been many advances in man-made technology made by distilling concepts that have been extracted from biological life that use these principles. For instance, Boeing's Gulfstream II utilizes winglets on its wings and Bannasch developed a round tipless propeller that both reduce wing-tip drag; both new features greatly increase efficiency of a steady state realm vehicle while being conceived from examining the biology of live eagles [28]. Similar advances can be gleaned from marine life as well. Recently, many bio-mimetic or bio-inspired robots have been built that look to employ the unsteady locomotion techniques utilized by marine animals for their significant advantages over conventional propulsion techniques (as pointed out above in Section 2.2). These robotic platforms have used both conventional technologies, that include electric motors and servos, linear actuators, and compliant mechanisms, as well as several classes of active materials (discussed next). An overview of past and continuing efforts to create bio-inspired robots is discussed in the following.

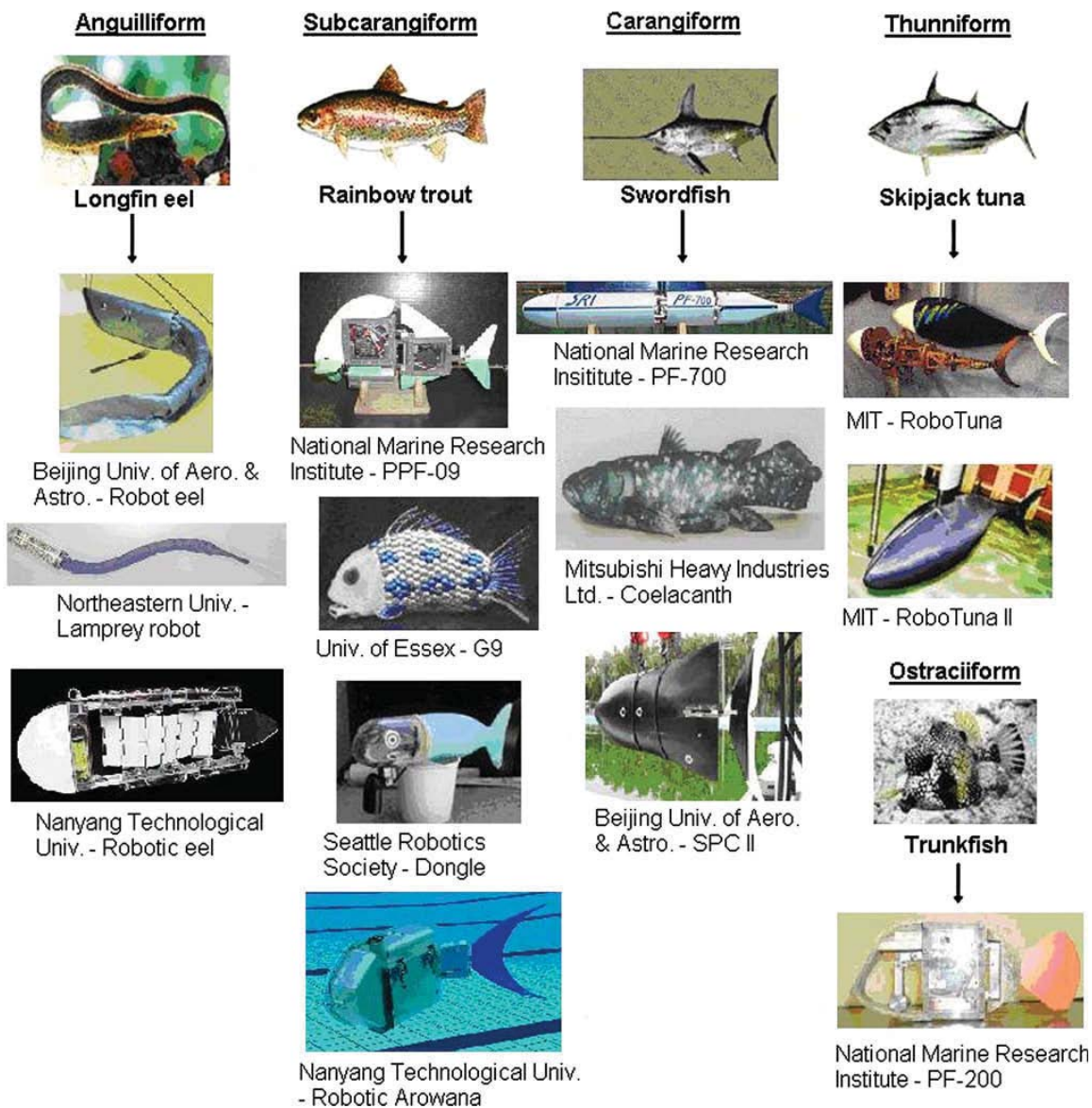


Figure 2.7: Examples of biomimetic robots, the body and caudal fin (BCF) locomotion modes they mimic, and the groups that developed them [5].

Research work has focused on the development of biomimetic fish robots, particularly those whose primary source of thrust generation comes from undulatory movements of the body and caudal fin. This movement is the BCF locomotion (see above). Mimicry of these locomotion techniques comes easier than other more complex locomotion schemes. An oscillating tail fin is all that's needed while the effectiveness of the biomimicry can be increased with the additions of functional pectoral fins and flexible bodies. Many robots have been designed to take advantage of these movements are design to replicate them through the use of conventional motors and actuators. An overview of these efforts can be seen in Fig. 2.7. The diagram identifies the targeted swimming mode and the groups that developed the robotic system.

Similar efforts have been made incorporating various types of active materials to produce the motion. These active (smart) materials bend in response to electrical stimuli. Those that are most actively used for underwater bio-inspired robots are shape memory alloys (SMA), polypyrrole based conductive polymer , and ionic polymer metal composites. In [29] shape memory alloys have been used to a robotic fish capable of sub-carangiform motion while rajiform locomotion was demonstrated with a manta ray robot in [30]. Utilization of polypyrrole conductive polymers is less widespread, however, a ostraciiform style robot was successfully developed in [31]. Ionic polymer metal composites are much more prominent and common sight in the research community that is developing bio-inspired robotic systems. IPMC actuators have been much more keenly integrated into robotic systems such that these systems emulate the movement of fish [13, 32–36], jellyfish [37], manta ray [38], and other aquatic and non-aquatic animals [39, 40].

Of the robotic systems presented here that mimic the locomotion techniques of fish several that feature conventional technologies have active elements (pectoral fins) outside of the caudal fin. For the systems featuring smart materials in an active

roll a caudal fin is the sole source of propulsion and maneuvering. This lack of pectoral fins is insignificant with respect to thrust production. However, significant gains maneuverability of robotic systems can be substantially improved with the addition of active fins aside from the caudal fin. These gains, when coupled with those already realized by mimicry of fish locomotion modes, can substantially improve the performance of current smart material based robotic systems.

In order to reproduce these swimming modes accurately robotic systems must be capable of complex bending and twisting motion. Electric motors, servos, and linear actuators make replication of required motion difficult, and require complex mechanical linkages. Active (smart) artificial muscle type materials are one enabling technology that can deform under electrical stimuli, therefore producing complex bending and twisting motion for propulsion and maneuvering. These materials do not require heavy or complex auxiliary components. For this reason, active materials have been identified as perfect candidates for biomimetic robotic applications as will be discussed in the following section.

2.4 Ionic Polymer Metal Composites for Under-water Propulsion

Internal combustion engines, electric motors, hydraulics, and pneumatic methods of providing useful movement to robotics applications has long been the standard. Deficiencies in these current technologies providing actuation forces makes it difficult to reproduce the complex, smooth, fluidic movements generated by muscle like those seen exhibited by biology in nature [41]. To replicate motions such as these sophisticated linkages are required, complicating the system and making for expensive design. In addition, few conventional motors compare to muscle in force and torque genera-

tion to weight ratios [41]. To fill this void, research and development in a family of materials known as electroactive polymers (EAPs) has been conducted. An exciting ionic subclass of this group known as ionic polymer metal composites has the ability to produce large deformations in response to relatively low input voltages and as such has been identified as having significant potential, specifically for underwater applications.

Ionic polymer-metal composite material is one of the most promising active (smart) materials for developing novel soft biomimetic actuators and sensors, preferably for underwater applications [7–9, 42]. Notable advantages of the IPMC include low driving voltage (<5 V), relatively large strain, soft and flexible structure, and the ability to operate in an aqueous environment (such as water). Researchers over the past two decades have made significant advances in the manufacturing, modeling, design, control, and application of IPMCs for both actuation and sensing (e.g., see [8, 10, 15, 43–51]). Even energy harvesting applications in air and aqueous environments have exploited the unique properties of IPMCs [52–54].

An IPMC consists of a neutralized ionomeric membrane sandwiched between noble metallic electrodes as shown in Fig. 2.8. When the composite is saturated in a polar solvent (such as water) and then an electric field is applied across the electrodes, the composite bends. The bending is caused by induced swelling on the cathode side of the composite and shrinking on the anode side [see Fig. 2.8(b)] due to a sudden flux of cations and polar solvent (such as water). An oppositely applied voltage causes bending in the opposite direction. Conversely, when an IPMC is mechanically deformed, charges develop on the electrodes and thus IPMCs can function as current or voltage sensor [10, 15].

IPMCs can be applied in many unique applications. For example, due to their biocompatibility, IPMC actuators have been used to design biomedical devices such

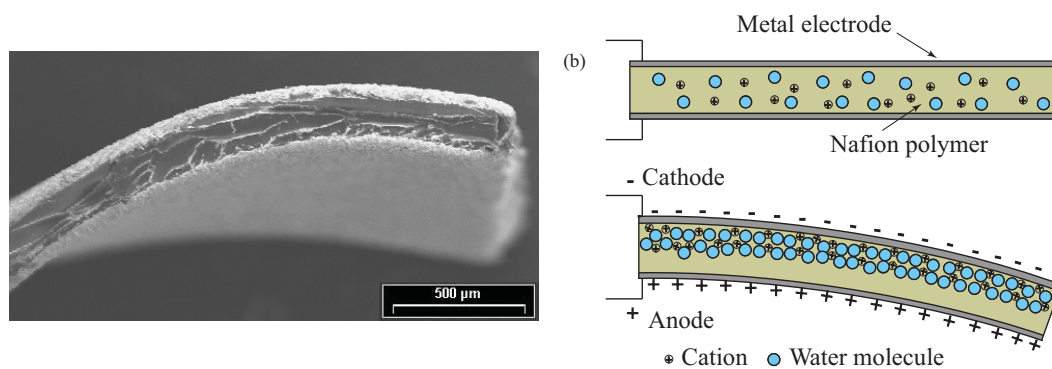


Figure 2.8: (a) Scanning electron microscope image of the cross-section of a Nafion-based IPMC. (b) Illustrative movement of cations and water molecules inside of an IPMC.

as active endoscopes [55] and smart catheters [56]. Strips of IPMCs can be used as sensors in hand prostheses [57]. One of the most promising applications is innovative propulsion systems for underwater autonomous systems [11, 13, 14, 32, 33, 58]. Specifically, IPMCs can replace or enhance the design of propulsors for underwater walking and swimming machines that are currently based on traditional actuators such as DC motors [25, 59–63], pneumatic actuators [64], and magnetic actuators [65]. As previously mentioned, strips of IPMCs have been used to construct artificial tentacles for a jellyfish-like robot [19] and other bio-inspired systems [13, 21, 33]. In some cases, IPMCs offer comparable performance to traditional actuators.

Bending motion is the most commonly studied and applied for IPMCs [11]. Particularly, when an IPMC strip is mounted in the cantilever configuration, with one end fixed and the other free, an applied electric field across the IPMC causes the actuator to bend as illustrated in Fig. 2.9(a). This single degree-of-freedom bending motion has wide applications, such as a single-link [33] and multi-link [66] oscillatory propulsor. However, IPMCs with multiple degrees-of-freedom are highly desirable to create control surfaces which can undergo complex motion and deformation, for both station-keeping [67] as well as propulsion and maneuvering. It has been observed that

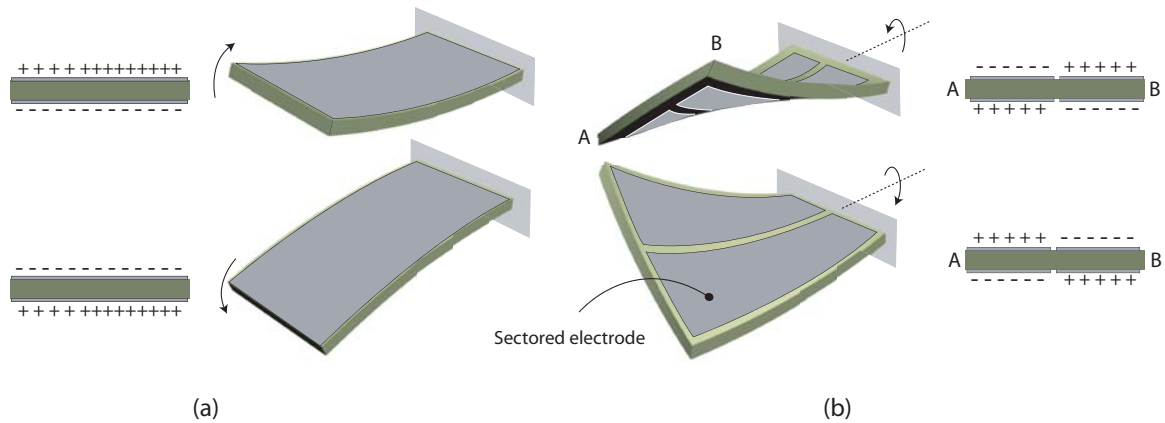


Figure 2.9: IPMC AM fin motion: (a) bending and (b) twisting.

the propulsion and maneuvering capabilities of the Bluegill (*Lepomis macrochirus*) sunfish is primarily due to its highly deformable pectoral fin [60]. Thus, multiple degrees-of-freedom IPMC actuator technology offers many avenues for mimicking such behavior to create more efficient and maneuverable underwater systems. Recently, sectored (patterned) IPMC as depicted in Fig. 2.9(b) have been developed to realize twisting motion [18]. Particularly, by carefully creating electrodes on the surface of the polymer with proper electrical isolation between adjacent units, sections of the AM fin can be independently controlled to achieve complex shapes and deformations.

Herein, a recently developed IPMC artificial muscle (AM) fin with patterned electrodes is characterized for underwater propulsion and maneuvering. It is pointed out that with careful design the electrodes on certain areas of the IPMC fin can be patterned to create a highly deformable control surface, while at the same time other regions can be pattern for sensing [68] fin deformation and responses to external stimulation. The final result is a compact monolithic control surface with integrated sensing for multifunctional applications in a wide spectrum of micro-autonomous robots and marine systems.

2.5 Summary

This chapter covered the fundamentals of underwater locomotion, reviewed current state-of-the-art man-made robotic systems, and presented the basics of an active material known as ionic polymer-metal composite. The IPMC is used in this work to mimic the propulsion characteristics of aquatic animals, and the sectored-electrode IPMCs are characterized to determine their performance for underwater systems.

Chapter 3

Experimental System

This chapter describes the experimental IPMC system, including IPMC fabrication, electrode patterning process, and hardware development.

3.1 IPMC Fabrication Process

Ionic polymer metal composites consist of a polymer substrate sandwiched between two conducting noble metal layers, such as platinum. The substrate typically consists of a fluoropolymer ion exchange membrane; the two most common being Nafion[®] by Dupont, or Flemion by Asahi Glass [69,70]. Otherwise known as an ionomer, this substrate is then doped by soaking in an aqueous solution of positively charged cations, typically metallic salts like Na⁺ or Li⁺. The fabrication of IPMCs is a time consuming procedure with several variations in the process as well as recipe of the elements used. The general process is depicted in Fig. 3.1 and discussed below.

The ionomer membranes used to produce IPMCs, like Nafion[®] are widely available for purchase today. However, the membrane thickness is limited to what is available from suppliers. In [71] a solution recasting method was proposed and verified that allows for modification of the membrane's thickness.

The IPMC-based propulsors are created from 0.5-mm thick prefabricated ionic fluoropolymer (Nafion[®]) membrane. The 0.5-mm thickness is chosen to achieve a good

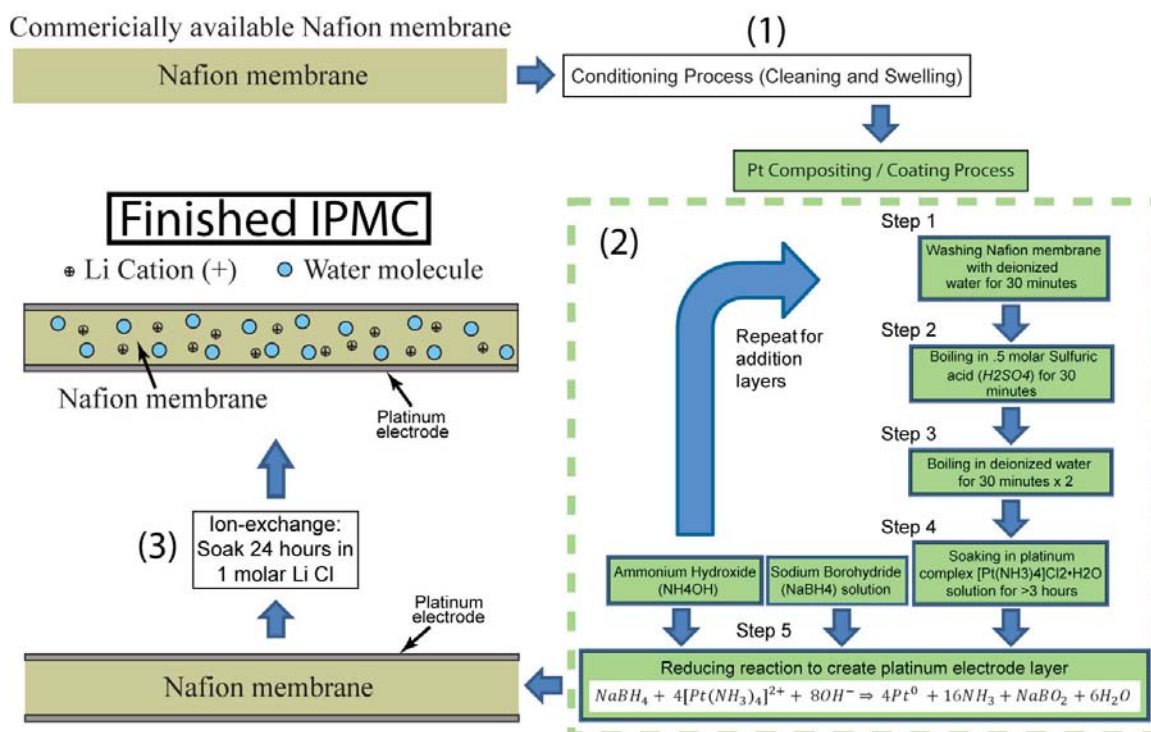


Figure 3.1: The above figure depicts the fabrication process that starts with a piece of commercial Nafion membrane and ends with a fully functional IPMC.

balance between deflection and actuation force [8]. The IPMC fabrication process consists of three parts, the first being a conditioning process to clean the sample for electroless plating. Next the sample is soaked in a platinum complex solution, tetraamineplatinum (II) chloridemonohydrate ($[Pt(NH_3)_4]Cl_2 \cdot H_2O$), for several hours. The platinum is then metalized on the membrane surface via a reduction process to create electrodes on the Nafion[®] membrane. The IPMC propulsor is then cleaned in a aqueous solution of sulfuric acid (H_2SO_4) and the reduction and cleaning processes are repeated until a sufficiently low surface resistance is achieved [8]. Lastly, the IPMC is hydrated with a salt solution to introduce mobile cations, Li^+ , in a process known as ion-exchange.

3.1.1 Surface Machining Technique: Sectoring

The sectored electrodes for the twistable IPMC AM fin can be created by masking, surface machining, or ablating the electrode using a high-power laser. The first approach involves the use of a mask to cover areas of the membrane that should not be exposed to the platinum-plating process, subsequently creating an isolation region between adjacent electrodes. The second approach uses a precision computer-controlled milling machine to mechanically remove the platinum electrodes from the surface of an IPMC membrane to create the isolation region [18]. An alternative to both methods in which a flexible boot is created for housing multiple IPMC actuators to create a fin-type structure that can be controlled to offer bending and twisting motion is discussed and presented in Appendix A. This technique avoids the need to pattern the electrodes on the IPMC surface. The end product is a monolithic IPMC with isolated electrodes as illustrated in Fig. 3.2.

Masking Technique The masking technique to create IPMCs with sectored electrodes involves the use of UHMW Polyethylene tape (3M). The tape is used to cover specific regions of the bare Nafion[®] membrane to inhibit the plating of platinum on the surface of the membrane. For example, the tape is applied to the bare Nafion[®] membrane, then the taped Nafion[®] membrane is processed using the pre-treatment and plating process described above.

Machining Technique The surface machining method utilizes a computer-controlled milling machine, such as an automated circuit board router (e.g., ProtoMat S42, LPKF), to mechanically remove the plated platinum metal on the surface of the Nafion[®] membrane. The surface machining process is outlined in Fig. 3.3 and described as follows:

1. Create the machining path to create the electrode pattern using CAD software

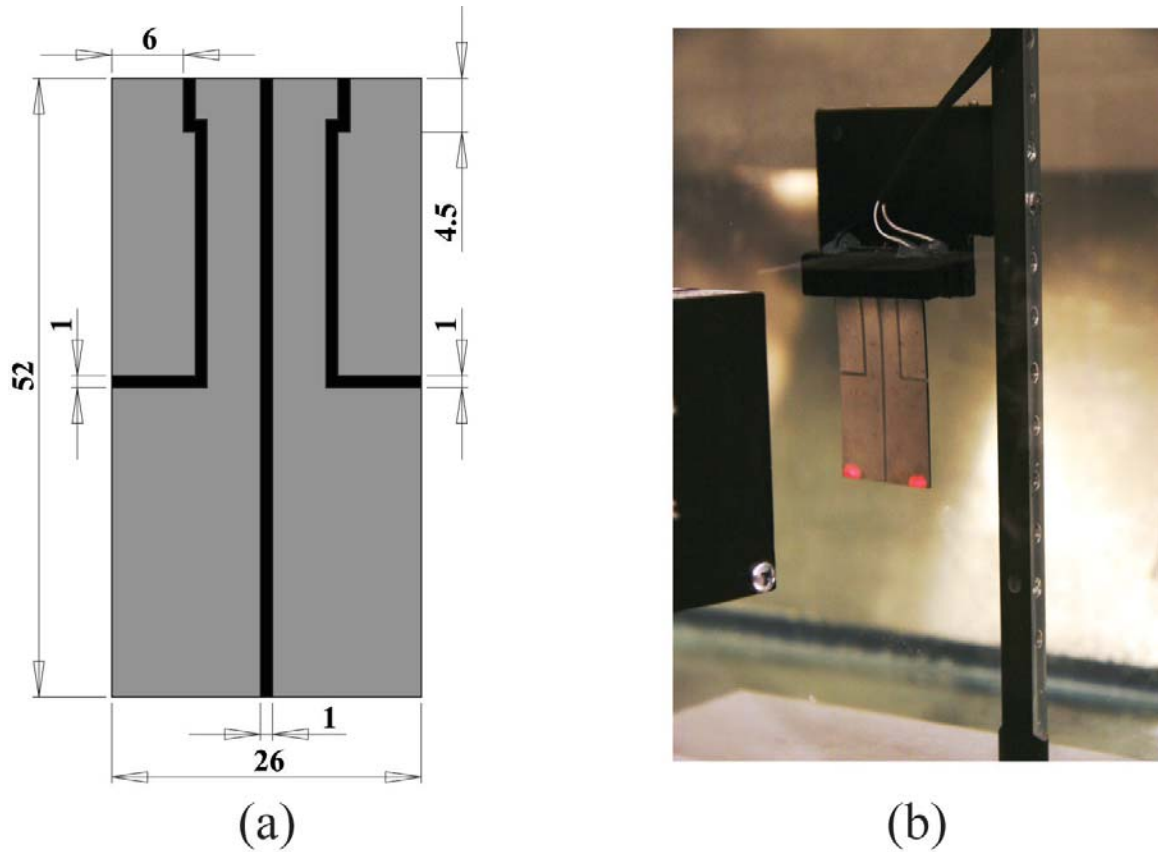


Figure 3.2: (a) Example patterned IPMC (units in millimeters) and (b) experimental setup for measuring bending/twisting response.

(e.g., Solidworks) or a circuit board layout program (e.g., Eagle, V5.6). The result of this step is a CAD/CAM file which is ran by the milling machine.

2. Attach an IPMC sample (with platinum electrodes) to the working surface of the milling machine using an adhesive layer, for example double-sided tape (see Fig. 3.3) or a vacuum system. Air bubbles trapped underneath the IPMC sample should be removed. Additionally, the locations of the corners of the IPMC on the working surface are marked for aligning the sample.
3. Load the CAD/CAM file onto the milling machine and start the milling process.
4. Remove the machined IPMC sample, then flip it over and attach the sample

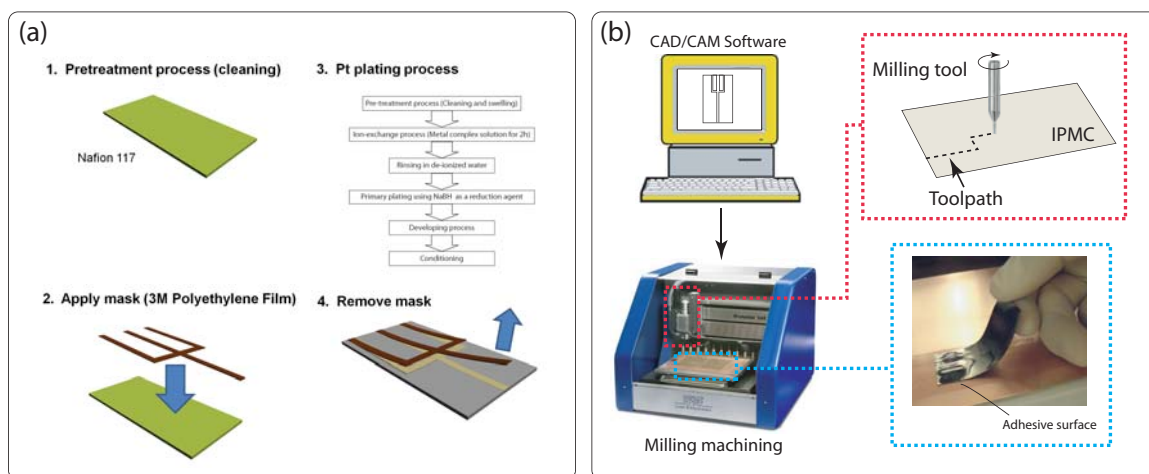


Figure 3.3: Electrode patterning process: (a) the masking and (b) the surface-machining technique.

to the working surface making sure the corners are aligned with the markings created in Step 2. Repeat Step 2 and 3.

5. Remove the machined IPMC sample and trim away excess material.

3.2 IPMC Enhancement - Gold Plating Process

Performance degradation of the IPMC actuators can occur over time from the loss of mobile Li⁺ cations as well as an increase in surface (electrode) resistance. The latter is a result of the platinum electrode surface developing cracks or voids from high levels of actuation or dehydration. Quick electroplating of gold to fill these voids and lower the surface resistance can “resurrect” these IPMCs or improve performance. A newly fabricated and an old, poorly performing IPMC are electroplated with gold using the previously described process (see Fig. 3.6). The newly fabricated IPMC had a surface resistance of 2.4 $\Omega/5\text{cm}$ before and 1.3 $\Omega/5\text{cm}$ after gold plating while the old sample had resistances of 14.1 $\Omega/5\text{cm}$ and 1.4 $\Omega/5\text{cm}$ before and after gold plating, respectively. The tip deflection and blocking force of the IPMCs are tested

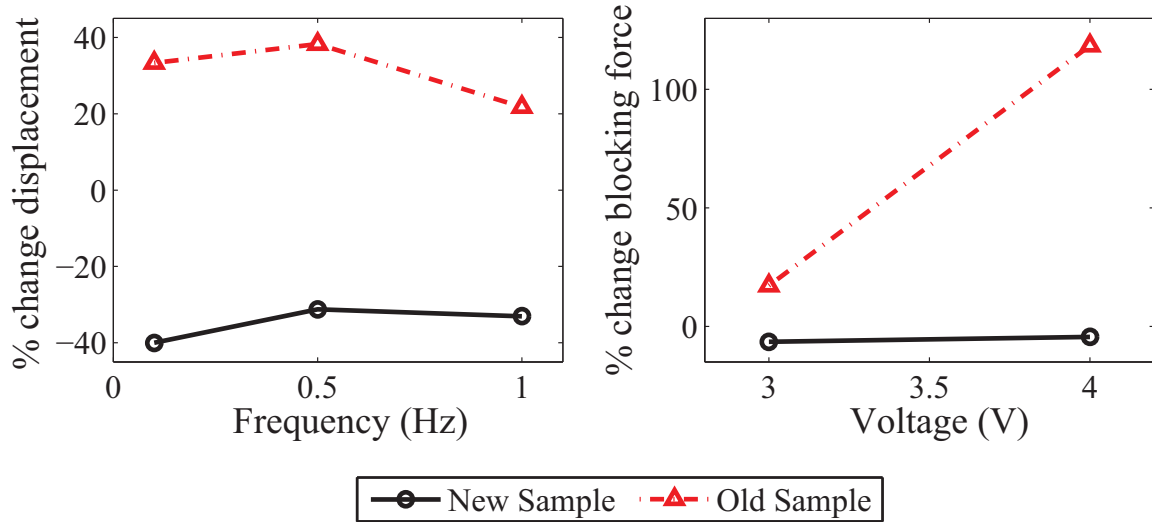


Figure 3.4: Displacement and force responses before and after Au plating.

before and after the plating process and the percent change after plating is shown in Fig. 3.4. The performance of an old sample that is rejuvenated by the gold plating process is shown in Fig. 3.5. The results show that electroplating is beneficial for old samples with degraded performance; both the displacement and blocking force are improved. In the case of a new sample with already good performance and low electrode resistance, no improvement is observed after electroplating the gold.

3.3 Electrical Contact Considerations

Typically, stainless steel or copper clamps, or conductive glues are used to establish an electrical connection to the IPMC electrode [72–74]. Conductive glue can be an effective method of connecting wires, but prolonged submersion in water may be undesirable and a separate clamping mechanism still must be devised to hold the actuator in place. Certain grades of stainless steel can be used as a contact material and provide great corrosion resistance but the material can be difficult to solder and must still be integrated into a mechanical clamping system. Copper’s superior

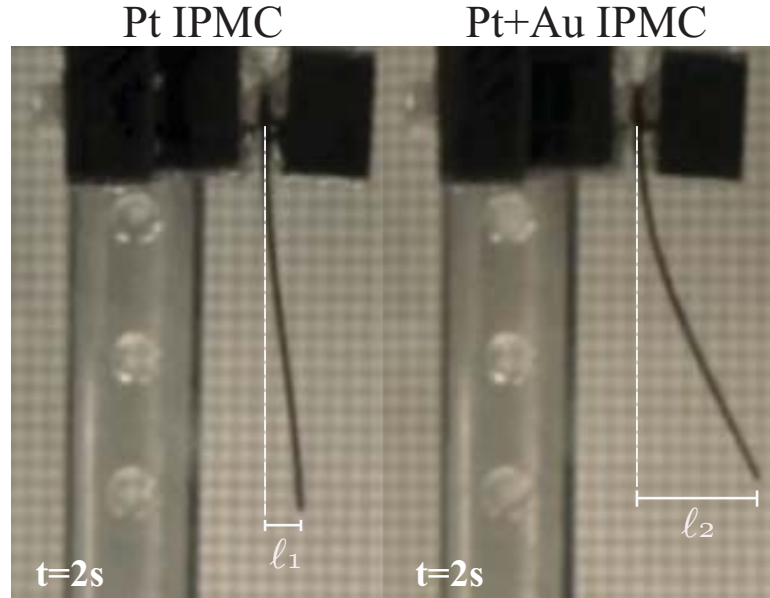


Figure 3.5: IPMC bending before (left) and after (right) gold plating.

conductivity is ideal but its low corrosion resistance makes submersion in water a problem. In [72], copper electrodes were sputter coated with platinum to prevent corrosion and any chemical reaction between the surface of the IPMC and the electrode. The process of sputter coating, however, is complex and few labs are equipped to perform the process. Therefore, the disadvantages of these methods illustrate the need for a simple mechanism and contact material to make good electrical contact with the IPMC actuator.

An all inclusive design incorporating nickel plated neodymium magnets was utilized in [31]. Similarly, in this work strong nickel plated rare earth neodymium magnets (NdFeB) are used as a multifunctional solution for clamping and power delivery. The magnets make for an easily removable clamp with a high clamping force of 0.4-0.8 lbf. The magnets used are typically electroplated with nickel and copper in the order Ni-Cu-Ni with each layer being approximately 5-7 μm . The magnets are quite modular in that they can easily be replaced or expanded by additional magnets placed

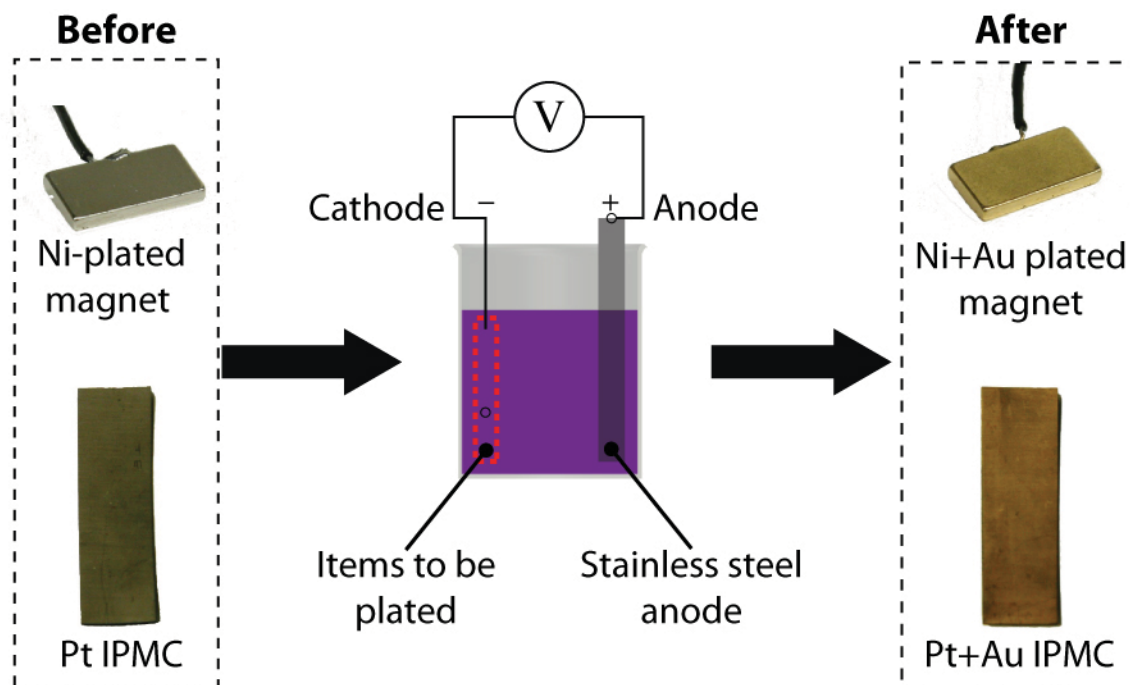


Figure 3.6: Electrodeposition process for Au plating magnets and IPMCs.

edge to edge.

The nickel coating is easily soldered to and is corrosion resistant. However, it was found that after prolonged submersion in water under an applied potential, breakdown of both the neodymium magnets' nickel surface and the IPMCs' platinum surface occurs due to the creation of a galvanic cell. This is exacerbated by the presence of voids in the nickel surface that expose the underlying copper layer and expedite the process. The differences in anodic potential between the platinum surface of the IPMC actuator and the magnet's nickel-copper surface can lead to degradation of electrical contact through chemical reduction of the platinum. To combat this problem, the nickel plated magnets are then electroplated utilizing a high quality gold plating solution to form a 1-2 μm layer of gold on the magnet's surface. In the process, neodymium magnet contacts are attached to a negative lead (cathode) and placed in a gold solution (see Fig. 3.6). A positive (anode) lead is connected to a strip of stainless

steel and a potential is applied. In the electrodeposition process the thickness of the resulting gold layer is determined by the current density and immersion time. The nickel then acts as a barrier layer and slows diffusion of copper atoms into the gold while the gold layer's low anodic potential minimizes the electrochemical reactions that damage the IPMC's platinum electrode.

3.4 Control Hardware

A custom voltage/current amplifier is developed to drive the IPMC actuator. Figure 3.7(a) and (b) show the circuit block diagram and fabricated circuit board for the amplifier, respectively. The amplifier is a class-B, emitter-follower design with feedback to minimize cross-over distortion [75]. In voltage mode, the voltage difference across the electrodes of the actuator is used as feedback information as shown in Fig. 3.7(a). In current mode, resistor R_s (1Ω , 5 W) functions as a current sensor. The measured unloaded bandwidth (-3.01 dB) in voltage mode exceeds 100 kHz . Likewise, the measured cross-over distortion at different input frequencies using a 1 V triangle input signal for a 4Ω resistive load is shown in Fig. 3.7(c). At frequencies less than 1000 Hz , the maximum cross-over distortion is less than 2% .

3.5 Displacement Sensor Calibration

Characterization of IPMCs required knowledge of the displacement of the actuator. To do this a non-contact reflection laser displacement sensor (SUNX Microlaser Sensor LM10) was used. The sensor uses a laser diode with a wavelength of 650 nm . It functions by radiating light from the diode to the target surface. The reflected light is detected by a receiver and converted to an analog voltage. To ensure consistent reading the laser sensor was calibrated using a reflective plate and a micrometer as

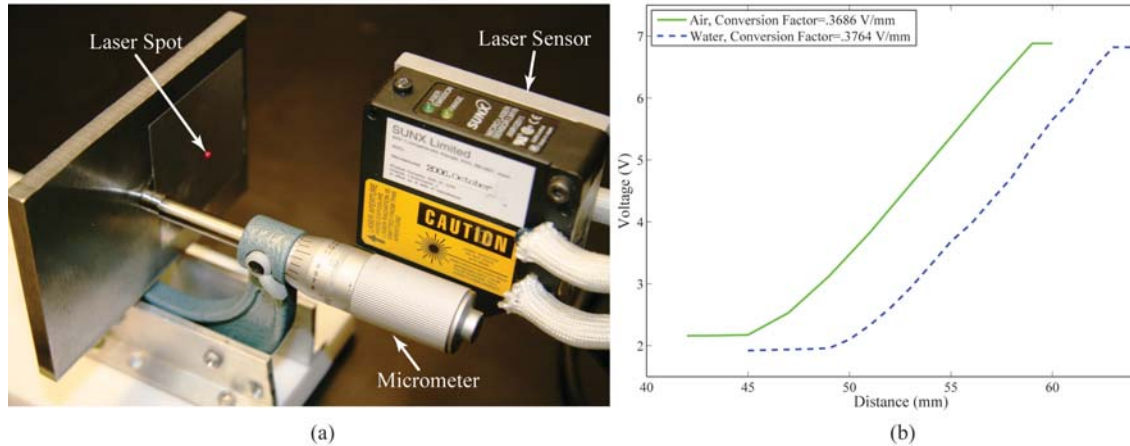


Figure 3.8: The experimental setup for (a) laser sensor calibration and (b) the resulting data.

shown in Fig. 3.8(a).

With the laser turned on the micrometer thimble was rotated to produce a travel of 1 mm displacement via the spindle. This process was repeated starting at the edge of the laser's range and continued until the plate was out of range. A similar process was performed in water as well. The results are shown in Fig. 3.8(b) and the results show the effective range of the laser sensor in water is shifted farther out. The difference is likely due to the laser light being diffracted when traveling through water. The laser had an effective range of approximately 10 mm where the voltage and displacement displayed a linear relationship. Calibration coefficients of 0.3686 V/mm in air and 0.3764 V/mm in water were found and used later to determine the IPMC displacement.

3.6 Drag Tank

To experimentally measure the drag coefficient of the finished prototype, drag tank experiments were performed. The drag tank consisted of a 6 ft \times 1 ft \times 1 ft acrylic tank with an overhead carriage and track. The six axis load cell (see Fig. 4.4) mounts

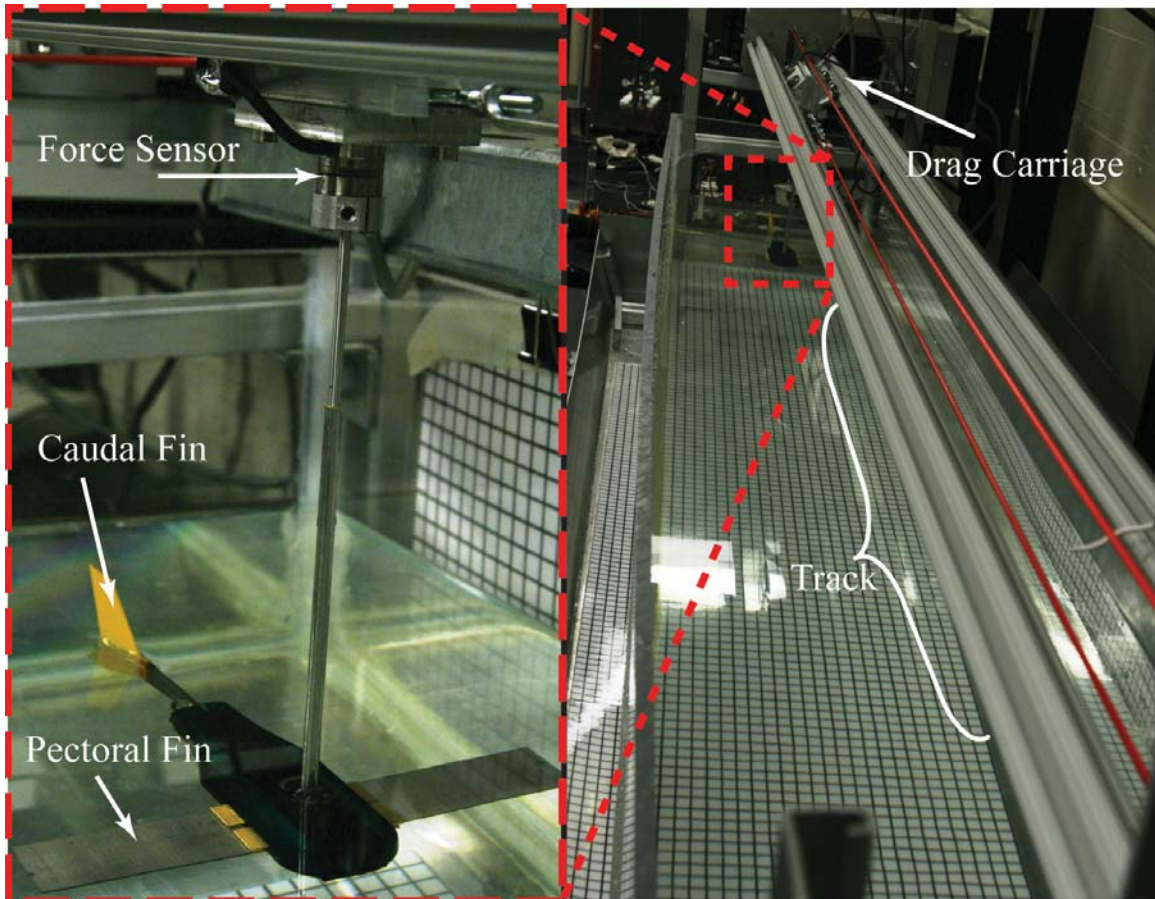


Figure 3.9: Left, the prototype similar to how it was tested for drag coefficient and Right, the drag tank and carriage system.

to the underside of the carriage and the body of interest is attached to the load cell. A 256-step per revolution stepper motor pulls the carriage along a track via a cable. The acceleration and speed of the carriage is controlled via Mach3 CNC controller software. Automatic stops were placed at either end of the tank to prevent driving the carriage too far and damaging the load cell. The experimental setup is shown in Fig. 3.9.

3.7 Summary

This chapter described the experimental IPMC system, including IPMC fabrication, electrode patterning process, control hardware development, laser sensor calibration, and experimental drag tank.

Chapter 4

Characterization

IPMCs demonstrate significant aptitude for producing smooth complex motion that is largely unrealized by conventional actuation techniques [41]. However, understanding the abilities of IPMCs with respect to blocking force, torque, bending, and twisting is essential to successful development of future platforms. Knowledge of operational characteristics allow accurate modeling and successful design. This chapter describes the characterization of sectored IPMCs for propulsion and maneuvering in underwater systems. The following chapter describes a bio-inspired robotic platform based on the IPMC actuators.

4.1 Twisting Response

It is necessary for IPMCs to bend and twist to realize propulsive movements that would be beneficial to any underwater vehicle or platform. The bending and twisting were studied for a monolithic IPMC with sectored electrodes. An alternative approach to create such motion is to use multiple IPMCs housed in a flexible medium. This approach was first proposed by Prof. Kim and David Pugal, Active Materials and Processing Laboratory (AMPL), and the method is summarized in Appendix A.

A single IPMC was processed using the technique discussed in Section 3.1.1 to produce four separate electrode pads; effectively creating four independently control-

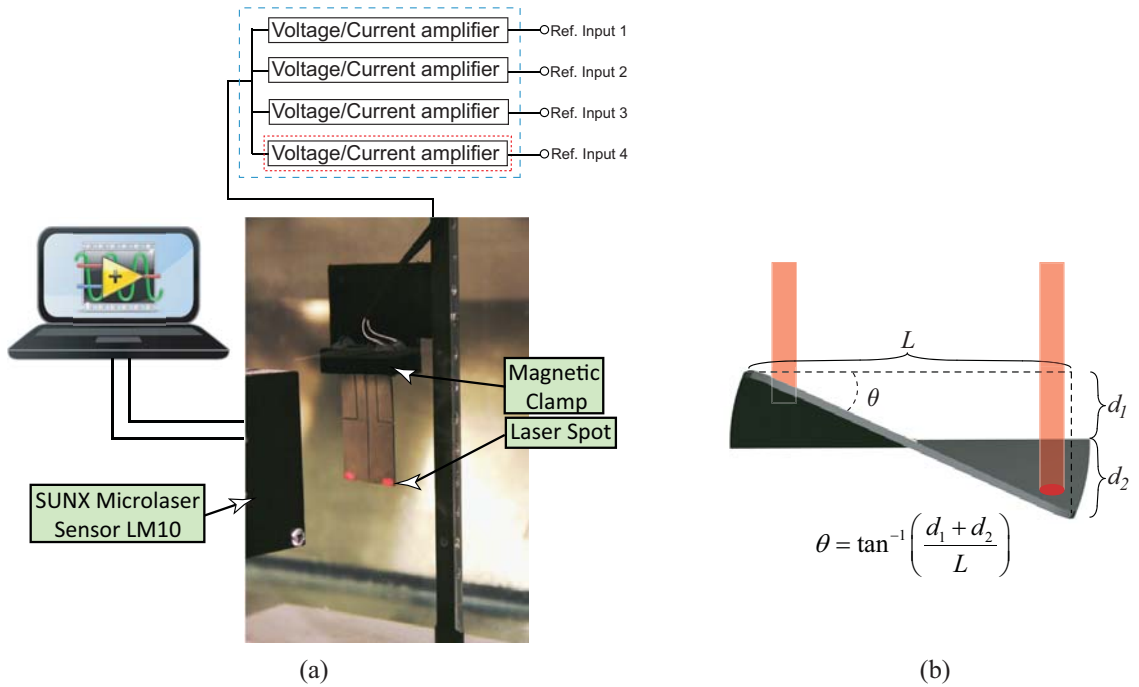


Figure 4.1: The achievable twist angle of a 4 sector IPMC was obtained using the (a) the experimental setup and (b) the definition of the twist angle where d_1 and d_2 are obtained by the laser sensors.

lable areas. Without these patterned electrodes, a conventional IPMC actuator is not capable of generating twisting motion. The IPMC was constrained and electrically driven via a custom made magnetic clamp. The experimental setup used and the method of calculating the twist angle is shown in Fig. 4.1(a) and (b) respectively. For this sectored IPMC [see Fig. 3.2(a)], twisting motion is generated by phase shifting the input signal of the left and right sectors (e.g., by 180 degrees) relative to each other. A custom-design National Instruments LabVIEW program is used to generate and output the actuation signal and monitor the IPMCs movement by means of a laser sensor (see Section 3.5). The displacement of IPMC was measured at two points equidistance form the center of the IPMC with a separation of 2 cm. Through these measurements the twist angle was then trigonometrically calculated as shown in Fig. 4.1(b). In the case of 180-degrees phase shifting, the patterned IPMC

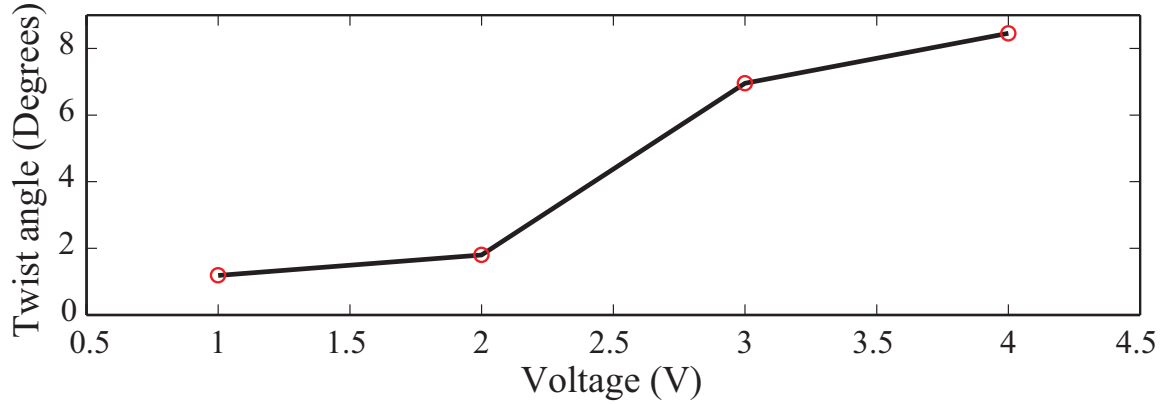


Figure 4.2: Twist angle of IPMC versus amplitude of DC input voltage.

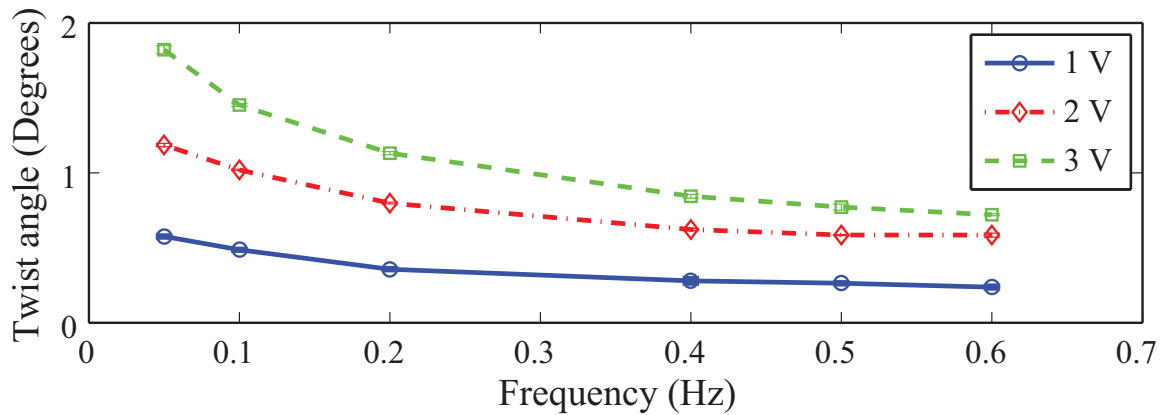


Figure 4.3: Twist angle verses input signal frequency (sinusoidal input).

achieved a maximum twist angle of 8.46 degrees under a 4-V DC input. Furthermore, it is found that the twist angle increased dramatically with increasing input voltages as well as decreasing actuation frequency (sinusoidal input). These trends are found in Fig. 4.2 and Fig. 4.3, showing the ability to produce practical twisting motion.

4.2 Blocking Force and Torque

Bending and twisting movements illustrate the potential use of IPMCs as both control surfaces and tools for active maneuvering. However, any control or maneuvering

forces generated are ultimately limited by the blocking strength of the actuator. The blocking force and torque are defined here as the maximum tip force or torque that can be generated by the actuator with zero deflection (displacement).

In [71], tip force, referenced as generative force (F_T), was found to increase with applied voltage, decrease with tip deflection, and display a cubic relationship with membrane thickness that could be explained by Hooke's Law. Since relatively thick Nafion[®] membrane is not readily available, researchers have explored the solution casting process [76–79] and the hot pressing technique [80]. The output force enhancement for thicker IPMCs is evident by considering two IPMC strip actuators, both having the same length, width, but each have a different thicknesses, such as t and $2t$ (twice as thick). Assuming that for both actuators, the same tip displacement is required, then the required strain for the thick actuator is 2ϵ . As the stress tensor for linear beam with thickness of t , width b , and length L can be expressed [76]

$$\sigma_t = \frac{6F_t L}{bt^2}, \quad (4.1)$$

the ratio of the stresses is

$$\frac{\sigma_{2t}}{\sigma_t} \approx 2 = \frac{F_{2t}}{2^2 F_t}, \quad (4.2)$$

hence $F_{2t} = 8F_t$. Therefore, a thicker IPMC will produce a larger blocking force.

The tip force again was characterized for surface resistance and effective bending length parameters in [72]. Herein the blocking force and blocking torque are experimentally obtained for the sectored IPMC seen in Fig. 3.2(a).

A six-axis load cell (ATI Industrial Automation Nano17-Ti, with resolution down to 0.149 mN of linear force and 0.0069 Nmm torque) was introduced used to measure forces of interest. A stiff 1/8-inch diameter rod made of 304 stainless steel is used for

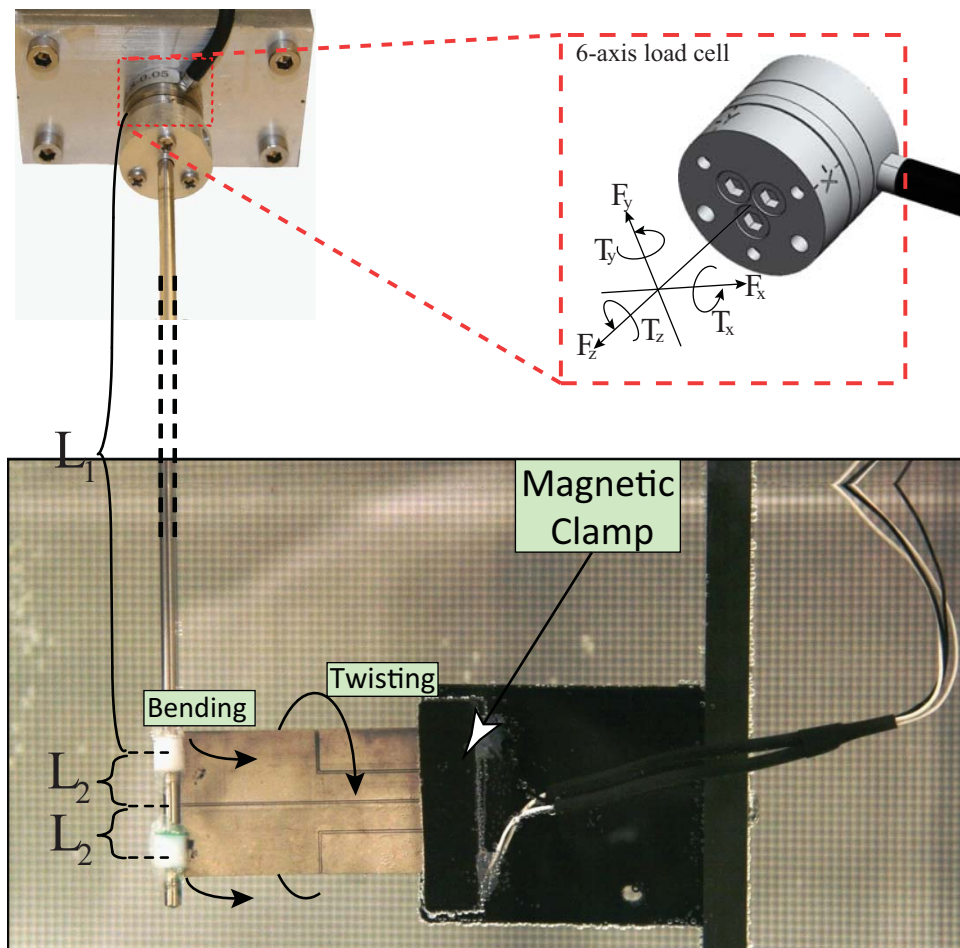


Figure 4.4: Experimental setup for measuring the blocking force and torque of a sectored IPMC

mechanical amplification of tip force. The load cell's coordinate system as well as the experimental setup are shown in Fig. 4.4, where a magnetic-based clamp is used to hold the IPMC in the desired location and provide electrical power. The measured torque about the x -axis, T_x shown in Fig. 4.4, is used to resolve the blocking force and blocking torque. The sectored IPMC was actuated in either a bending or twisting fashion and where the blocking force was calculated by,

$$T_x = F_B \cdot (L_1 + L_2)$$

$$F_B = \frac{T_x}{(L_1 + L_2)}$$

and the blocking torque by,

$$T_x = F \cdot L_1 - F(L_1 + 2L_2)$$

$$F = \frac{T_x}{2L_2}$$

$$T_B = 2F \cdot L_2$$

$$T_B = 2 \frac{T_x}{2L_2} \cdot L_2$$

$$T_B = T_x$$

A sinusoidal input voltage of 1-, 2-, and 3-V amplitude is applied to the IPMC to obtain the blocking force; and a 2-, 3-, and 4-V amplitude signal is applied for the blocking torque. The input frequency range is from 0.05 Hz to 2 Hz. The same voltage is applied to all electrode pads to measure blocking force while in the case of generation blocking torque, the left and right electrodes are phase shifted by 180 degrees. The results for blocking force and blocking torque are presented in Fig. 4.5 and Fig. 4.6, respectively. Both blocking strength characteristics are found to increase with decreasing input frequency. However, two separate growth regimes are observed on either side of a threshold of about 0.2 Hz. At frequencies greater than 0.2 Hz, the blocking force and torque exhibited quasi-linear growth with decrease frequency while

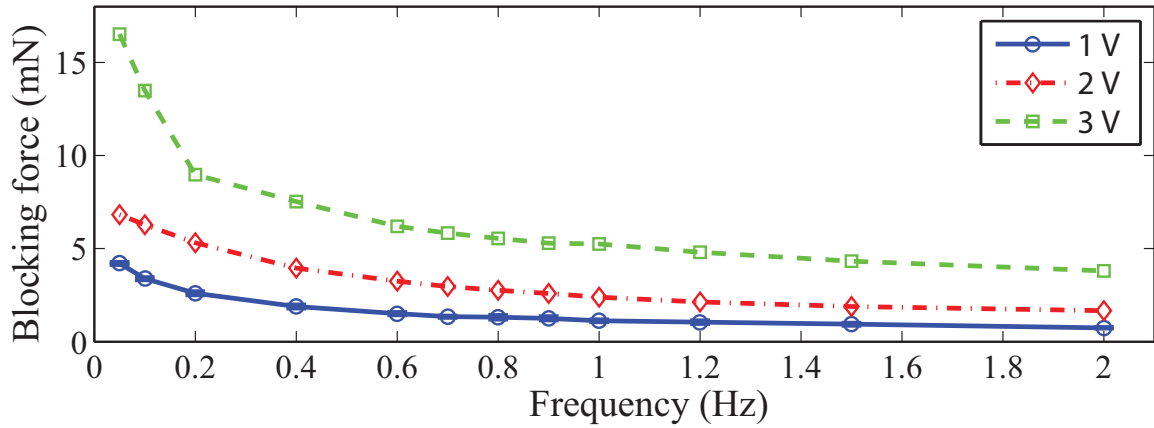


Figure 4.5: Bending force of sectored IPMC versus input signal frequency.

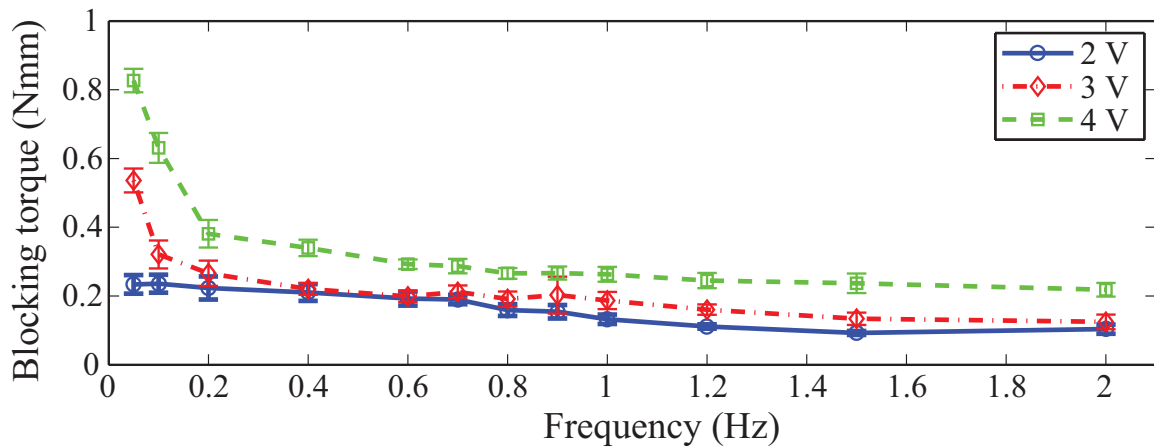


Figure 4.6: Blocking torque of IPMC versus input signal frequency.

at frequencies less than 0.2 Hz, there is rapid increase of these loads. This behavior can be attributed to the fact that the transient response of mobile cations induce stress, and in effect tip force and torque. The maximum blocking torque measured is 16.5 mN at 3 V and the maximum blocking torque is 0.83 Nmm at 0.05 Hz.

4.3 Propulsion Characteristics

Existing underwater propulsion systems are currently dominated by conventional propeller designs. On the contrary, bio-inspired designs are still in the infant stage. With respect to underwater locomotion, substantial improvements can be made in the areas of efficiency and maneuverability by mimicking biological forms of locomotion [28]. IPMCs can be exploited to replicate smooth motions seen in nature. Typical propulsion techniques employed by aquatic animals, particularly fish, feature flexible foils in combination with motions such as flapping, heaving, or both. The tail, or caudal fin, is the primary propulsor for most of these animals. In this section an IPMC in conjunction with a passive tail element (caudal fin) is tested for its ability to generate thrust.

For simplicity, consider an oscillating rigid tail fin as shown in Fig. 4.7, where the thrust force is defined as the resultant force in the x -direction and given by the equation:

$$F_{thrust} = \Sigma F_x = (F_r - F_d) \sin(\theta), \quad (4.3)$$

where F_r is the reaction force due to fin movement, F_d is the drag on the oscillating fin, and θ is the oscillation angle. With this in mind a conventional IPMC sample connected to a trapezoidal caudal fin [Fig. 4.13(a)] is tested to verify the ability to extrapolate thrust force from the experimental setup. The fin is secured to the IPMC with Kapton[®] polyimide film tape. Kapton[®] tape is chosen for its silicone adhesive that is more water resistant than conventional acrylic or rubber adhesive tapes. A nylon block featuring neodymium magnet clamps is installed at the end of the stainless steel rod while the rod itself is secured to the load cell via a set screw. The IPMC-caudal fin assembly is secured in the magnetic clamps and actuated in water. The experimental setup with the load cell is illustrated in Fig. 4.8. The thrust

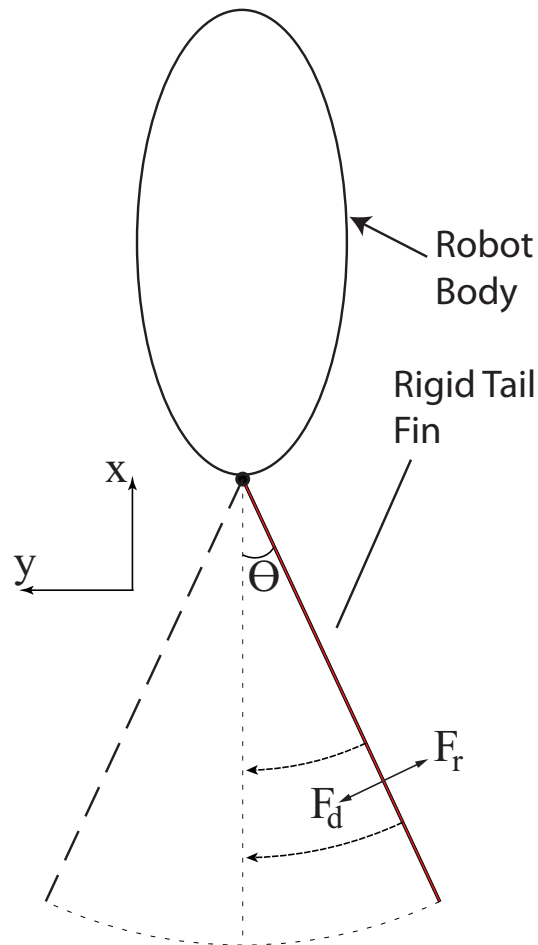


Figure 4.7: Diagram of an oscillating rigid tail fin.

force was then backed out from the torque measured about the load cells x-axis by,

$$T_x = F_T \cdot L$$

$$F_T = \frac{T_x}{L}$$

The frequency response measured between the applied input voltage and resulting bending displacement is shown in Fig. 4.9. The resonance frequency is found to be 1.1 Hz. The fin is then actuated at its resonance and a thrust profile is obtained and plotted over the input voltage and IPMC deflection in Fig. 4.10. The per cycle thrust measurement profile is compared to experimental results obtained in [33, 81],

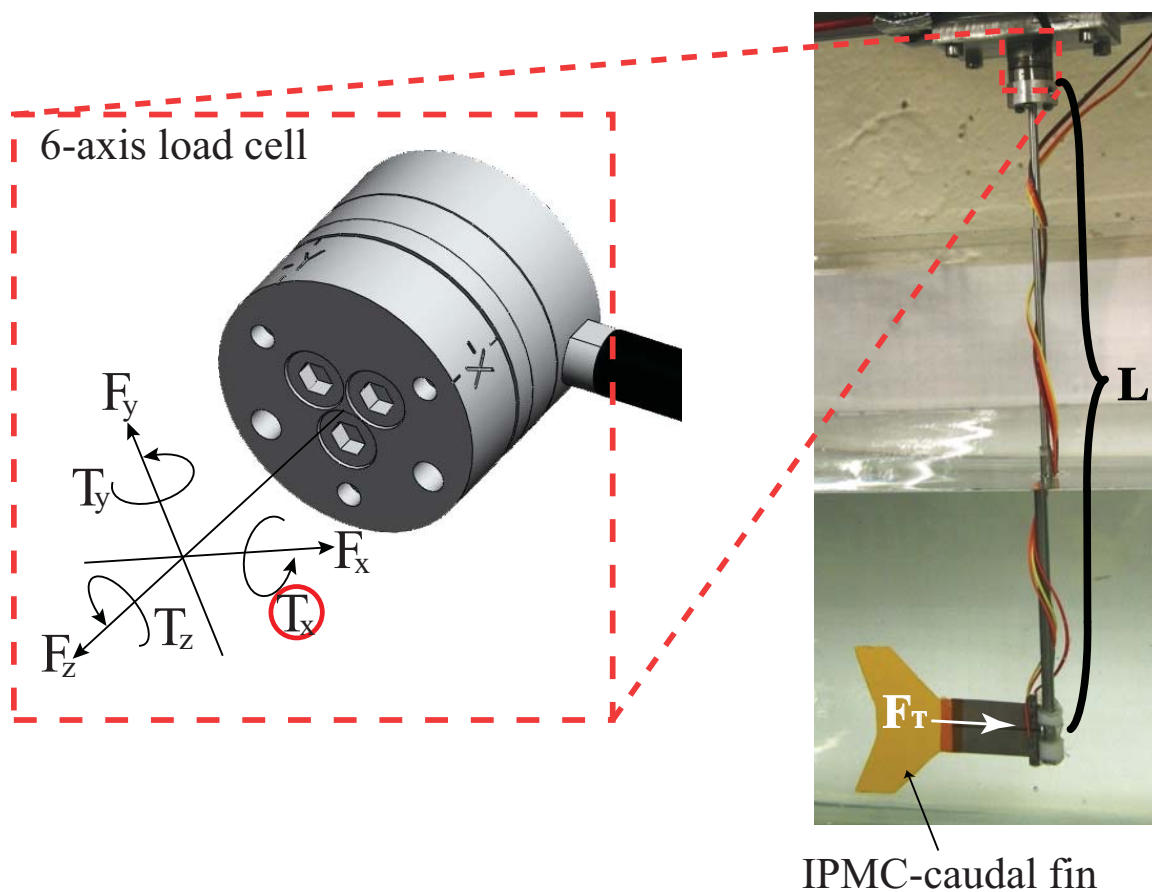


Figure 4.8: Experimental setup used to measure the thrust of IPMC and caudal fin tail assembly.

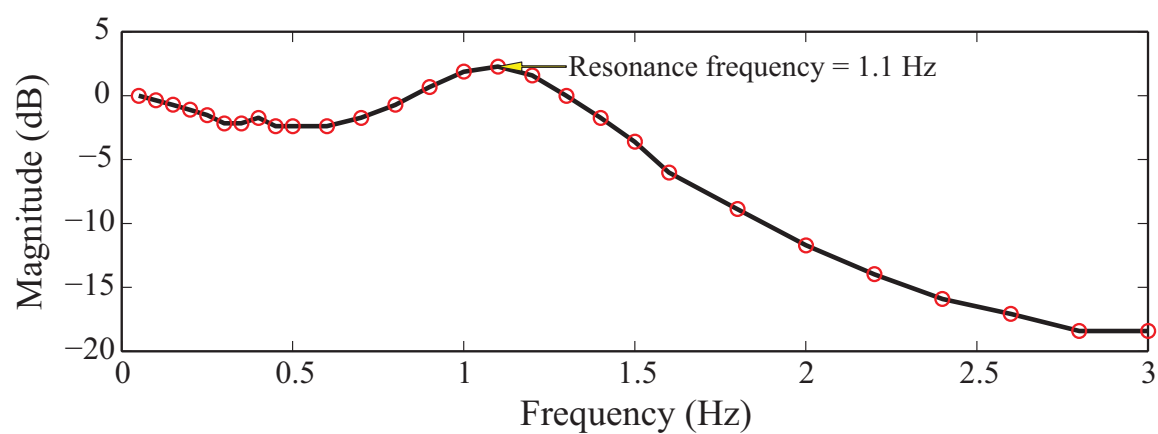


Figure 4.9: Frequency response of conventional IPMC with attached passive caudal fin.

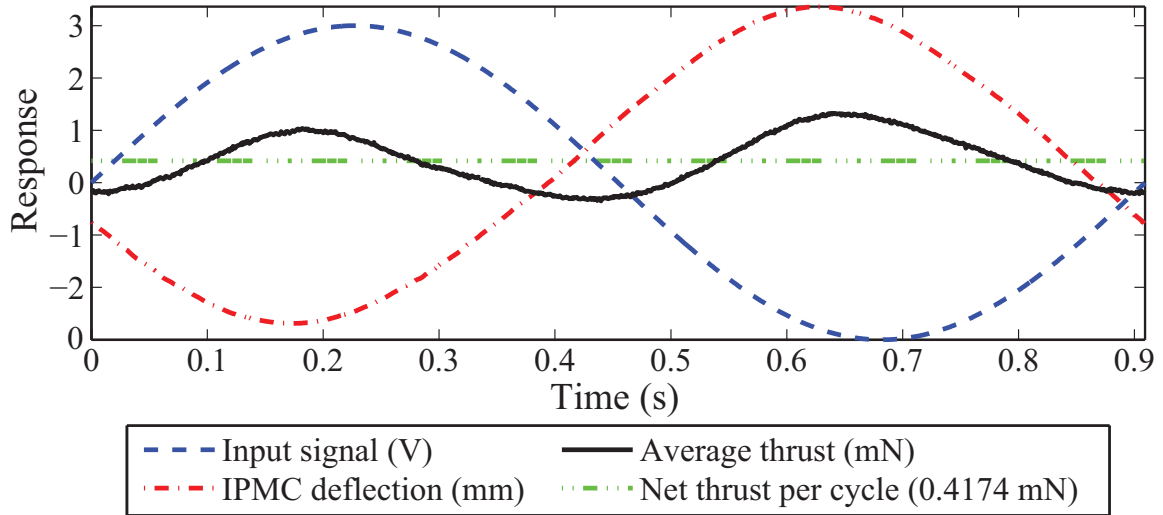


Figure 4.10: Thrust response of conventional IPMC with caudal fin when driven by a 3-V, 1.1-Hz sine wave at resonance.

numerical simulation analysis performed in [60,82], and predicted results from models in [83,84]. Correlating behavior is found on two counts: the frequency of the thrust being twice that of the IPMC actuation frequency, and the thrust and IPMC deflection are found to have values of zero simultaneously. The latter of which agrees with the diagram shown in Fig. 4.7 which shows that when $\theta = 0^\circ$, there is no resultant component in the x -direction. Two other behaviors are also consistent with expected system behavior. First, the peak thrust is found shortly after inflection points of the IPMC deflection; given the thrusts dependence on both θ and the velocity of the fin. Second, one would expect a 180-degree phase lag between the input signal and the IPMC deflection at resonance. By inspection of Fig. 4.10, a phase lag of nearly 180 degrees is observed.

With thrust verified the assembly was then actuated at three different voltage levels with a sinusoidal input waveform over the frequency range between 0.2 Hz to 2 Hz; this was found to cover the boundaries of reasonable thrust production. For each actuation frequency the thrust, and power consumption were measured

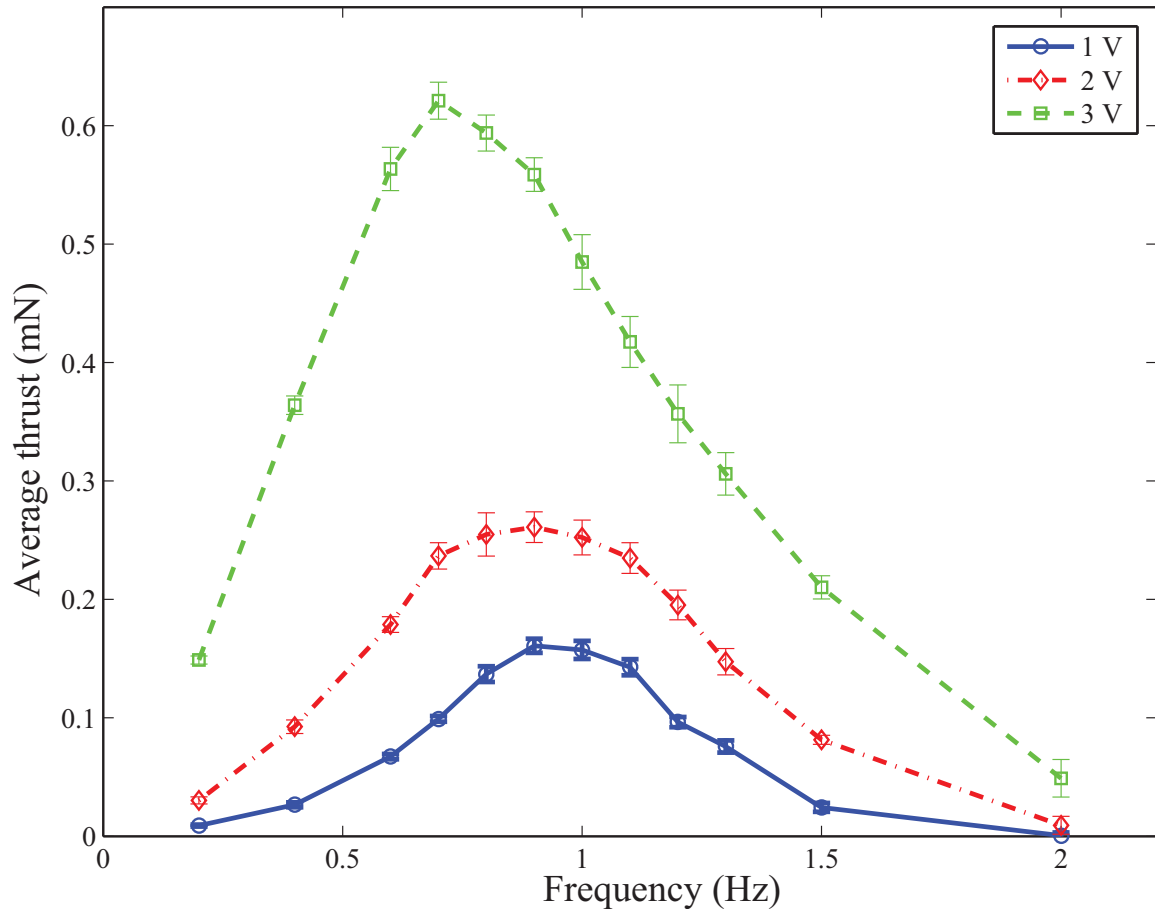


Figure 4.11: Average thrust of conventional IPMC-Caudal fin assembly when actuated by a sinusoidal input.

with a LabVIEW program that had been developed. A custom Matlab program then processed the entire frequency sweep. At each frequency a minimum of eight actuation cycles were averaged together. The maximum thrust was found to have a slight dependence on input voltages. Increasing the amplitude input voltages appears to slightly shift the peak thrust value to lower frequencies however more testing will need to be done to confirm this trend. The maximum value reported was 0.67 mN at 0.7 Hz (see Fig. 4.11). This value can be raised significantly by increasing the applied potential further.

The effect of the shape of input waveforms on thrust production was then inves-

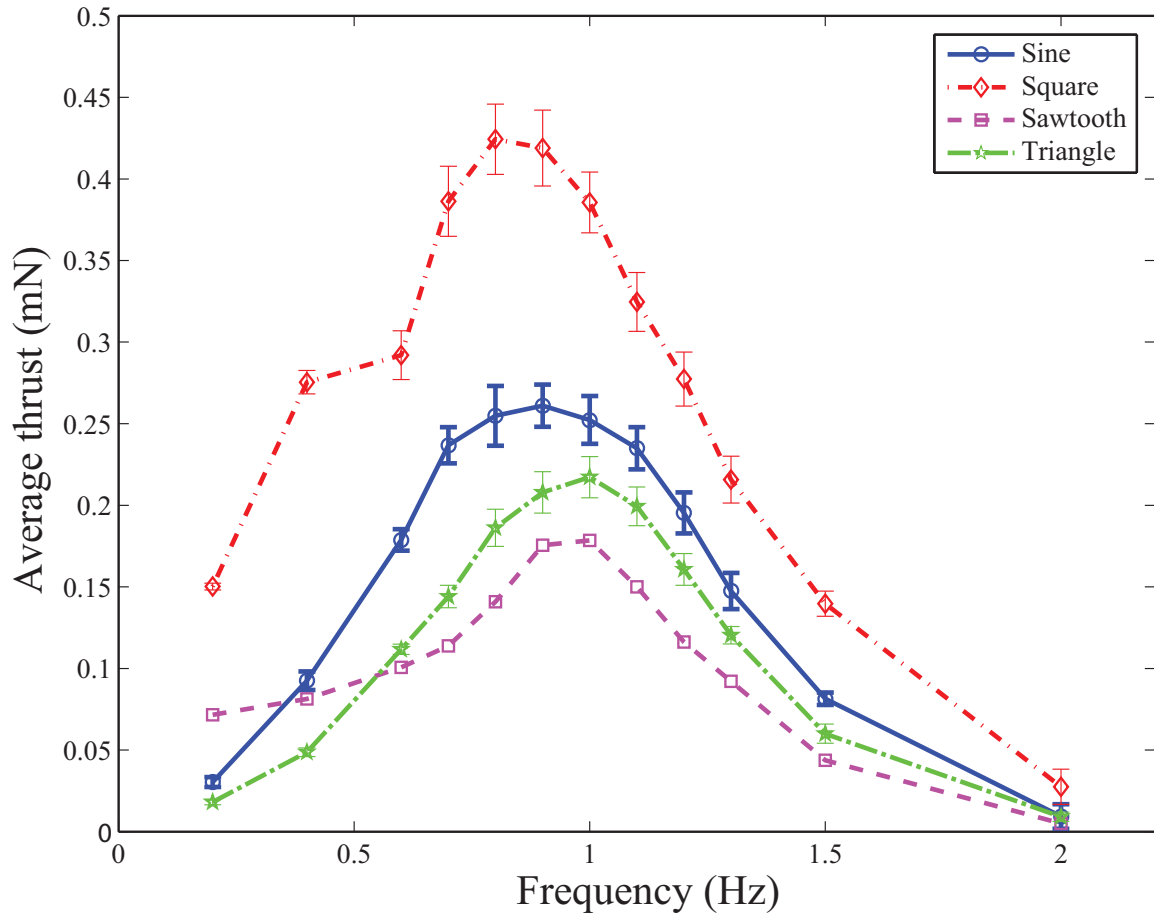


Figure 4.12: Thrust production of assembly in Fig. 4.13a when actuated by different input waveforms at 2 V.

tigated. The four wave forms used were sinusoidal, square, sawtooth, and triangle waves. All of the signals used had a 2-V amplitude. The largest thrust production was found to be 0.42 mN was generated by the square waveform at 0.8 Hz. A sine wave was found to be the second best with a peak value of 0.26 mN at 0.9 Hz. Both sawtooth and triangle waveforms were found to have similar profiles with respect to frequency albeit it with lower peak values found at 1.0 Hz (see Fig. 4.12).

The thrust force is again was experimental obtained sectored IPMC with two different caudal fin geometries. A conventional IPMC sample with dimensions of 21 mm \times 35 mm is bi-sectored to create one IPMC that consists of two separate

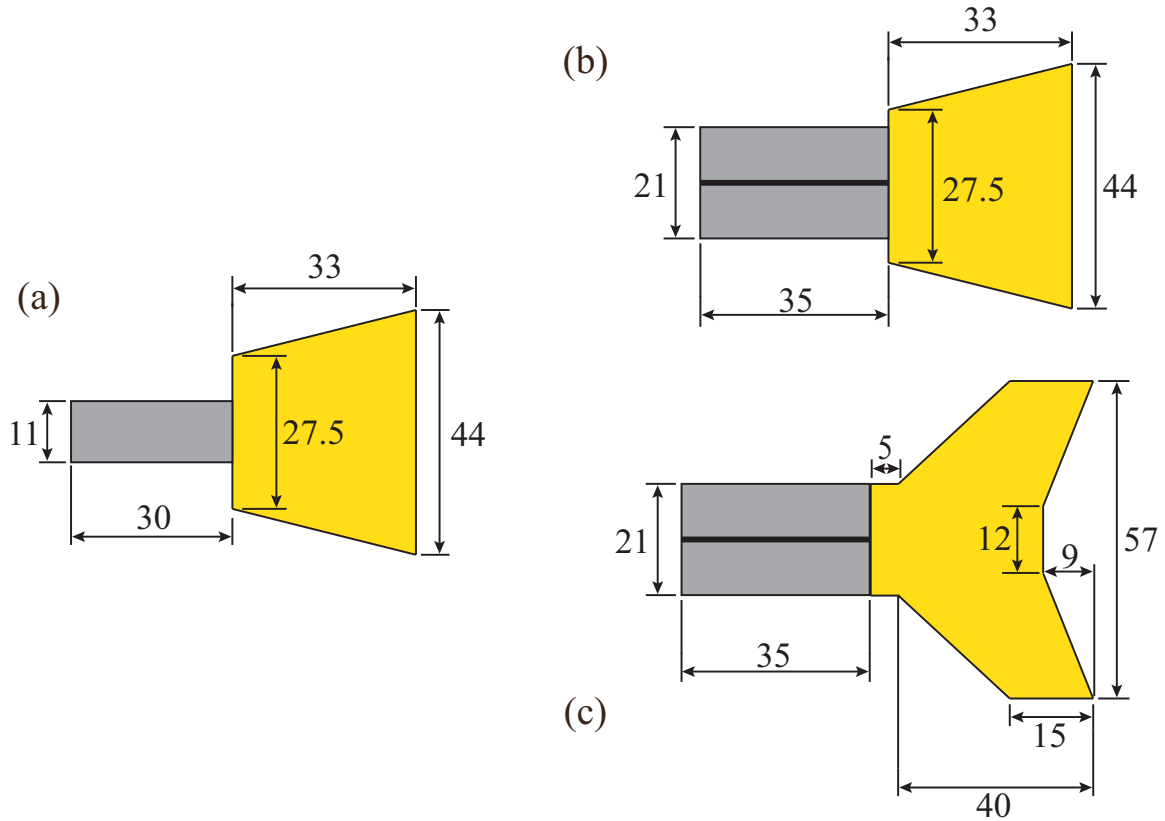


Figure 4.13: IPMC-caudal fin assemblies used for thrust testing (units in mm): (a) conventional IPMC sample and simple trapezoidal caudal fin, (b) sectorized IPMC with simple caudal fin, and (c) with bio-inspired caudal fin.

10 mm \times 35 mm electrode pads. A passive caudal fin is attached and used to aid in thrust production as preliminary testing indicated that thrust generated by the IPMC itself is 1- to 2-orders of magnitude smaller than when coupled with a rigid fin. Lexan plastic 50- μ m thick is chosen as the fin material for its high stiffness to weight ratio. Two fin geometries are tested: a simple trapezoidal caudal fin and a bio-inspired fin characteristic of thunniform swimmers approximately 11.8% larger, as depicted in Fig. 4.13(b) and (c), respectively.

The sectorized IPMC was actuated over frequencies ranging from 0.1 to 2 Hz for the trapezoidal shape and 0.4 to 2.6 Hz for the bio-inspired geometry. The resulting average thrust values are reported in Fig. 4.14.

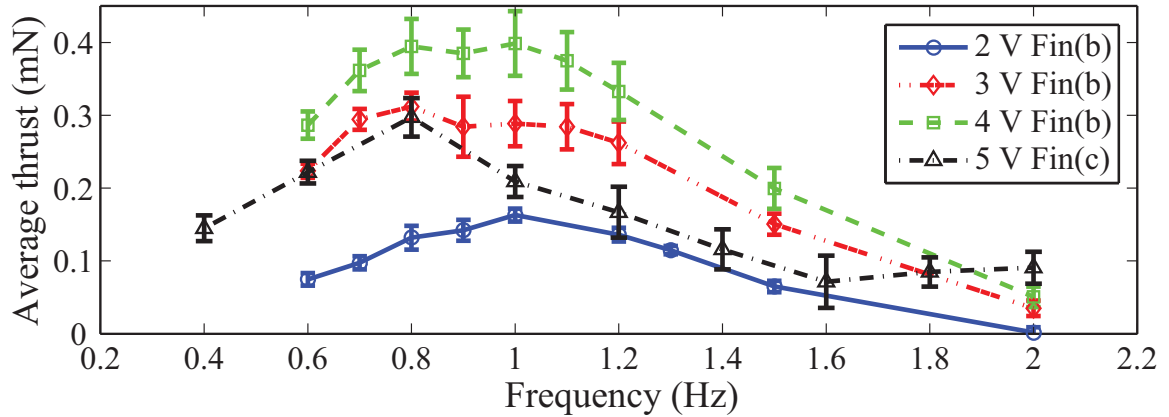


Figure 4.14: Thrust production of sectored IPMC in conjunction with caudal fin shapes shown in Fig. 4.13(b) and Fig. 4.13(c) when actuated by sinusoidal input voltages.

The largest average thrust value is found using the trapezoidal fin with an applied voltage of 4 V at 1 Hz and is 0.4 mN. When the biomimetic caudal fin is used, a maximum thrust is measured at an actuation frequency of 0.8 Hz and is found to be 0.3 mN. This peak value occurs at a lower frequency than in the case of a trapezoidal caudal fin. Interestingly, despite the caudal fin's larger surface area thrust forces are approximately 26% lower at a 25% higher actuation voltage. This can be attributed to hydrodynamic effects relating to the complex geometry; particularly the cutout on the trailing edge and its effect on vortex production. These results show that the thrust production is greatly influenced by the configuration of the IPMC and caudal fin geometry.

Experimental results show that thrust generation is heavily dependant on actuation frequency, applied voltage, input waveforms, and configuration of the IPMC and caudal fin geometry. However, implementation of IPMCs as primary propulsors in autonomous underwater vehicles requires a self contained power supply. This means that proper design of underwater vehicles utilizing this technology would need to strike a balance between power consumption and thrust generation to fully maximize

run time and range.

4.4 Power Consumption and Effectiveness

The power consumption of IPMC actuators is dependant on several factors. The first of which is that the size or geometry of the actuator itself. The mechanism behind IPMC actuation is the migration of mobile cations in response to transient charge behavior on the IPMCs surface. Increasing the size of the actuator results in the more mobile cations and increased charge dynamics, this contributes to increased power consumption. Secondly, when applied potentials become too large an electrolytic process know as electrolysis can occur. The standard potential of the water electrolysis cell at 25°C is 1.23 V at pH 7, but in case of IPMCs it may be higher depending on experimental conditions and material properties. In [85] the electrolysis point for an IPMC was found to be 1.8 V. Past this point the resulting reduction reaction splits water into hydrogen and oxygen and results in higher a current draw than is necessary for IPMC actuation. The resulting energy consumed in this process does not aid in thrust production and results in large inefficiencies. The degree to which electrolysis occurs in the actuation cycle is determined by the magnitude of the applied voltage (e.g., electrolysis happens more readily at 5 V than 3 V) and the shape of the input waveform.

The applied voltage and current were monitored via LabVIEW software for all of the experiments conducted in Section 4.3. The power consumption is determined by calculating instantaneous power consumption over a minimum of eight actuation cycles and then taking the mean over the course of the cycle. The resulting power consumption for the conventional IPMC-caudal fin assembly is shown in Fig. 4.15 and Fig. 4.16. In Fig. 4.15 a nonlinear relationship can be seen between the overall power consumption across a range of frequencies and the applied voltage. This is

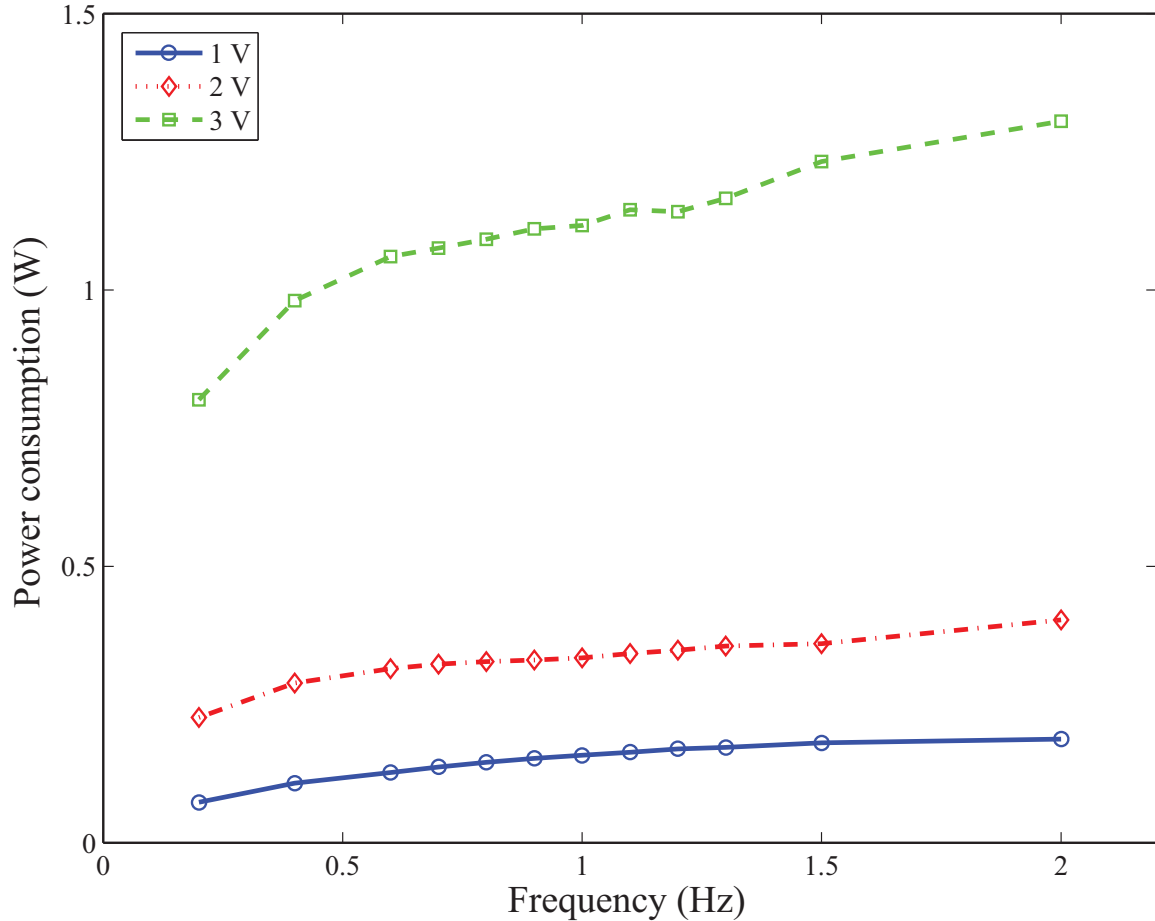


Figure 4.15: Power Consumption of assembly in Fig. 4.13(a) when actuated sinusoidal input voltage.

particularly clear in the jump from 2-V amplitude to 3 V and can be explained by the increased electrolysis. Investigation of different input waveforms (see Fig. 4.16) reveals that square waveforms consume 2-4 times the power of other shapes. Again this is due to electrolysis. The nature of the square wave shapes means the conditions for electrolysis are always present (the applied potential is always 2 V in magnitude). This is confirmed by the fact that the power consumption of the other wave forms decreases in order of how much time the signal spends above the electrolysis point.

In order to quantify how effectiveness of the propulsor, the ratio of thrust force to power consumption defined as Υ is introduced:

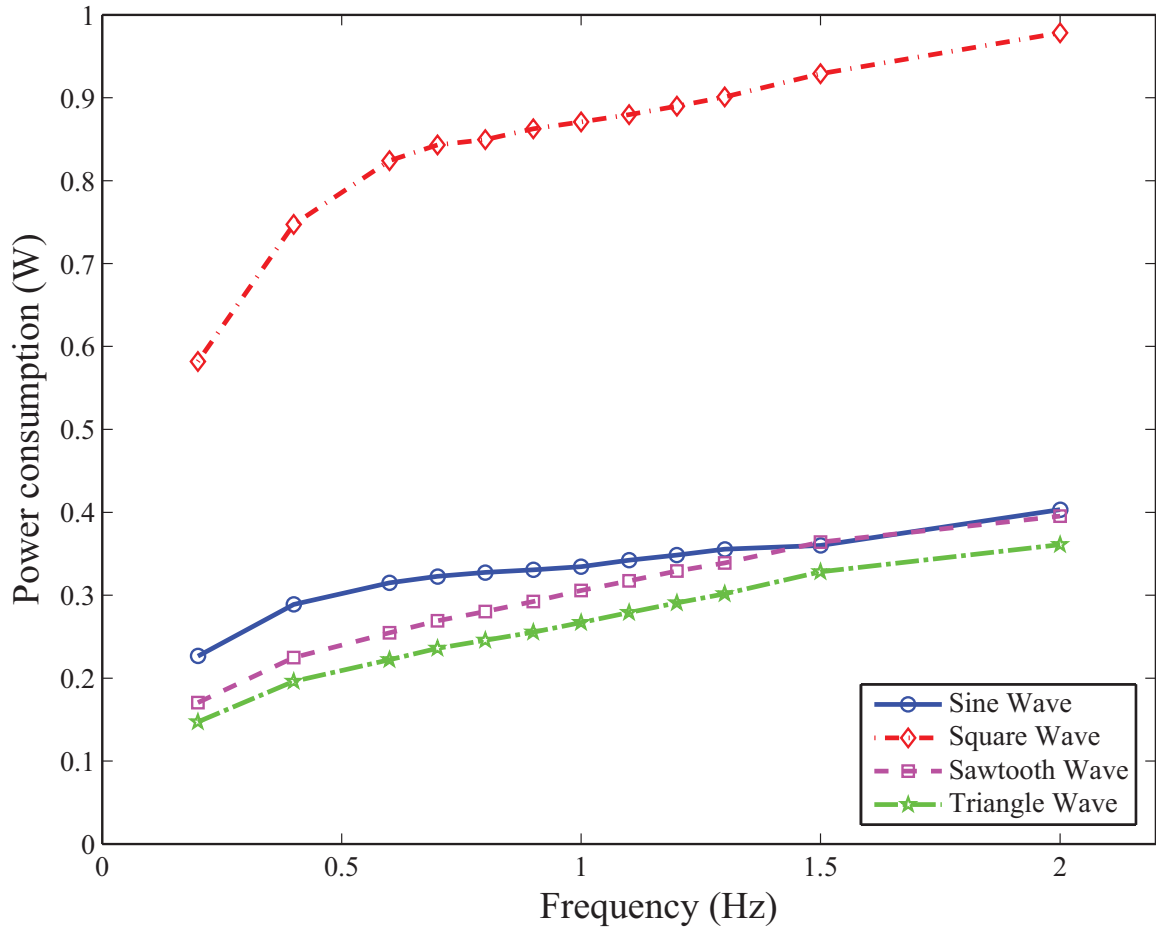


Figure 4.16: Power Consumption of assembly in Fig. 4.13(a) when actuation by different input waveforms of 2 V amplitude.

$$\Upsilon = \frac{T_{ave}}{P}, \quad (4.4)$$

where T_{ave} is the average thrust per actuation cycle, P is the corresponding power consumption, and Υ has the units mN/W . The value of Υ is plotted for all cases in Fig. 4.17. When examining the three amplitudes of the sinusoidal input voltages for the trapezoidal fin, it can be seen that when increasing the voltage to generate more thrust it is a game of diminishing returns. Any increase in thrust gained from an

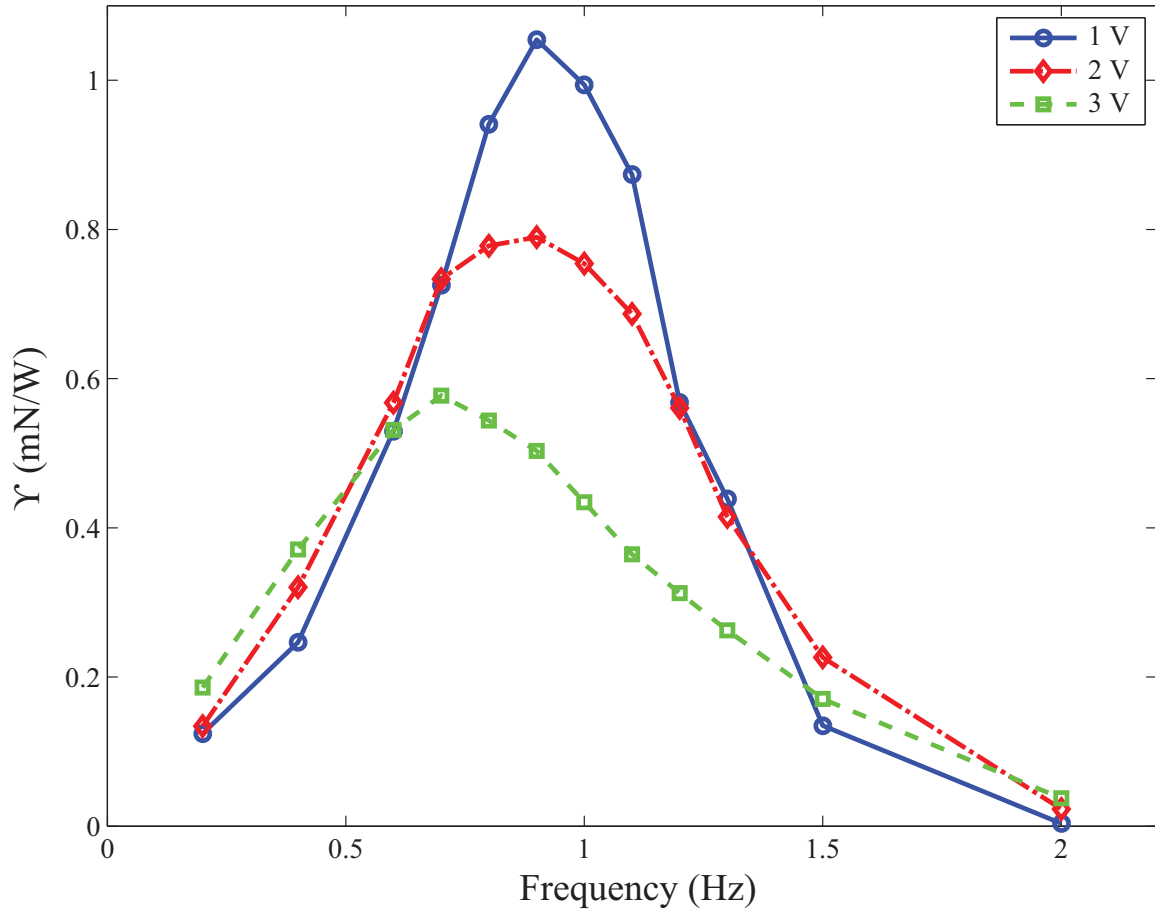


Figure 4.17: The ratio of average thrust force to power consumed, Υ , for the IPMC and tail fin geometry seen in Fig. 4.13(a) when actuated sinusoidal input voltage.

increased input voltage results in a disproportionate increase in power consumption. A similar trend is seen in Fig 4.18 in that while the square wave form produces significantly greater thrust Υ is significantly lower than that of other waveforms. It can also be seen that sine and triangle waveforms exhibit very similar thrust to power consumption relationships. However, when this is compared with data in Fig. 4.12, where the sine wave produces significantly higher thrust than a triangle wave at 2 V a conclusion can be drawn. A sinusoidal waveform for is ideal for providing maximum thrust at a given input voltage without sacrificing power consumption. A maximum value of 1.1 mN/W was seen for Υ .

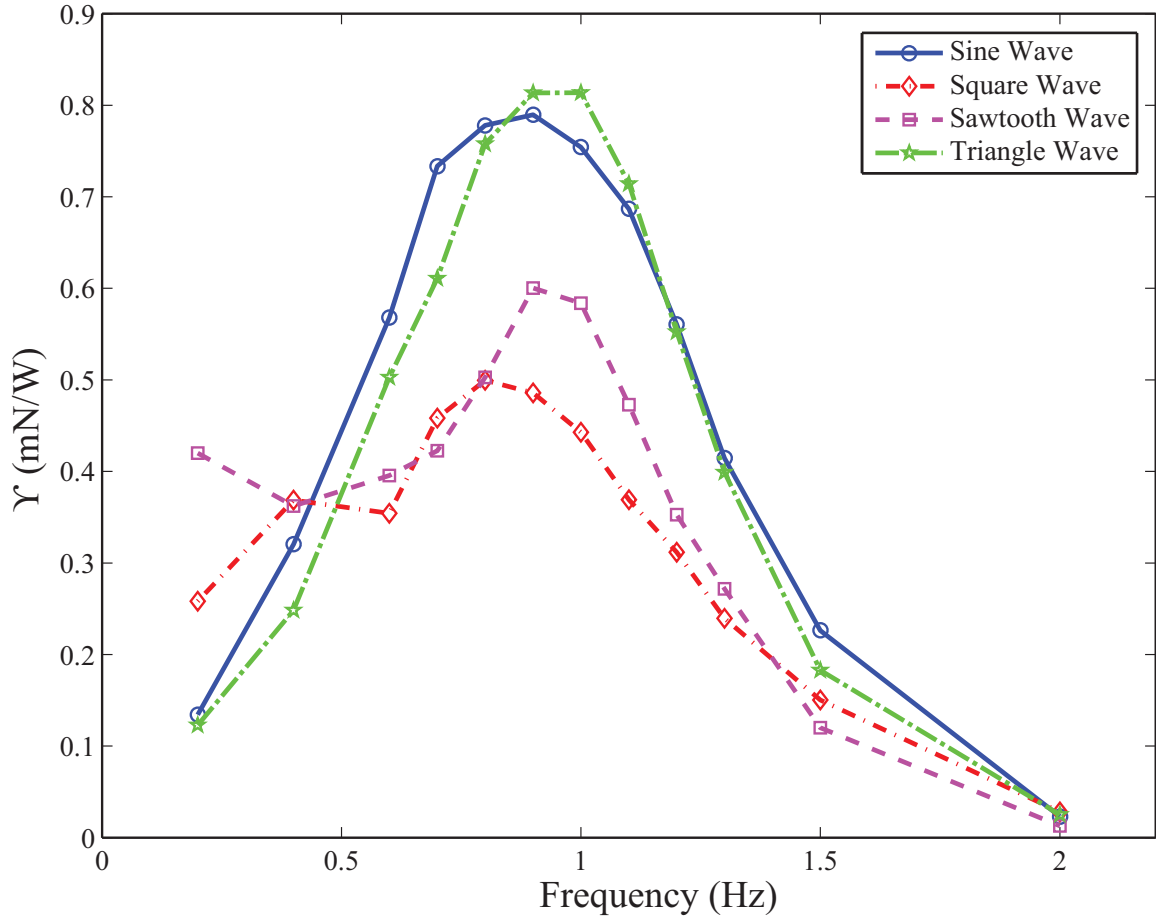


Figure 4.18: The ratio of average thrust force to power consumed, Υ , for the IPMC and tail fin geometry seen in Fig. 4.13(a) when actuated by different input waveforms of 2-V amplitude.

The same data was analyzed and plotted in Fig. 4.19 and Fig. 4.20 for the bi-sector IPMC and caudal fins shown in Fig. 4.13 exhibit similar trends. As the applied voltage increases, the power consumption increases nonlinearly for the trapezoidal caudal fin. However, this trend stops when the bio-inspired caudal fin is examined. This fin consumes less than half the power of the trapezoidal fin despite being actuated at a 25% higher applied voltage. This is investigated further later.

Investigation of Υ of the different fins shapes yields interesting results. In the case of the bio-inspired fin Υ of the fin is on par with the trapezoidal fin at 1 V

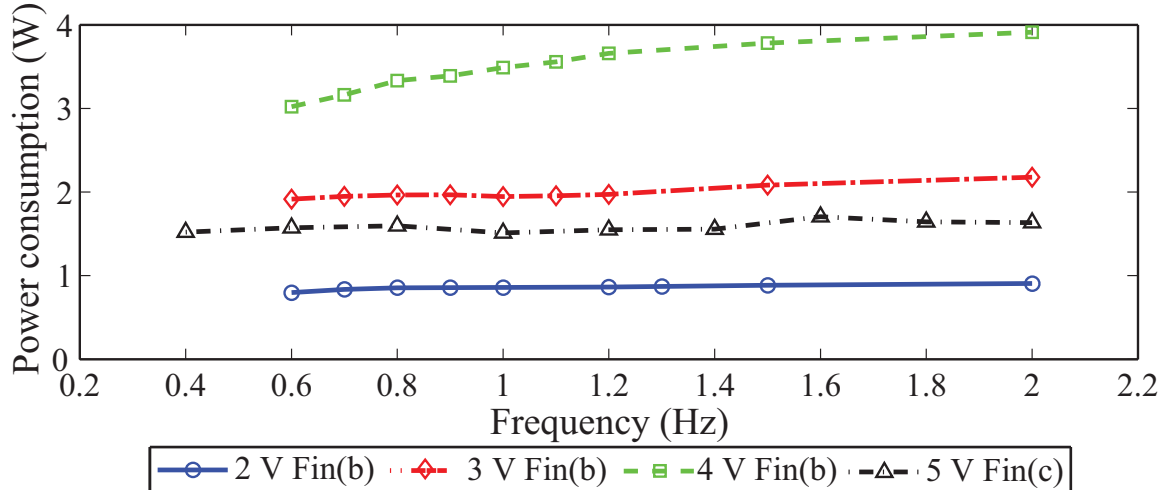


Figure 4.19: Power consumption of sectored IPMC and caudal fins seen in Fig. 4.13(b) and (c) when actuated sinusoidal input voltage.

despite its drastically higher voltage of 5 V. It is suspected that the geometry of the bio-inspired caudal fin minimizes drag perpendicular to the fin and thus reduces energy consumption throughout the cycle. Complex hydrodynamic effects related to vortex generation are also likely explanations. Further experimentation will need to be conducted in order to draw concrete conclusions.

4.5 Summary

This chapter described the characterization of sectored IPMCs for propulsion and maneuvering in underwater systems. It was determined that sectored IPMCs produced reasonable levels of force and torque for underwater systems, and the propulsion characteristics were suited for propelling a small robotic system.

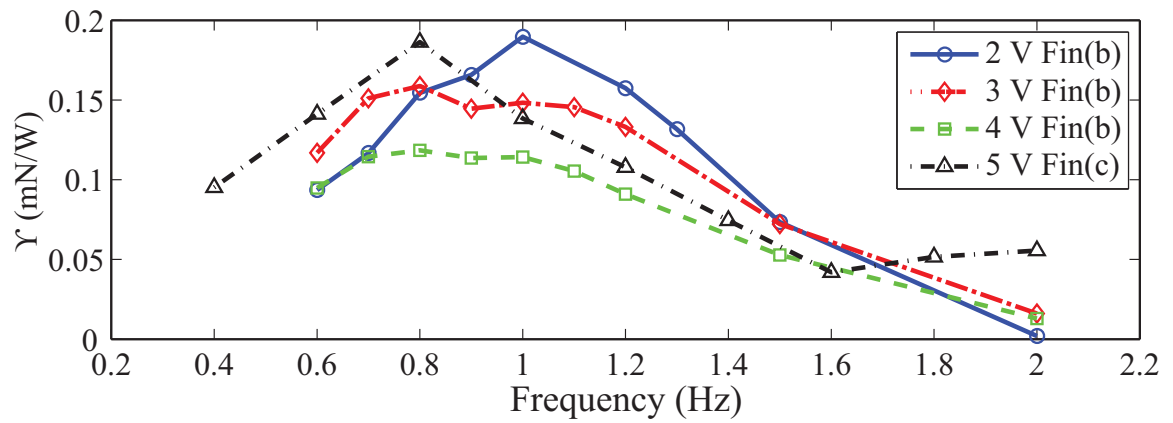


Figure 4.20: The ratio of average thrust force to power consumed, Υ , for sectored IPMC shown in Fig. 4.13(b) and (c) versus frequency of sinusoidal input voltage.

Chapter 5

IPMC-Based Bio-inspired Robot

The characterization results presented in the previous chapter demonstrated feasibility of sectored IPMCs for bio-inspired applications. Additionally, when used in a flapping capacity and paired with a passive element to form a caudal fin, significant thrust is produced. To demonstrate the potential of these sectored IPMCs with respect to underwater robotics a prototype was developed. The device is endowed with IPMC actuators for propulsion and advanced maneuverability through the use of sectored IPMCs that allow potential maneuvering in the roll, pitch, and yaw planes with pectoral fins (anterior rudders). The design and characterization of the resulting prototype are discussed.

5.1 Design

5.1.1 Initial Body Design: Monolithic Silicone Body

To demonstrate the potential of sectored IPMCs for active fins a bio-inspired platform was to be developed. A streamlined body to house wiring, provide structure, and clamp the actuators was needed. Ideally a flexible body was desired that would allow natural undulating movement as a result of tail fin actuation. To achieve this, a monolithic silicone body was first proposed. Using a two part silicone casting rubber (RTV 500, Hastings Plastic) because of its flexibility, durability, and reasonable

density (1400 kg/m^3), a body was design as shown in Fig. 5.1(a). The rubber would also also allow for a smooth streamlined shape through the design of a custom mold.

To allow service and buoyancy negative areas would be molded into the space. Power delivery would be handled by gold plated magnets clamps inside the robot body. Creating the body was a three part processes. Two individual halves were poured and inserts were placed to create space for the the IPMC actuators and positive buoyancy that would be added later. The two halves were then mated and sealed with fresh casting rubber leaving small slits for insertion of actuators later. The custom mold, top, and bottom view of the streamlined body are shown in Fig. 5.1(b), (c), and (d), respectively. After construction of the prototype it was found that the design did not allow sufficient positive buoyancy to be added to make the robot neutrally buoyant. In addition, the thickness of rubber surrounding IPMCs in the pectoral fin and caudal fin area inhibited the deflection of the actuators. Also, the body's construction did not allow for changes to be made primarily because rubber readily teared once any crack or cut was introduced. A more robust design that allowed easier changes was needed.

5.1.2 Final Body Design

Due to the challenges with the initial monolithic silicone rubber body design, the final prototype body was created using acrylic plastic. The body consisted of two separate identical pieces that mated to form a bluff body as shown in Fig. 5.2. A modular design that allowed quick and easy removal of the fins is created using gold plated magnets as the contact and power delivery mechanisms. This design allows quick modification of fin configuration and geometry. Slits were machined into the body to accommodate the gold plated magnetic clips. Silicone coated 36-gauge copper strand wire (Calmont, Siliflex) was used to tether the robot for simplicity and to

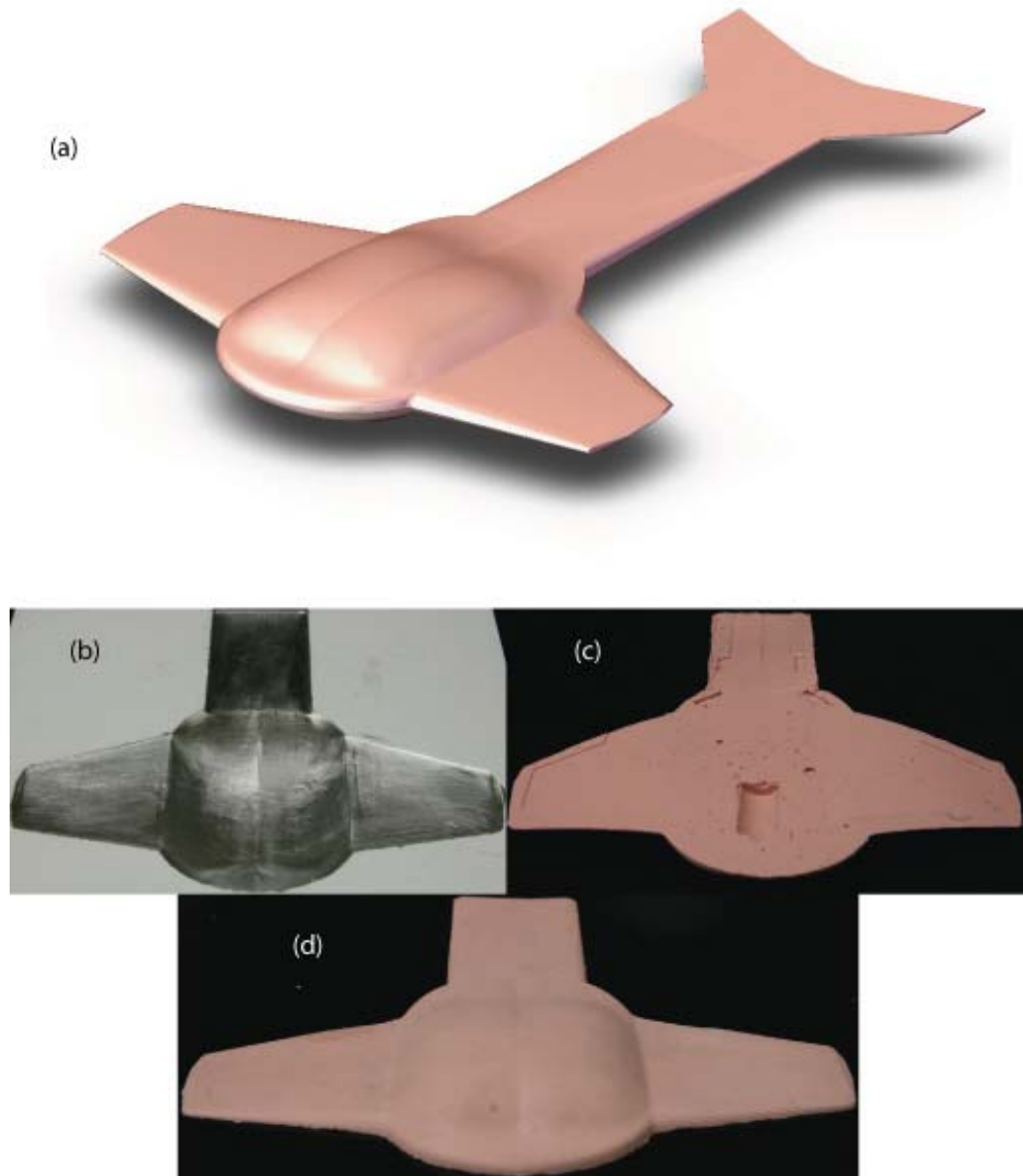


Figure 5.1: Initial design: monolithic body (a) the 3-D model, (b) used to construct the body out of silicone casting rubber and (c) the bottom view and (d) top view of the resulting cast body.

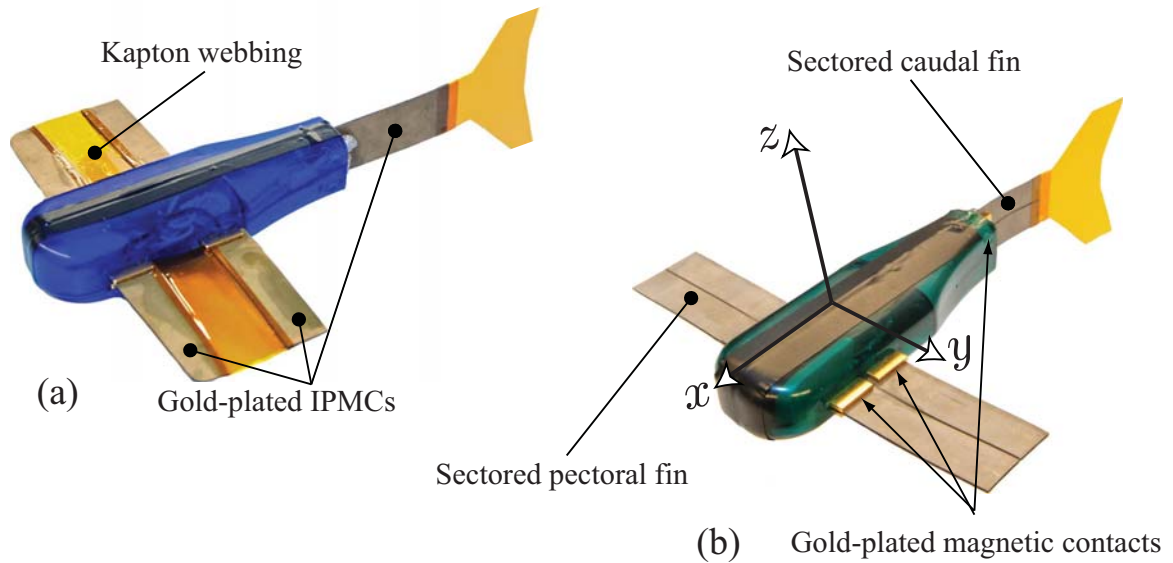


Figure 5.2: Two bio-inspired IPMC-based robots: (a) prototype with gold-plated IPMCs where pectoral fins consisted of individual actuators connected by Kapton[®] film and (b) prototype with three bi-sectored IPMCs.

avoid affecting its dynamic performance in water. The robot was partially filled with silicone casting rubber to the point of near neutral buoyancy and then sealed. This modular design allowed for easy swapping pectoral fin and caudal fin assemblies as well as repair of electrical contacts. If a wireless design was developed later the electronic and power package could fit inside of the body cavity.

To compliment the newly constructed body pectoral fins were needed. IPMCs were revived to the point of functionality with the gold resurrection technique discussed in Section 3.2 and illustrated in Fig. 5.2(a). Pectoral fins were constructed out of four individual IPMCs (two per side) with one actuator at the leading and trailing edge. These two IPMCs were connected by a webbing of Kapton[®]. The purpose of this webbing was to provide a control surface that would reflect the movement of the IPMCs and generate a twisting motion when the IPMCs were not actuated in unison just as is done with a silicone casting rubber “boot” in Appendix A.

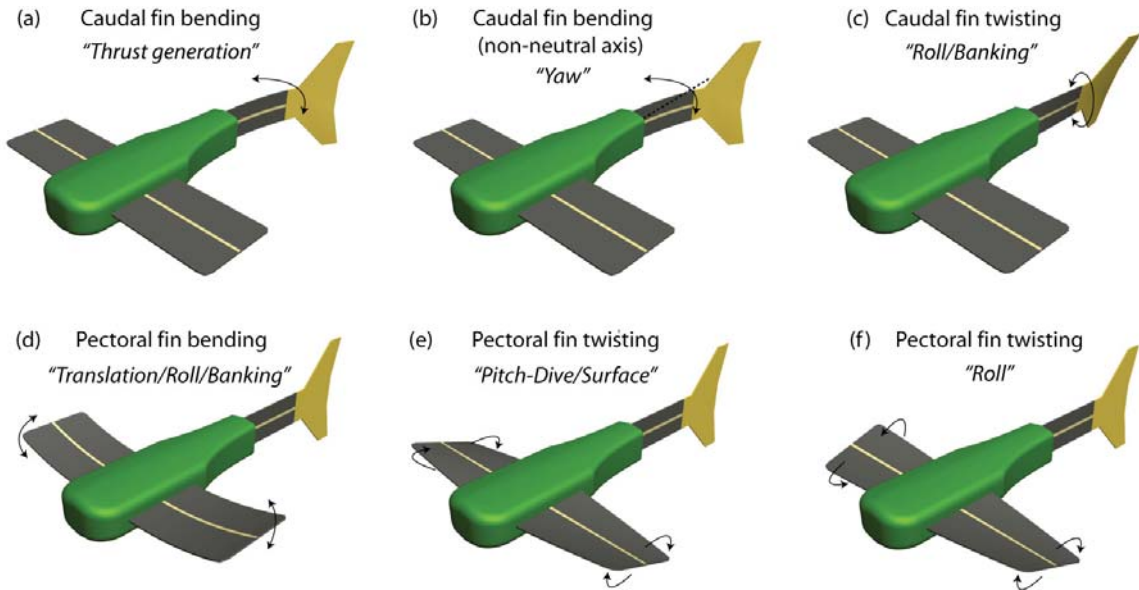


Figure 5.3: Robot motions and required fin orientations.

In the final prototype monolithic IPMCs featuring a bi-sectored pattern are used as right and left pectoral fins and as a tail assembly featuring a passive caudal fin. The design of the robot can be seen in Fig. 5.2(b). The same IPMC-caudal fin assembly as shown in Fig. 4.13(c) was used. Up to this point bio-robotic fish have used the caudal fin both for propulsion and maneuverability by way of changing the duty cycle or biasing the input voltage so that the caudal fin does not oscillate about a neutral axis [31, 32]. This allows the robot motion in the yaw plane. By utilizing sectored IPMCs as pectoral fins, more degrees of freedom can be achieved and thus, more complex maneuvering. For example, by propelling the robot forward and then twisting the pectoral fins in opposite directions, the robot body can roll. Then twisting the pectoral fins in the same direction would result in a banking motion of the entire robot. Components of this process and other motions are depicted in Fig. 5.3.

When the final prototype was submerged in water approximately 25% of the caudal fin is above the water surface. The finished prototype had a mass of 67.4 g and was

177-mm long and is seen in Fig. 5.2(b).

5.1.3 Body Dynamics

A model for the body dynamics of an underwater vehicle is proposed in [73]. The model was experimentally validated and shown to correlate to a high degree. This model is adapted and used to defined the dynamics of the prototype when performing ostraciiform locomotion swimming.

The prototype is modeled relative to a Newtonian reference frame defined by a set of cartesian coordinates, X, Y, Z (see Fig. 5.4). Additionally, a fixed cartesian coordinate system centered about the body's center of buoyancy is illustrated and defined by x, y, z . Several assumption are made in forming the model:

1. The prototype center of mass and center of buoyancy are coincident;
2. The entire device displaces its own weight in water, i.e., it is neutrally buoyant;
3. Only in-plane (x/y -plane) motion, yaw w (rotation about the Z -axis), surge v (forward motion in x -direction), and sway u (transverse to body in y -direction), are relevant to vehicle behavior;
4. Yaw, sway, and surge motions do not exhibit inertial coupling (i.e., the movements are de-coupled);
5. The angle θ is the required input and defines the neutral axis of IPMC actuation; and
6. The robot's body, for hydrodynamic purposes, can be reasonable approximated by a prolate spheroid.

The position of the prototype in the inertial reference frame is illustrated in Fig. 5.4. The external forces acting on the body are also depicted. The velocity

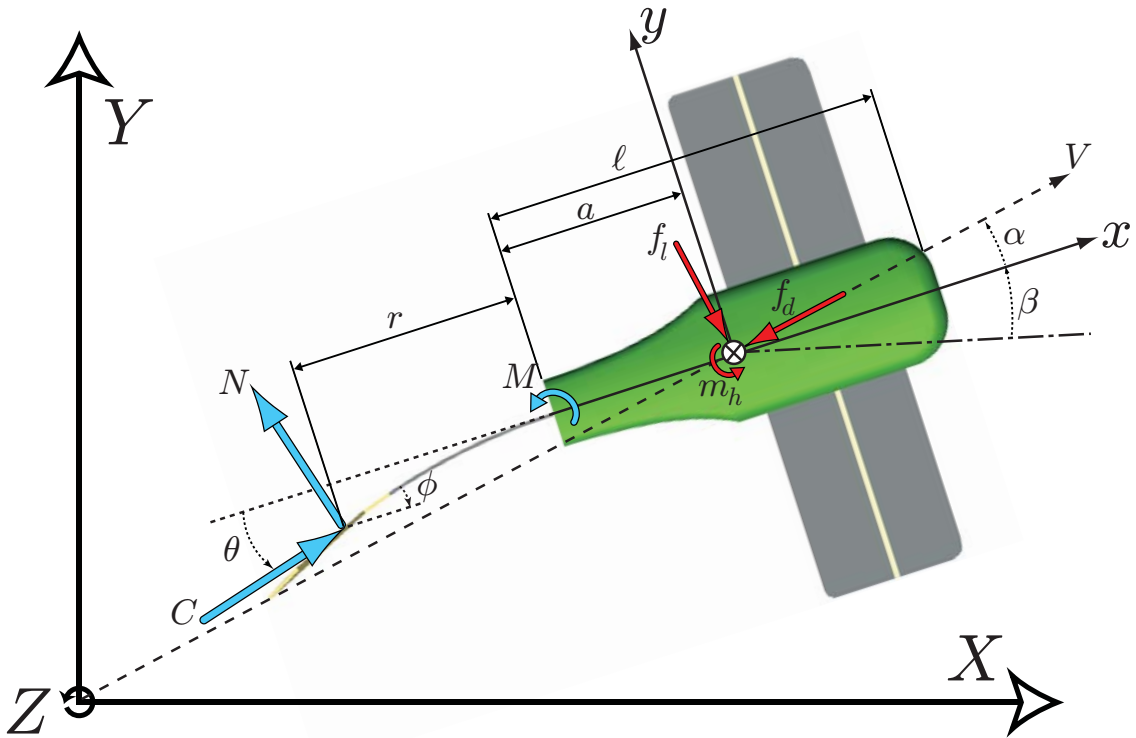


Figure 5.4: The 2-D representation of the body dynamics of the prototype during ostraciiform locomotion.

vector is denoted by V , where the magnitude of the vector is $|V| = \sqrt{v^2 + u^2}$. In the figure, four angles, θ , α , β and ϕ , are defined. The angle θ represents the oscillation angle of the caudal fin with respect to the body coordinate x . The attack angle, α , is the angle formed by the velocity vector V and x -axis. Lastly, the angle β is the prototypes attitude relative to the frame of reference; this represents the yaw angle of the robot and when $\beta = 0$ the X and x axis are parallel. The forth angle ϕ is the attack angle of the tail fin fin and is addressed later in Section 5.1.4.

The Eulerian description of the swimming robot's planar motion is expressed by

the following system equations [33, 73]:

$$\dot{v} = \frac{F_x + (m_b + Y_{\dot{u}})uw}{m_b + X_{\dot{v}}}, \quad (5.1a)$$

$$\dot{u} = \frac{F_y - (m_b + X_{\dot{v}})vw}{m_b + Y_{\dot{u}}}, \quad (5.1b)$$

$$\dot{w} = \frac{(-Y_{\dot{u}} + X_{\dot{v}}) + M_z}{(J_z + K_{\dot{w}})}, \quad (5.1c)$$

where \dot{v} , \dot{u} , and \dot{w} represent the time derivatives of the corresponding variables. The mass of the vehicle and its moment of inertia about the z -axis is denoted by m_b and J_z , respectively. The hydrodynamic variables $Y_{\dot{u}}$, $X_{\dot{v}}$, and $K_{\dot{w}}$ are defined in [86] to account for the added mass on the robot due to hydrodynamic effects.

The system of equations (5.1) feature the force variables F_x , F_y , and moment M_z . These represent the sum of the external forces acting on the body in the x and y directions and the moments about the z -axis. These forces represent those generated in reaction to the IPMC actuators movement as well as forces due to hydrodynamic dampening and are given by:

$$F_x = C \cos(\theta) - N \sin(\theta) - f_d \cos(\alpha) - f_l \sin(\alpha), \quad (5.2a)$$

$$F_y = C \sin(\theta) - N \cos(\theta) - f_d \sin(\alpha) - f_l \cos(\alpha), \quad (5.2b)$$

$$M_z = -Ca \sin(\theta) - Na \cos(\theta) + M + m_h, \quad (5.2c)$$

where a is the distance from the magnetic clamping point to the center of buoyancy and the reactive forces from IPMC oscillation are C , N , and moment M . The chord force C and normal force N are described in Section 5.1.4. The variables m_h , f_d , and f_l describe the moment resulting from hydrodynamic dampening as described in [87],

the form drag of the robot, and the lift, respectively,

$$m_h = \frac{1}{2}\rho|V|^2 A_c \ell \left(\frac{\ell}{|V|} C_{Mw} w + C_{M\alpha} \alpha \right), \quad (5.3a)$$

$$f_d = \frac{1}{2}\rho|V|^2 A_c C_d, \quad (5.3b)$$

$$f_l = \frac{1}{2}\rho|V|^2 A_c C_l \alpha, \quad (5.3c)$$

where ρ is the mass density of the water and A_c is the cross-sectional reference area of the prototype. The coefficients C_d , C_l , $C_{M\alpha}$, and C_{Mw} are dimensionless and are function of the Reynolds number, $Re = \frac{\rho\ell|V|}{\mu}$, and the angle of attack α . These coefficients, which are largely geometry-dependant, also contain unknown functions that represent modeling uncertainties relating to viscous drag and lift.

5.1.4 Flapping IPMC

In [88] a model was developed that illustrated the hydrodynamics of an oscillating rigid fin. The model was found to match experimentally measured forces quite well. The model is adapted here and meshed with the model expressed in the previous section. The IPMC actuator and Lexan caudal fin are assumed to be sufficiently stiff to minimize cambering and as such can be represented by an oscillating plate. A free body diagram of the oscillating tail is shown in Fig. 5.5. The movement of the fin can then be described as:

$$\theta = \theta_{max} \sin(\omega t), \quad (5.4)$$

where ω is the angular frequency of oscillations in radians. A velocity vector, u_f , of the caudal fin can then be defined who magnitude is then given by:

$$U_f = \sqrt{r^2 \dot{\theta}^2 + V^2}, \quad (5.5)$$

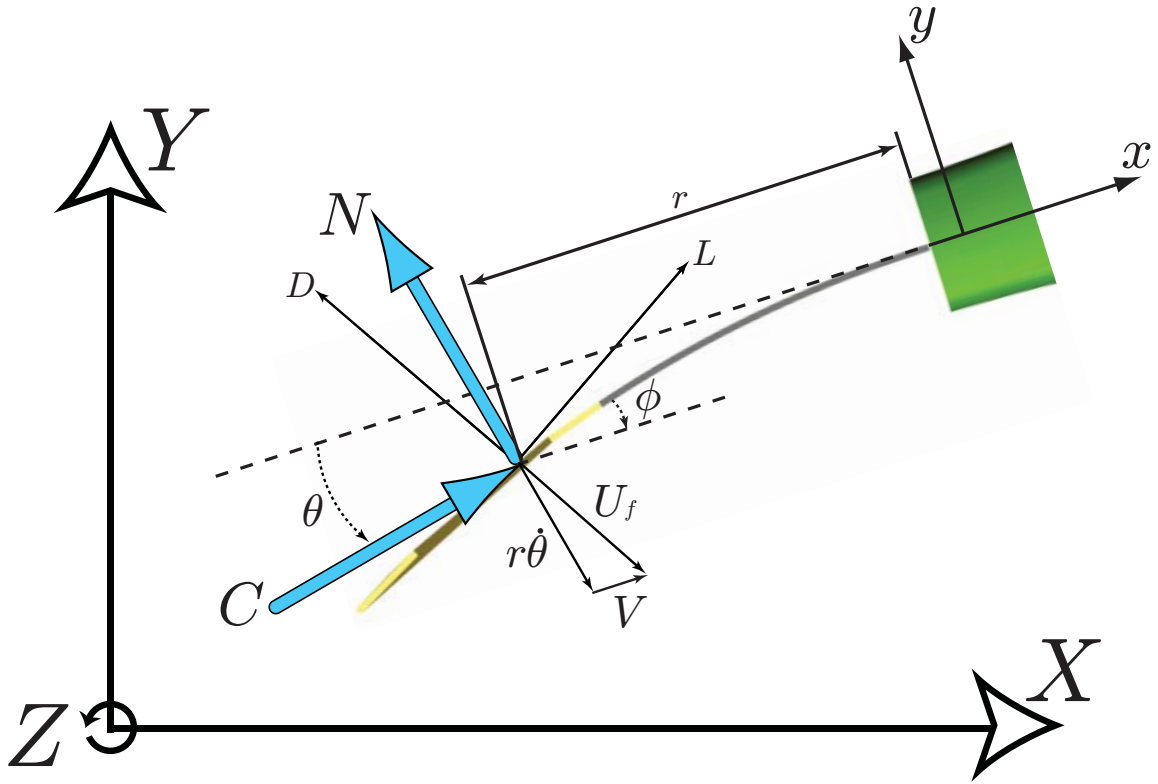


Figure 5.5: Free body diagram of forces acting on oscillating tail, where D and L represent drag and lift forces, respectively.

where r is the distance from the mounting point of the IPMC to the acting center of force on the caudal fin and V is the velocity of the prototype as defined in Section 5.1.3.

The angle of attack and its time derivative can then be expressed as:

$$\phi = \arctan \left(\frac{r\dot{\theta} \cos \theta}{r\dot{\theta} \sin \theta + V} \right), \quad (5.6a)$$

$$\dot{\phi} = \frac{Vr(\ddot{\theta} \cos \theta - \dot{\theta}^2 \sin \theta) - r^2\dot{\theta}^3}{2Vr\dot{\theta} \sin \theta + (r\dot{\theta})^2 + V^2}. \quad (5.6b)$$

The forces acting on the oscillating fin again are the result of drag, lift, and added mass effects. The forces are expressed in the body's Cartesian coordinate system, x , y , and z , that was defined earlier and are centered about the center of buoyancy of

μ_c	0
μ_n	$\rho\pi a^2$
μ_{nc}	0
μ_{cw}	0
μ_{nw}	$\rho\pi a^3$
μ_w	$\frac{9}{8}\rho\pi a^4$

Table 5.1: Added mass coefficients of a 2-D thin plate as defined in [6].

the robot. The chord force C (the force axial to the fin), and normal force N that were first presented in Eq. (5.2) now become

$$N = N_d + N_l + N_{am}, \quad (5.7a)$$

$$C = C_d + C_l + C_{am}, \quad (5.7b)$$

where the subscripts d , l , and am denote components of the drag, lift, and added mass effect forces normal and axial to the fin.

The dimensionless coefficients C_d^f and C_l^f represent the drag and lift coefficients of the oscillating fin are dependant on the operating Reynolds number and the fin geometry. These coefficients are featured in the following equations expressing the lift and drag force components. The components N_d , C_d , N_l , and C_l can then be written as:

$$N_d = -C_d^f \rho A_f U_f^2 \sin(\phi + \theta), C_d = -C_d^f \rho A_f U_f^2 \cos(\phi + \theta), \quad (5.8a)$$

$$N_l = -C_l^f \sin \phi \rho A_f U_f^2 \cos(\phi + \theta), \quad (5.8b)$$

$$C_l = -C_l^f \sin \phi \rho A_f U_f^2 \sin(\phi + \theta), \quad (5.8c)$$

with A_f being the projected fin area normal to U_f .

Lastly, the added mass effects are assessed. The added mass coefficients for a two dimensional thin plate were derived in [6] and are shown in Table 5.1. The force

components are then

$$N_{am} = -\mu_{nc}\dot{U}_c - \mu_n\dot{U}_n - \mu_{nc}\ddot{\theta} - \dot{\theta}(\mu_c U_c + \mu_{nc} U_n + \mu_{cw}\dot{\theta}), \quad (5.9a)$$

$$C_{am} = -\mu_c\dot{U}_c - \mu_{nc}\dot{U}_n - \mu_{cw}\ddot{\theta} + \dot{\theta}(\mu_{nc} U_c + \mu_n U_n + \mu_{nw}\dot{\theta}), \quad (5.9b)$$

where U_c , U_n are the components of U_f normal and axial to the fin. Their time derivatives \dot{U}_c , and \dot{U}_n are given by

$$\dot{U}_c = -\frac{1}{U_f} r^2 \dot{\theta} \ddot{\theta} \sin(\phi + \theta) - U_f (\dot{\phi} + \dot{\theta}) \cos(\phi + \theta), \quad (5.10a)$$

$$\dot{U}_n = \frac{1}{U_f} r^2 \dot{\theta} \ddot{\theta} \cos(\phi + \theta) - U_f (\dot{\phi} + \dot{\theta}) \sin(\phi + \theta). \quad (5.10b)$$

5.2 Performance Characterization and Analysis

The prototype's caudal fin was actuated over a range of frequencies with a 5-V amplitude sine wave. The robot's motion was recorded from two angles with a 1 cm grid in the background. Three runs at each frequency were conducted. The video was then analyzed to obtain an average velocity resulting in six measurements for each frequency. The average velocity of the robot as a function of the actuation frequency can be seen in Fig. 5.7. The highest average velocity (2.8 cm/s) was found at an actuation frequency of 2 Hz. Significant improvements can be made through full submersion of the caudal fin as well as optimization of the IPMC-caudal fin geometry. Intuitively one would expect the frequency of maximum velocity of the robot and the maximum thrust (presented in Fig. 4.14) to agree. It was found that this is not the case and is explained by the the fact that at low actuation frequencies the large tail actuation amplitude results large yaw angle of the robot body. This results in a limiting effect on forward speed. At frequencies >1 Hz this effect is reduced and reaches an optimum level at 2 Hz, where the maximum velocity occurs. A similar

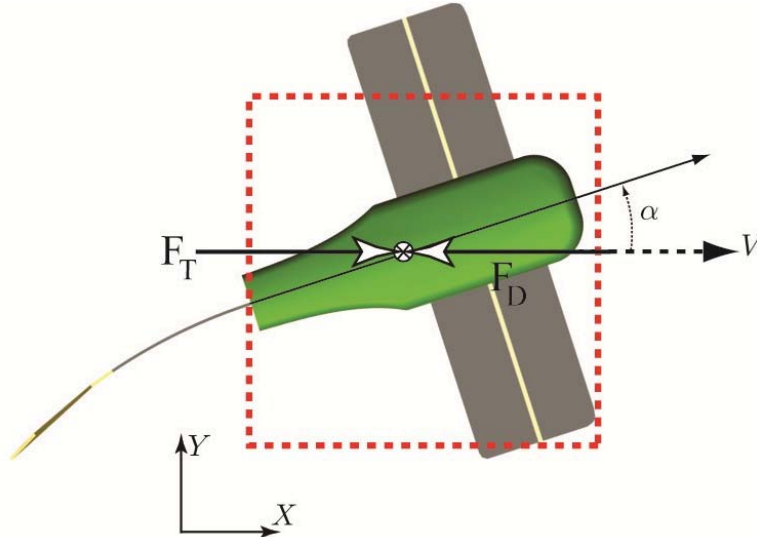


Figure 5.6: Simplistic model proposed to predict the prototype's velocity.

conclusion is made for an IPMC enabled robot in [31].

The model described in Section 5.1.3 describes the dynamic characteristics of the robot moving through a fluid. However, solving the equations is difficult, and is only an approximation. To correlate the experimental thrust data with the velocity of the prototype a simplistic model was proposed (see Fig. 5.6) to take the place of complete model previously described. In operation, the velocity of the robot increases to the point at which the thrust is canceled out by the drag force,

$$0 = F_T(f) - F_D(f), \quad (5.11)$$

As the velocity of the robot oscillates from its lowest point to the maximum surge speed the drag force oscillates as well. To simplify the problem the transient movement of the robot is ignored and it is assumed that the average speed of the robot can be derived from a free body diagram consisting of the average thrust force generated by the caudal fin and the drag force that the robot encounters. Then, at a given frequency, F_T is the thrust force and F_D is the form drag of the entire prototype

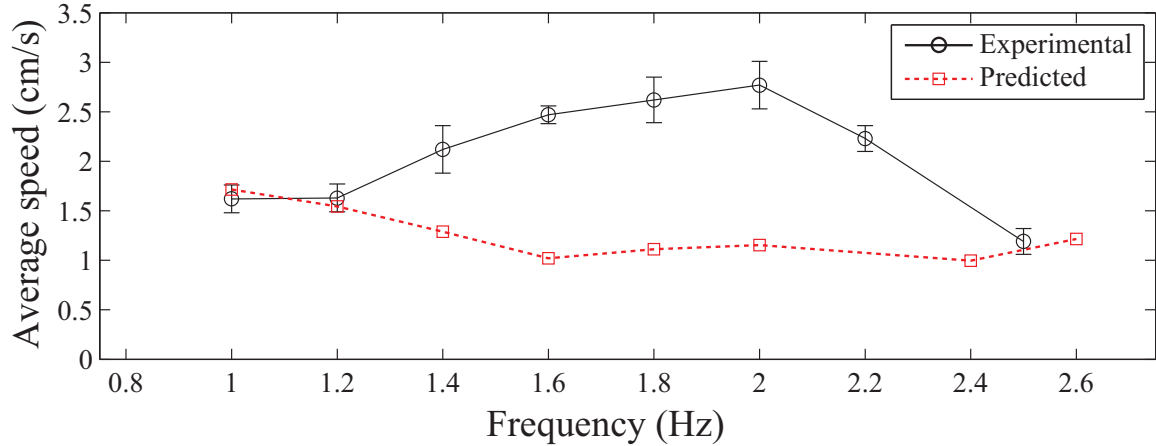


Figure 5.7: Experimentally and predicted velocities of prototype when actuated by 5 V sinusoidal input.

when the body is at its maximum yaw angle and is given by:

$$F_D(f) = \frac{1}{2}\rho C_D A V_P^2, \quad (5.12)$$

where f is the frequency of tail oscillations, C_D is the drag coefficient, A is the reference area, ρ is the fluid density, and V_P is the predicted velocity.

To determine C_D and A , the prototype was mounted in a drag tank and the drag force was measured for various yaw angles. A curve-fit relating yaw angle and the $C_D A$ product was backed out. Then, utilizing video captured from the top view of the robot, a yaw angle, α , was calculated for each frequency and substituted into the the curve-fit derived from drag tank testing to obtain a $C_D A$ product for that frequency. This data, along with the measured thrust at corresponding frequency, can then be used to calculate a predicted velocity:

$$V_p = \sqrt{\frac{2F_T(f)}{\rho C_D A(f)}}, \quad (5.13)$$

The results are shown in Fig. 5.7. It can be seen that the simplistic model predicts

velocities that do not agree with the measured results in magnitude or trend. There are several explanations for the discrepancies between measured and predicted velocities. In reality the robot experiences oscillations about its center of buoyancy in the yaw plane and sway motion (perpendicular to the velocity vector V). These motions generate forces, i.e., added mass effects and hydrodynamic lift, that are represented in Section 5.1.3. Also the thrust has a sinusoidal profile that occurs at twice the actuation frequency. Forces perpendicular to the fin generate moments that further complicate the flow around the robot. The failure of this simplistic model to correlate with the experiment results indicates that the forces mentioned play a large roll in the swimming dynamics of the robotic system. Without taking these forces into account a reasonable prediction of the robots behavior can not be obtained.

When investigating the locomotive behavior in a fluid environment, non-dimensional numbers are typically used. One, the Reynolds number (Re), illustrates the ratio of inertial forces to viscous forces. When $Re \ll 1$ viscous forces are dominate and govern the object's behavior. In contrast, when $Re \gg 1$ viscous forces play little role and inertial forces dominate the object's movement. This means that for small robotic systems or larger ones at low speeds (e.g., accelerating from rest) viscous forces are an important consideration. The Reynolds number of the prototype operating at maximum velocity is approximately 4890.

Another dimensionless number, the Strouhal number (St), corresponds to the ratio of unsteady forces to steady forces in the wake left by the object in transit. The Strouhal number is given by:

$$St = \frac{fA}{V} \quad (5.14)$$

where A is the tail beat amplitude. The Strouhal number is also indicative of the frequency at which reverse Kármán vortices are generated. The Kármán vortices are the primary mechanism responsible for thrust production of an oscillating fin.

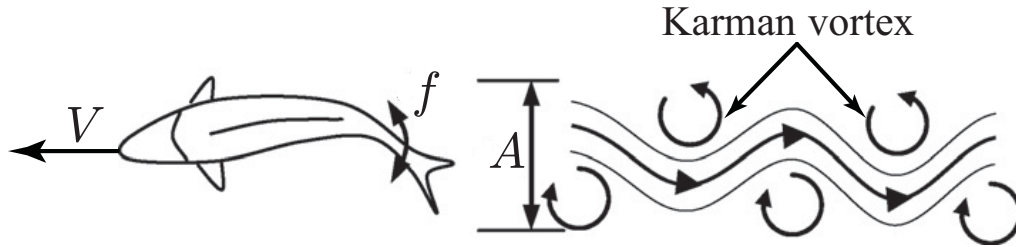


Figure 5.8: An illustration of the reverse Kármán vortex street generated by a swimming fish.

The vortices are created by alternating low pressure vortices downstream from the fin and is illustrated in Fig. 5.8. This Strouhal number is a passive indicator of the effectiveness of thrust production and swimming. When this value is between 0.25 and 0.4, [89] the thrust and swimming behavior of the object is considered ideal. Indirectly it was shown that fish propulsion occurs where $0.25 < St < 0.35$ [90]. The Strouhal number of the robotic prototype at maximum velocity was found to be 0.72. This value being outside the optimal range can be attributed to the caudal fin being of arbitrary design and its geometry and size not being tuned to the length and width of the IPMC actuator. Further improvements could also be made through changes in the body size and geometry.

Chapter 6

Conclusions

Ionic polymer-metal composite actuators have the capability to generate complex motions for applications in underwater systems. Successful integration these actuators into underwater robotic designs is hindered by limited knowledge of their capabilities. Herein, the ability of sectored IPMCs to realize bending and twisting motion was experimentally quantified. A maximum twist angle of 8.46 degrees was found when actuated by a 4 V DC voltage. Thrust production of a sectored IPMC with a passive caudal fin element was investigated for two different fin geometries. This ability was discussed with respect to power consumption. The variable Υ was introduced to reflect the ratio of thrust generation to power consumption of a fixed oscillating fin. The fins that were tested fielded maximum thrust of 0.67 mN, and $\Upsilon = 1.1$ mN/W. The results confirmed the potential for IPMCs act as secondary and primary propulsors for efficient swimming. In addition, sectored IPMCs created with a simple surface machining technique were found to possess the necessary performance to provide enhanced maneuvering ability in underwater robotic applications. This information was used to develop two bio-inspired robotic systems capable of ostraciiform locomotion with potential to control pitch, roll, and yaw through complex twisting of the pectoral fins. Two modular prototypes were designed and utilized a novel magnetic-based con-

tact and power delivery mechanism. A proven model was then proposed to express the hydrodynamic behavior of the swimming prototype. The robotic platform was experimentally characterized for swimming speed and produced a maximum speed of 2.8 cm/s. The simplified model was then examined for its ability to predict average thrust of the prototype. It was found that a successful prediction requires inclusion of all transient behavior and hydrodynamic effects. The approaches used here were largely experimental and serve to compliment the documented results from other groups and further the understanding of IPMCs, specifically patterns actuators and their biomimetic application potential. The resulting data provided in this thesis is a comprehensive reference of IPMC dynamic characteristics which can serve as a foundation for the design of future IPMC enabled underwater robotic vehicles.

Chapter 7

Future Work

Future innovations toward performance improvement of IPMCs in the areas of blocking force and stiffness, specifically lowering stiffness, while increasing the blocking force, will improve the attractiveness of incorporating sectored IPMCs into underwater robotic vehicles. These advances will also open up opportunities to generate more complex bio-mimetic motions such as undulations without needing independent flexible mediums. However, utilizing simple surface machining techniques to produce patterned IPMCs capable of complex deformation is a reality, and the potential to use these surfaces to actively control underwater robotic systems capable of multiple degrees of freedom is possible.

Bibliography

- [1] M. Krieg and K. Mohseni, “Thrust characterization of a bioinspired vortex ring thruster for locomotion of underwater robots,” IEEE Journal of Oceanic Engineering, vol. 33, no. 2, pp. 123–132, 2008.
- [2] C. Lindsey, Form, Function, and Locomotory Habits in Fish, ser. Fish Physiology, 1979, vol. Volume 7.
- [3] M. Sfakiotakis, D. M. Lane, and J. B. Davies, “Review of fish swimming modes for aquatic locomotion,” IEEE Journal of Oceanic Engineering, vol. 24, no. 2, pp. 237–252, 1999.
- [4] D. R. Yoerger, J. G. Cooke, and J. J. Slotine, “The influence of thruster dynamics on underwater vehicle behavior and their incorporation into control system design,” IEEE Journal Oceanic Engineering, vol. 15, no. 3, pp. 167–178, 1990.
- [5] K. H. Low, “Modelling and parametric study of modular undulating fin rays for fish robots,” Mechanism and Machine Theory, vol. 44, no. 3, pp. 615–632, 2009.
- [6] L. Sedov, Two-Dimensional Problems in Hydrodynamics and Aerodynamics. Interscience Publishers, 1965.
- [7] M. Shahinpoor, “Ionic polymer-metal composites (ipmcs) as biomimetic sensors, actuators and artificial muscles - a review,” Smart Materials and Structures, vol. 7, no. 6, p. R15, 1998.
- [8] K. J. Kim and M. Shahinpoor, “Ionic polymer-metal composites: II. manufacturing techniques,” Smart Mater. Struct., vol. 12, no. 1, pp. 65 – 79, 2003.
- [9] M. Shahinpoor and K. J. Kim, “Ionic polymer-metal composites: IV. industrial and medical applications,” Smart Materials and Structures, vol. 14, pp. 197–214, 2005.
- [10] D. Pugal, K. Jung, A. Aabloo, and K. J. Kim, “Ionic polymermetal composite mechanoelectrical transduction: review and perspectives,” Polymer International, vol. 59, no. 3, pp. 279 – 289, 2010.

- [11] K. J. Kim, W. Yim, J. W. Paquette, and D. Kim, "Ionic polymer-metal composites for underwater operation," Journal of Intelligent Material Systems and Structures, vol. 18, no. 2, pp. 123 – 131, 2007.
- [12] N. Kamamichi, M. Yamakita, K. Asaka, and Z.-W. Luo, "A snake-like swimming robot using IPMC actuator/sensor," in IEEE International Conference on Robotics and Automation, Orlando, FL, 2006, pp. 1812 – 1817.
- [13] S. Guo, G. Yarning, L. Lingfei, and L. Sheng, "Underwater swimming micro robot using IPMC actuator," in IEEE International Conference on Mechatronics and Automation, 2006, pp. 249–254.
- [14] H. Nakadoi and D. Sobey, "Liquid environment-adaptive ipmc fish-like robot using extremum seeking feedback," in IEEE/RSJ International Conference on Intelligent Robots and Systems, 2008, pp. 3089–3094.
- [15] G. Alici, G. M. Spinks, J. D. Madden, Y. Wu, and G. G. Wallace, "Response characterization of electroactive polymers as mechanical sensors," IEEE/ASME Trans. Mechatronics, vol. 13, no. 2, pp. 187 – 196, 2008.
- [16] Y. Nakabo, T. Mukai, and K. Asaka, "Kinematic modeling and visual sensing of multi-DOF robot manipulator with patterned artificial muscle," in Proceedings of the 2005 IEEE International Conference on Robotics and Automation (ICRA), Barcelona, Spain, 2005, pp. 4315 – 4320.
- [17] J. H. Jeon, S.-W. Yeom, and I.-K. Oh, "Fabrication and actuation of ionic polymer metal composites patterned by combining electroplating with electroless plating," Composites: Part A, vol. 39, no. 4, pp. 588 – 596, 2008.
- [18] R. O. Riddle, Y. Jung, S.-M. Kim, S. Song, B. Stolpman, K. J. Kim, and K. K. Leang, "Sectorized-electrode IPMC actuator for bending and twisting motion," in SPIE Smart Structures and Materials and Nondestructive Evaluation and Health Monitoring, vol. 7642, San Diego, CA, USA, 2010, p. 764221.
- [19] S. Guo, L. Shi, X. Ye, and L. Li, "A new jellyfish type of underwater microrobot," in Proc. IEEE International Conference on Mechatronics and Automation, Harbin, China, 2007, pp. 509 – 514.
- [20] S. W. Yeom and I. K. Oh, "Fabrication and evaluation of biomimetic jellyfish robot using IPMC," Advances in Science and Technology, vol. 58, pp. 171 – 176, 2008.
- [21] Z. Chen and X. Tan, "Monolithic fabrication of ionic polymer-metal composite actuators capable of complex deformation," Sensors and Actuators, A: Physical, vol. 157, no. 2, pp. 246–257, 2010.

- [22] A. Menozzi, H. A. Leinhos, D. N. Beal, and P. R. Bandyopadhyay, "Open-loop control of a multifin biorobotic rigid underwater vehicle," IEEE Journal of Oceanic Engineering, vol. 33, no. 2, pp. 59–68, 2008.
- [23] G. V. Lauder and P. G. Madden, "Fish locomotion: Kinematics and hydrodynamics of flexible foil-like fins," Experiments in Fluids, vol. 43, no. 5, pp. 641–653, 2007.
- [24] M. Krieg and K. Mohseni, "Developing a transient model for squid inspired thrusters, and incorporation into underwater robot control design," in IEEE/RSJ International Conference on Intelligent Robots and Systems, 2008, pp. 3178–3183.
- [25] —, "Thrust characterization of a bioinspired vortex ring thruster for locomotion of underwater robots," IEEE Journal of Oceanic Engineering, vol. 33, no. 2, pp. 123 – 132, 2008.
- [26] A. Healey, S. Rock, S. Cody, D. Miles, and J. Brown, "Toward an improved understanding of thruster dynamics for underwater vehicles," Oceanic Engineering, IEEE Journal of, vol. 20, no. 4, pp. 354–361, 1995.
- [27] P. R. Bandyopadhyay, "Trends in biorobotic autonomous undersea vehicles," IEEE Journal of Oceanic Engineering, vol. 30, no. 1, pp. 109–139, 2005.
- [28] —, "Maneuvering hydrodynamics of fish and small underwater vehicles," Integrative and Comparative Biology, vol. 42, no. 1, pp. 102–117, 2002.
- [29] Z. Wang, G. Hang, and J. Li, "A micro-robot fish with embedded sma wire actuated flexible biomimetic fin," Sensors and Actuators A: Physical, vol. 144, no. 2, pp. 354–360, 2008.
- [30] Z. Z. Wang and Y. Y. Wang, "A micro biomimetic manta ray robot fish actuated by sma," in IEEE International Conference on Robotics and Biomimetics, 2009, pp. 1809–1813, compilation and indexing terms, Copyright 2010 Elsevier Inc. 20101712895083 Flexible pectoral fin Good stability Pulse width Robot fish Shape memory alloy wire SMA wire.
- [31] S. McGovern, G. Alici, V. Truong, and G. Spinks, "Finding NEMO (novel electromaterial muscle oscillator): A polypyrrole powered robotic fish with real-time wireless speed and directional control," Smart Materials and Structures, vol. 18, 2009.
- [32] B. Kim, D.-H. Kim, J. J. Jung, and J.-O. Park, "A biomimetic undulatory tadpole robot using ionic polymer-metal composite actuators," Smart Mater. Struct., vol. 14, pp. 1579 – 1585, 2005.

- [33] M. Aureli, V. Kopman, and M. Porfiri, “Free-locomotion of underwater vehicles actuated by ionic polymer metal composites,” IEEE/ASME Transactions on Mechatronics, vol. 15, no. 4, pp. 603–614, 2010.
- [34] X. Ye, Y. Su, and S. Guo, “A centimeter-scale autonomous robotic fish actuated by IPMC actuator,” in 2007 IEEE International Conference on Robotics and Biomimetics, 2007, pp. 262–267.
- [35] S. Xu, B. Liu, and L. Hao, “A small remote operated robotic fish actuated by IPMC,” in 2008 IEEE International Conference on Robotics and Biomimetics, 2008, pp. 1152–1156.
- [36] X. Tan, D. Kim, and N. Usher, “An autonomous robotic fish for mobile sensing,” in IEEE/RSJ International Conference on Intelligent Robots and Systems, 2006, pp. 5424–5429.
- [37] S. Yeom and I. I. Oh, “Fabrication and evaluation of biomimetic jellyfish robot using IPMC,” in 3rd International Conference on Smart Materials, Structures and Systems, vol. 58, 2008, pp. 171–176.
- [38] Z. Chen, T. Um, and H. Bart-Smith, “A novel fabrication of ionic polymer-metal composite membrane actuator capable of 3-dimensional kinematic motions,” Sensors and Actuators A: Physical, vol. 168, no. 1, pp. 131–139, 2011.
- [39] S. Guo, L. Shi, and K. Asaka, “IPMC actuator-based an underwater micro-robot with 8 legs,” in 2008 IEEE International Conference on Mechatronics and Automation, 2008, pp. 551–556.
- [40] M. Yamakita, N. Kamamichi, and T. Kozuki, “Control of biped walking robot with IPMC linear actuator,” in 2005 proceedings of International Conference on Advanced Intelligent Mechatronics, vol. 1, 2005, pp. 48–53.
- [41] J. D. W. Madden, N. Vandesteeg, P. A. Anquetil, P. Madden, and A. Takshi, “Artificial muscle technology: physical principles and naval prospects,” Oceanic Engineering, IEEE Journal of, vol. 29, no. 3, pp. 706–728, 2004.
- [42] M. Shahinpoor and K. J. Kim, “Ionic polymer-metal composites: I. fundamentals,” Smart Materials and Structures, vol. 10, pp. 819–833, 2001.
- [43] S. Nemat-Nasser and Y. L. Jiang, “Electromechanical response of ionic polymer-metal composites,” J. Appl. Phys., vol. 87, no. 7, pp. 3321 – 3331, 2000.
- [44] S. Tadokoro, S. Yamagami, and T. Takamori, “An actuator model of ICPF for robotic applications on the basis of physicochemical hypotheses,” in IEEE International conference on Robotics and Automation, vol. 2, 2000, pp. 1340 – 1346.

- [45] Z. Chen and X. Tan, “A control-oriented and physics-based model for ionic polymer-metal composite actuators,” IEEE/ASME Trans. Mechatronics, vol. 13, no. 5, pp. 519 – 529, 2008.
- [46] D. J. Leo, K. Farinholt, and T. Wallmersperger, “Computational models of ionic transport and electromechanical transduction in ionomeric polymer transducers,” in SPIE Smart Structures and Materials: Electroactive Polymer Actuators and Devices (EAPAD), vol. 5759, 2005, pp. 170 – 181.
- [47] B. C. Lavu, M. P. Schoen, and A. Mahajan, “Adaptive intelligent control of ionic polymer-metal composites,” Smart Mater. Struct., vol. 14, no. 4, pp. 466 – 474, 2005.
- [48] R. C. Richardson, M. C. Levesley, M. D. Brown, J. A. Hawkes, K. Watterson, and P. G. Walker, “Control of ionic polymer metal composites,” IEEE/ASME Trans. Mechatronics, vol. 8, no. 2, pp. 245 – 253, 2003.
- [49] N. D. Bhat and W.-J. Kim, “Precision force and position control of ionic polymer-metal composite,” Journal of Systems and Control Engineering, vol. 218, no. 6, pp. 421 – 432, 2004.
- [50] S. Kang, J. Shin, S. J. Kim, H. J. Kim, and Y. H. Kim, “Robust control of ionic polymer-metal composites,” Smart Mater. Struct., vol. 16, no. 6, pp. 2457 – 2463, 2007.
- [51] K. Krishen, “Space applications for ionic polymer-metal composite sensors, actuators, and artificial muscles,” Acta Astronautica, vol. 64, no. 11 – 12, pp. 1160 – 1166, 2009.
- [52] R. Tiwari, K. J. Kim, and S. Kim, “Ionic polymer-metal composite as energy harvesters,” Smart Structures and Systems, vol. 4, no. 5, pp. 549 – 563, 2008.
- [53] J. Brufau-Penella, M. Puig-Vidal, P. Giannone, S. Graziani, and S. Strazzeri, “Characterization of the harvesting capabilities of an ionic polymer metal composite device,” Smart Mater. Struct., vol. 17, no. 1, p. 015009 (15 pages), 2008.
- [54] M. Aureli, C. Prince, M. Porfiri, and S. D. Peterson, “Energy harvesting from base excitation of ionic polymer metal composites in fluid environments,” Smart Mater. Struct., vol. 19, p. 015003 (15 pages), 2010.
- [55] W. J. Yoon, P. G. Reinhall, and E. J. Seibel, “Analysis of electro-active polymer bending: A component in a low cost ultrathin scanning endoscope,” Sensors and Actuators A: Physical, vol. 133, no. 2, pp. 506 – 517, 2007.
- [56] B.-K. Fang, M.-S. Ju, and C.-C. K. Lin, “A new approach to develop ionic polymer-metal composites (IPMC) actuator: fabrication and control for active catheter systems,” Sensors and Actuators A: Physical, vol. 137, no. 2, pp. 321 – 329, 2007.

- [57] E. Biddiss and T. Chau, "Electroactive polymeric sensors in hand prostheses: Bending response of an ionic polymer metal composite," Medical Engineering and Physics, vol. 28, no. 6, pp. 568 – 578, 2006.
- [58] N. Kamamichi, M. Yamakita, K. Asaka, and Z. Luo, "A snake-like swimming robot using IPMC actuator/sensor," in IEEE International Conference on Robotics and Automation, 2006, pp. 1812–1817.
- [59] J. Ayers and J. Witting, "Biomimetic approaches to the control of underwater walking machines," Philosophical Transactions of the Royal Society A: Mathematical, Physical and Engineering Sciences, vol. 365, no. 1850, pp. 273–295, 2007.
- [60] M. Bozkurttas, J. Tangorra, G. Lauder, and R. Mittal, "Understanding the hydrodynamics of swimming: From fish fins to flexible propulsors for autonomous underwater vehicles," in International Conference on Smart Materials, Structures and Systems, vol. 58, 2008, pp. 193–202.
- [61] J. H. J. Buchholz, R. P. Clark, and A. J. Smits, "Thrust performance of unsteady propulsors using a novel measurement system, and corresponding wake patterns," Exp Fluids, vol. 45, pp. 461–472, 2008.
- [62] N. Kato, "Locomotion by mechanical pectoral fins," Journal of Marine Science and Technology, vol. 3, no. 3, pp. 113–121, 1998.
- [63] J. L. Tangorra, . S. N. Davidson, I. W. Hunter, P. G. Madden, . G. V. Lauder, H. Dong, M. Bozkurttas, and R. Mittal, "The development of a biologically inspired propulsor for unmanned underwater vehicles," Oceanic Engineering, IEEE Journal of, vol. 32, no. 3, pp. 533–550, 2007.
- [64] Y. Cai, S. Bi, and L. Zheng, "Design and experiments of a robotic fish imitating cow-nosed ray," Journal of Bionic Engineering, vol. 7, no. 2, pp. 120–126, 2010.
- [65] G. Tortora, S. Caccavaro, and P. Valdastri, "Design of an autonomous swimming miniature robot based on a novel concept of magnetic actuation," in IEEE International Conference on Robotics and Automation, pp. 1592–1597.
- [66] W. Yim and et al., "An artificial muscle actuator for biomimetic underwater propulsors," Bioinspiration and Biomimetics, vol. 2, no. 2, p. S31, 2007.
- [67] P. R. Bandyopadhyay, D. N. Beal, and A. Menozzi, "Biorobotic insights into how animals swim," Journal of Experimental Biology, vol. 211, pp. 206 – 214, 2008.
- [68] K. Kruusamae, P. Brunetto, S. Graziani, A. Punning, G. Di Pasquale, and A. Aabloo, "Self-sensing ionic polymer-metal composite actuating device with patterned surface electrodes," Polymer International, vol. 59, no. 3, pp. 300 – 304, 2009.

- [69] K. J. Kim and M. shahinpoor, "Ionic polymer-metal composites: II. manufacturing techniques," Smart Materials and Structures, vol. 12, pp. 65–79, 2003.
- [70] K. J. Kim, Electroactive Polymers for Robotic Applications. Springer, 2007.
- [71] K. J. Kim and M. Shahinpoor, "A novel method of manufacturing three-dimensional ionic polymer-metal composites (IPMCs) biomimetic sensors, actuators and artificial muscles," Polymer, vol. 43, no. 3, pp. 797–802, 2002.
- [72] S. Lee, H. Park, S. D. Pandita, and Y. Yoo, "Performance improvement of IPMC (ionic polymer metal composites) for a flapping actuator," Journal of Control, Automation and Systems, vol. 4, no. 6, pp. 748–755, 2006.
- [73] M. Aureli, V. Kopman, and M. Porfiri, "Control-oriented modeling of ionic polymer metal composites for biomimetic underwater propulsion," in American Control Conference (ACC), 2010, pp. 6016–6021.
- [74] N. N. Pak and S. Scapellato, "Biomimetic design of a polychaete robot using IPMC actuator," in International Conference on Biomedical Robotics and Biomechatronics, 2006, pp. 666–671.
- [75] P. Horowitz and W. Hill, The art of electronics, 2nd ed. New York: Cambridge University Press, 1989.
- [76] K. J. Kim and M. Shahinpoor, "A novel method of manufacturing three-dimensional ionic polymer-metal composites (ipmcs) biomimetic sensors, actuators and artificial muscles," Polymer, vol. 43, no. 3, pp. 797 – 802, 2002.
- [77] B. Kim, B. M. Kim, J. Ryu, I.-H. Oh, S.-K. Lee, S.-E. Cha, and J. Pak, "Analysis of mechanical characteristics of the ionic polymer metal composite (IPMC) actuator using cast ion-exchange film," in SPIE Smart Structures and Materials: Electroactive Polymer Actuators and Devices (EAPAD), vol. 5051, San Diego, CA, USA, 2003, pp. 486 – 495.
- [78] J. J. Pak, J. Kim, S. W. Oh, J. H. Son, S. H. Cho, S.-K. Lee, J.-Y. Park, and B. Kim, "Fabrication of ionic-polymer-metal-composite (IPMC) micropump using a commercial nafion," in SPIE Smart Structures and Materials: Electroactive Polymer Actuators and Devices (EAPAD), vol. 5385, 2004, pp. 272 – 280.
- [79] Y. Shan and K. K. Leang, "Frequency-weighted feedforward control for dynamic compensation in ionic polymer-metal composite actuators," Smart Materials and Structures, vol. 18, no. 12, p. 125016 (11 pages), 2009.
- [80] S. J. Lee, M. J. Han, S. J. Kim, J. Y. Jho, H. Y. Lee, and Y. H. Kim, "A new fabrication method for ipmc actuators and application to artificial fingers," Smart Mater. Struct., vol. 15, pp. 1217 – 1224, 2006.

- [81] S. McGovern, M. Abbot, R. Emery, and G. Alici, "Evaluation of thrust force generated for a robotic fish propelled with polypyrrole actuators," Polymer International, vol. 59, pp. 357–364, 2010.
- [82] I. Akhtar, R. Mittal, G. V. Lauder, and E. Drucker, "Hydrodynamics of a biologically inspired tandem flapping foil configuration," Theoretical and Computational Fluid Dynamics, vol. 21, no. 3, pp. 155–170, 2007.
- [83] K. Harper, M. Berkemeier, and S. Grace, "Modeling the dynamics of spring-driven oscillating-foil propulsion," IEEE Journal of Oceanic Engineering, vol. 23, no. 3, pp. 285–296, 1998.
- [84] D. Xia, J. Liu, W. Chen, and L. Han, "Hydrodynamic analysis of fishlike robot swimming in the straight forward way," in IEEE International Conference on Mechatronics and Automation, 2009, pp. 3342–3347.
- [85] D. Kim and K. Kim, "Experimental investigation on electrochemical properties of ionic polymer-metal composite," Journal of Intelligent Material Systems and Structures, vol. 17, no. 5, pp. 449–454, 2006.
- [86] T. I. Fossen, Guidance and Control of Ocean Vehicles, 1st ed. John Wiley and Sons Incorporated, 1994.
- [87] V. Stepanyan, N. Hovakimyan, and C. A. Woolsey, "Adaptive output feedback control of a spheroidal underactuated underwater vehicle," in MTS/IEEE Proceedings on Oceans, vol. 1, pp. 278–284.
- [88] P. Kodati, J. Hinkle, A. Winn, and D. Xinyan, "Microautonomous robotic ostraciiform (marco): Hydrodynamics, design, and fabrication," IEEE Transactions on Robotics, vol. 24, no. 1, pp. 105–117, 2008.
- [89] M. Triantafyllou and G. Triantafyllou, "An efficient swimming machine," Sci. Am., vol. 272, pp. 64–71, 1995.
- [90] P. R. Bandyopadhyay, "Maneuvering hydrodynamics of fish and small underwater vehicles," Integ. and Comp. Biol., vol. 42, pp. 102 – 117, 2002.

Appendix A

Alternative IPMC Assembly for Complex Bending and Twisting

The characterization of a monolithic IPMC for bending and twisting motion was discussed in Chapter 4.1. Bending and twisting control surface be accomplished with conventional IPMCs and a flexible medium. The bending deflection and twist angle was investigated for an assembly containing three separate IPMCs housed in a silicone casting rubber medium as well as the twist angle of a sectored IPMC.

The use of a flexible sheathe to house IPMCs and provide a uniform surface for hydrodynamic control was of interest to the office of naval research. The feasibility of this composite design was investigated by the electroactive systems lab under direct instruction of Dr. Kim and the active materials and processing laboratory. To reduce stiffness of the initial prototype silicone casting rubber was proposed as the material of choice for the housing. A flexible sleeve or "boot" was provided by the Active Materials and Processing Laboratory (AMPL) for investigation of this concept. IPMCs could be inserted into was investigated. By inserting multiple IPMCs into the boot, complex deformation of the boot can be achieved. Three IPMCs were cut to 57 mm long by 11 mm wide and made to fit snugly inside the slots built into the

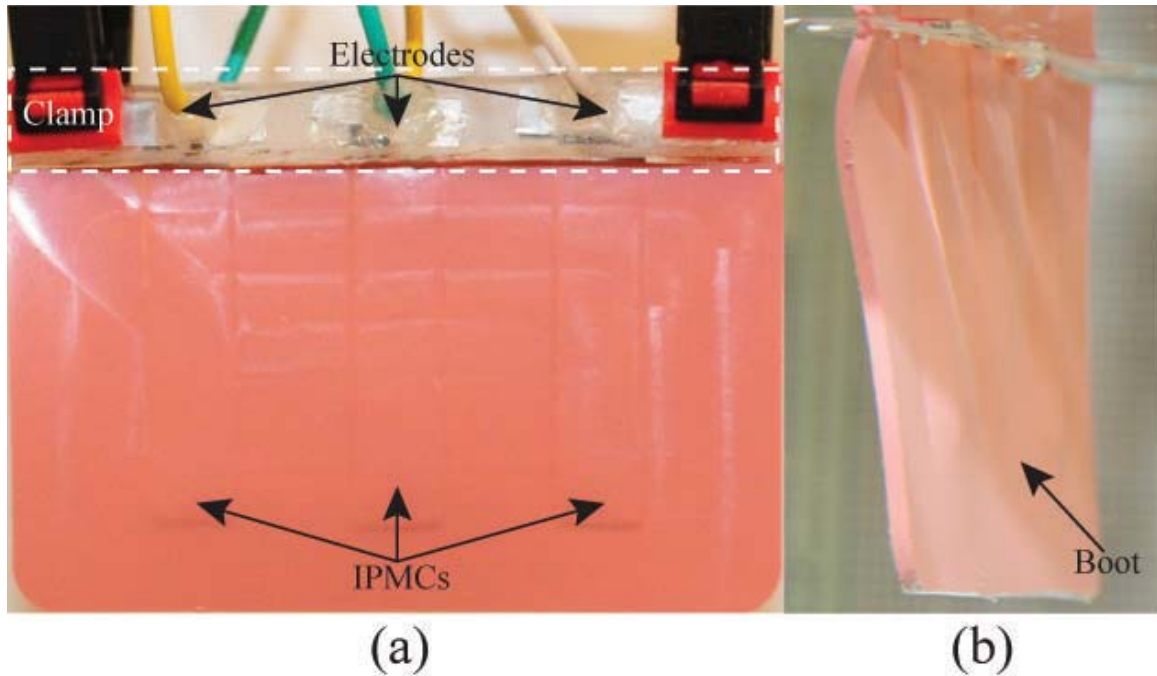


Figure A.1: Soft medium with embedded IPMCs: (a) front view and (b) isometric view.

boot, with a spacing of 25 mm. Due to the nature of testing, the clamp itself spends a significant amount of time in the water. For corrosion resistance, the electrodes were constructed out of stainless steel 304 and acrylic is chosen for the clamp itself. When clamped, the boot-IPMC system has an effective length of 46 mm. The full assembly used can be seen in Fig. A.1.

The clamp with the boot- IPMC assembly is then suspended from an aluminum rod and submerged in the tank. The IPMCs were then actuated with a 4-V (volt amplitude) sine or square wave input signal; the driving frequency was 50 mHz. A bending test was the first to be conducted; to achieve maximum deflection, square wave input signal with the same phase are applied to all three IPMCs in the boot. In Fig. A.2, three consecutive images taken at intervals of 3.5 seconds illustrate the bending action relative to the input signal (vertical dash-line corresponds to the time instant each image is acquired). A maximum tip deflection of 44 mm relative to the

vertical is achieved.

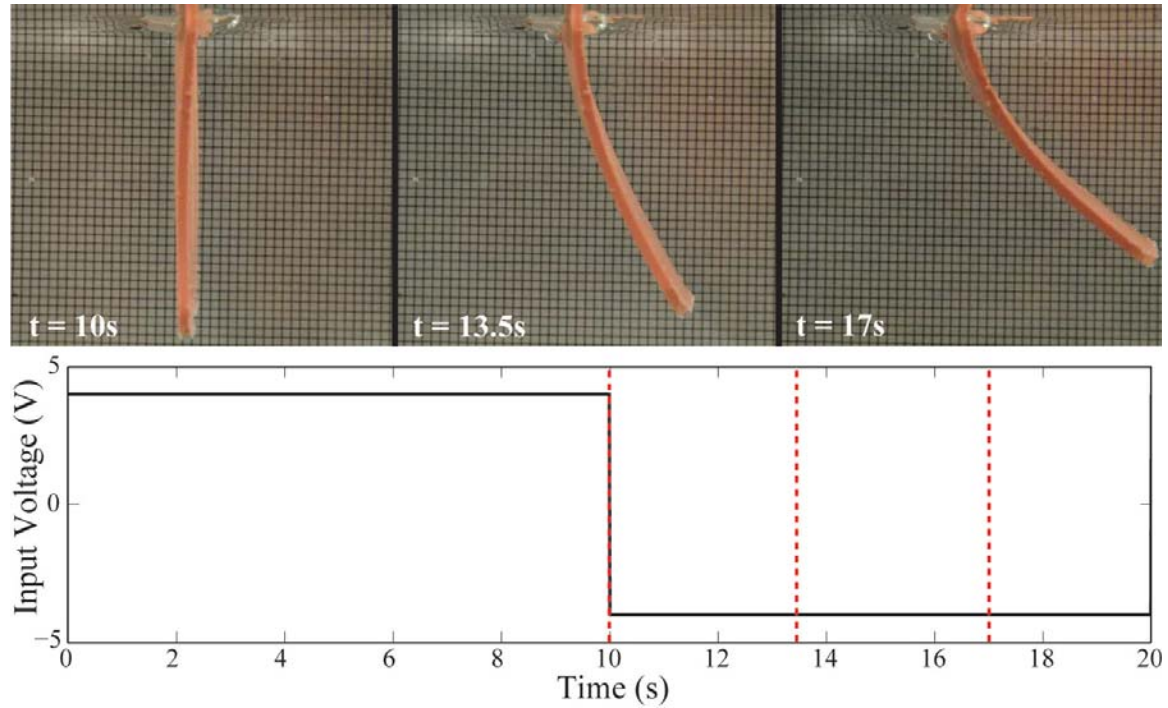


Figure A.2: Time lapse images of boot-IPMC assembly bending due to a 4 V 50 mHz square wave input signal. The times corresponding to the images are indicated by the red dotted lines overlaid on the input signal plot directly above.

Next a twisting motion is generated. To produce this movement the center IPMC was disabled while phase shifting the adjacent IPMCs by 180 degrees relative to each other. The maximum twist angle is found to be approximately 12 degrees and can be seen from two viewpoints in Fig. A.3. Note a complex shape is generated so that the angle varies both along the length and height of the boot. This can be attributed to the flexible boot material and non-linear bending behavior along the length of the actuators. While the complex shape may complicate predicting lift and drag forces by comparison to conventional control surfaces it confirms application potential.

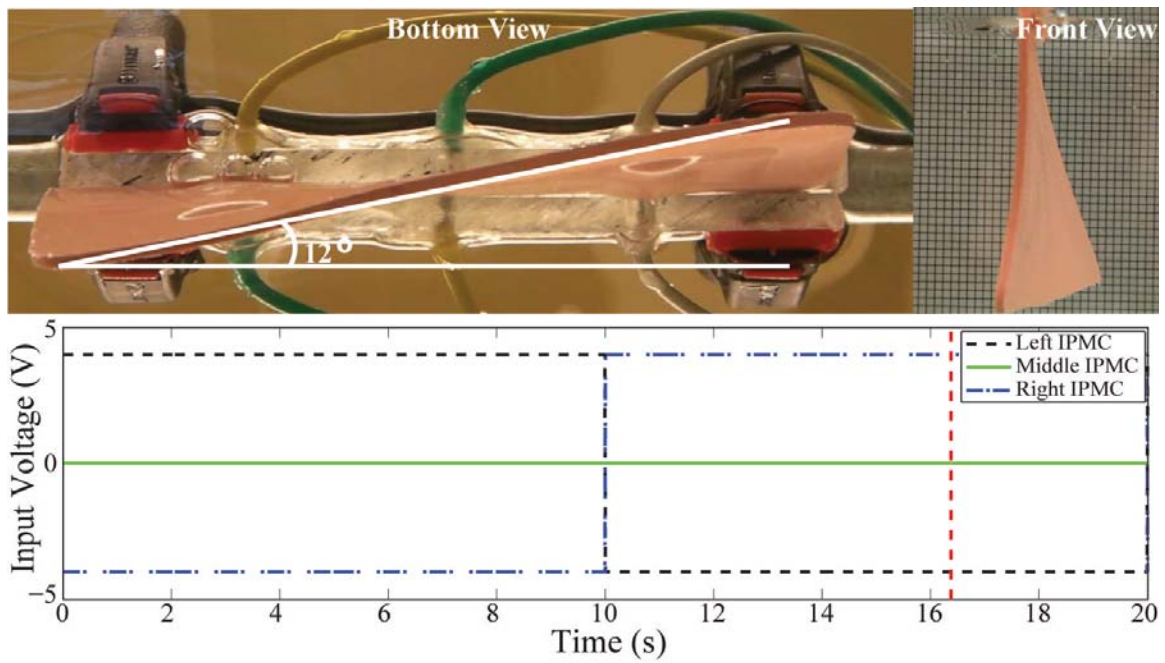


Figure A.3: Two views depicting the maximum twist angle achieved. The input signal is plotted directly above and the time of maximum deflection is noted by the red dotted line.